Development of Plasmonic Sensors for Leukemia Diagnosis

by

Chiara Valsecchi
B. Sc., University of Milan, 2009

A Thesis Submitted in Partial Fulfillment
of the Requirements for the Degree of

MASTER OF SCIENCE

in the Department of Chemistry

Supervisory Committee

Development of Plasmonic Sensors for Leukemia Diagnosis

by

Chiara Valsecchi
B. Sc., University of Milan, 2009

Supervisory Committee

Dr. Alexandre G. Brolo, (Department of Chemistry)
Supervisor

Dr. Dennis Hore, (Department of Chemistry)
Departmental Member

Dr. Reuven Gordon, (Department of Electrical Engineering)
Outside Member

Abstract

Supervisory Committee
Dr. Alexandre G. Brolo, (Department of Chemistry)
Supervisor
Dr. Dennis Hore, (Department of Chemistry)
Departmental Member
Dr. Reuven Gordon, (Department of Electrical Engineering)
Outside Member

Plasmonic materials constitute one of the most explored platforms in the past decade for biological sensing, as they offer a wide range of advantages in respect to the currently available tests employed in either screening or medical diagnosis.The detection of leukaemia cancer markers was chosen as the medical applications in the evaluation of the sensing capabilities of these platforms.

Particularly, nanohole arrays on gold films have already been demonstrated to be efficientsensing elements for the study of protein – protein interactions. In this work,nanohole arrays platforms were optimized by studying the combinations of shape, diameter, aspect ratio, polarization and periodicity that lead to the highest sensitivity. In addition, different nanohole arrays substrates fabricated by UV-nanolithography and interference lithography were characterized and compared to the structures made by conventional focus ion beam (FIB) milling. Analytes derived from blood sample of leukemia cancer patients were detected on these structures with great sensitivity and specificity, demonstrating a large potential for medical applications.

Furthermore, the development and characterization of a cost-effective system capable of detecting leukaemia cancer markers with comparable limit of detection and sensitivity as commercial platforms was started. With future development, this platform could provide advantages in terms of miniaturization, analysis time and the integration as an easy-to-use lab-on-chip device for diagnostics.

Table of Contents

Supervisory Committee ii
Abstract iii
Table of Contents iv
List of Tables vi
List of Equations vii
List of Figures viii
Abbreviations xiii
Acknowledgments xiv
Chapter 1: Overview 1
1.1 Thesis Organization 3
Chapter 2: Background 5
2.1 Surface Plasmon Resonance 5
2.2 Surface Plasmon for Biosensing: Detection Schemes 11
2.3 Performance of Plasmonic Biosensors 15
2.4 SPR Application for Leukemia Detection 20
2.4.1 Leukemia 21
Chapter 3: Background on the Nano- and Micro-fabrication Methods 24
3.1 Introduction 24
3.2 Fabrication of Nanohole Platforms 24
3.2.1 Focused Ion Beam (FIB) Milling 25
3.2.2 Interference Lithography 27
3.2.3 UV nanoimprinting 30
3.2.4 Scanning Electron Microscopy (SEM) 32
3.2.5 Energy-Dispersive X-Ray Spectroscopy 33
3.3 Microfluidic and Photolithography 35
Chapter 4: Experimental Setup 39
4.1 Sample Fabrication 39
4.1.1 Fabrication of Nanohole Arrays by FIB 39
4.1.2 Large Area Nanoholes Fabricated by IL 40
4.1.3 Nanoholes on Plastic Fabricated by UV nanoimprinting 42
4.2 Photolithography and Microfluidic chip 43
4.3 Optical and Chemical Sensing Setups 44
4.3.1 Transmission Detection 44
4.3.2 Intensity Detection with a Charge-Coupled Device (CCD) 47
4.4 FDTD Simulation 49
4.5 Surface Chemistry 53
4.5.1 Biotin and Streptavidin 53
4.5.2 Surface Modification for Leukemia Detection 55
Chapter 5: Results on the Geometrical Influence on the Performance of Nanohole Arrays Fabricate by FIB 60
5.1 Geometrical Parameters 60
5.2 Circular Holes 63

5.3 Rectangular Arrays 67
5.3.1 TM Polarization Studies 69
5.3.2 TE Polarization Studies 72
5.3.3 In-sample and Sample-to-Sample Variation 75
5.4 Final Remarks 77
Chapter 6: Plasmonic Sensing using Large Area Nanohole Arrays Fabricated by UV Nanolithography 79
6.1 Bulk Sensitivity 79
6.2 Biotin-SA 83
6.3 Leukemia Cancer Marker Detection 85
Chapter 7: Plasmonic Sensing using Large Area Nanohole Arrays Fabricated by IL 90
7.1 Bulk Sensitivities 90
7.2 Surface Sensitivity 91
7.3 Detection of Leukemia Cancer Markers 94
Chapter 8: Development of a Reliable Biosensing Scheme for Multiplexing 100
8.1 Hardware Characterization 100
8.1.1 Environmental Interference 102
8.1.2 Opto-mechanic 103
8.1.3 Light Source 104
8.1.4 CCD Detector 105
8.2 Preliminary Results 109
Chapter 9: Conclusion 114
Bibliography 116

List of Tables

Table 2.1 Summary of four performance parameters used in the evaluation of plasmonic biosensors (Γ: Surface coverage, g/mm²; C: concentration, mg/mL; t: film thickness, nm) 19

Table 4.1. Geometrical characteristics of the nanoholes gratings studied.....43

Table 5.1 Example of the in-sample and sample-to-sample variation found in the analysis performed. The values refer to experiment conducts with rectangular holes, under TE polarization 76

Table 5.2 Summary of the best performance parameters obtained for the different nanoholes arrays.....78

Table 6.1 Summary of the performance obtained from Sample 1 and Sample 2, both without the chromium layer. The geometrical parameters of the structures are outlined in Table 6.2 82

Table 6.2 Summary of the performance of Sample 3, taken for all the structures in two different points. In the fourth column, it is shown an estimate of respective resolutions. The geometrical parameters of the structures are outlined in the last two columns. 82

Table 6.3 Summary of the performance in surface sensing of Sample 3, obtained for all the structures at different points.....84

Table 7.1 Summary of the performance achieved with large area nanoholes array made by IL for both bulk and surface sensing.....97

Table 9.1 Summary of the performance values obtained for all the periodic structures studied. Transmission and Intensity define the different type of data monitoring and acquisition. 114

List of Equations

$$k_{SP} = k_0 \sqrt{\frac{\varepsilon_m \varepsilon_d}{\varepsilon_d + \varepsilon_m}}$$ Eq. 2.1 7

$$K_{SP} = K_x + G$$ Eq. 2.2 10

$$G = \frac{2\pi}{\Lambda}$$ Eq. 2.3 10

$$\lambda_0 = \frac{\Lambda}{\sqrt{(i^2 + j^2)}} \cdot \sqrt{\frac{\varepsilon_d \varepsilon_m}{\varepsilon_d + \varepsilon_m}}$$ Eq. 2.4 10

$$Res = \frac{\sigma_{so}}{S_b}$$ Eq. 2.5 19

$$\Lambda = \frac{\lambda}{2\,\mathrm{Sin}\theta}$$ Eq. 3.1 30

$$\theta = \frac{\theta_{Max} \cdot C}{K_D + C}$$ Eq. 7.1 93

List of Figures

Figure 1.1Prototype developed to demonstrate the effective miniaturization and low cost opportunities possible with SPR biosensor. From the right, an LED source illuminates the sample encased into a microfluidic system and a photodiode records the intensity variation with refractive index changes. [Reproduced with permission from [20]] 2

Figure 2.1a) Schematic representation of the propagation length of a PSP b) schematic representation of the field confinement typical of LSP. [Reproduced with permission from [32]] 6

Figure 2.2 Dispersion curve of light in vacuum and surface plasmon. Inset: representation of surface plasmon oscillations [Reprint with permission from [39] and [38]] 8

Figure 2.3 a) Kretschmann and Raether configuration, involving the use of a prism for the excitation of SPs. b) Change to the dispersion curve of light due to the introduction of the prism [Reprinted and modified with permission from [41] and [4]] 9

Figure 2.4 a) Grating-coupling configuration: the corrugations mediate the excitation of SPs. b) Change in the dispersion curve of light due to the periodic grooves on the metal surface [Reproduced and modified from[4]] 10

Figure 2.5 a) Prism-based configuration scheme and b) the plot of the resulting angular shift detection. c) Nanohole arrays configuration and d) the plot of the wavelength shift detection. [Reproduced with permission from [32]] 13

Figure 2.6 Typical kinetics curve obtained from the prism-coupled Biacore® SPR system. [Reproduced with permission from [49]] 14

Figure 2.7 Schematic of the decay field profile (field intensity (E^2) variation in the z-axis); a) in the absence of adsorbates, where n_{bulk} correspond to the refractive index of the bulk liquid; b) in the presence of adsorbates with a refractive index $n_{surface}$ 16

Figure 2.8a) SPR spectra obtained from a nanohole array immersed in different liquids; b) wavelength shift plotted against the refractive indexes. the bulk sensitivity (Sb) is the slope of this line. 17

Figure 2.9Antibody structure: in nature there are 5 types of heavy chains (blue), but only two type of light chains (red). [Reproduced with permission from [66]] 21

Figure 3.1 Scanning electron micrograph of sub-micron scale crests of the University of Victoria in a Copper TEM grid, fabricated with a Hitachi FB-2100 FIB [Reproduced with permission from [69]] 25

Figure 3.2 Scanning electron micrograph of a nanohole array profile fabricated by FIB. The gold layer is completely milled through, reaching down to the glass substrate. 26

Figure 3.3 a) Schematic of a conventional light interference and b) the scheme for a Llyod-mirror interferometer implemented in the setup for the nanohole fabrication and c) (following page) the actual scheme used for this project 27

Figure 3.4 Schematic on how generate 2D patterns with IL; after the first exposure, the sample is rotated by a desired angle and expose again to the interfering light.....28

Figure 3.5 UV nanoimprint process scheme: the low cost and the mass fabrication is due to its simplicity. [Reproduced with permission from[75]].....31

Figure 3.6 Two different representation of the structure employed; a) cartoon and b) SEM micrograph of the large area nanohole.....32

Figure 3.7 Electronic composition for a SEM image. [Reproduced with permission from 62].....33

Figure 3.8 Schematic of the EDX process [Reproduced with permission from [80]].....34

Figure 3.9 EDX images obtained for gold surfaces with nanoholes on glass substrates.....35

Figure 3.10 Picture of the photolithography mask used and enlargement of a detail to show the parameters considered.....36

Figure 3.11 Schematic for a photolithography process 37

Figure 3.12 Schematic of a typical microfluidic chip fabrication with PDMS. [Reproduced with permission from[83]].....38

Figure 4.1 SEM images of two samples of nanoholes arrays fabricated by FIB.....40

Figure 4.2 SEM image of a) photoresist template and b) large area (2cm by 2cm) nanoholes array after gold deposition and photoresist removal.....41

Figure 4.3 a) SEM micrograph of nanoholes made by UV nanoimprinting; the size of the feature is 200 nm and the periodicity is 330 nm. b) Photo of the whole substrate showing the six different gratings and their labels.....42

Figure 4.4 a) Image of the silicon master plate produced by photolithography. b) Image of the PDMS microfluidic chip assembled onto the gold nanoholes substrates; one inlet and one outlet teflon tubings for microfluidic are also shown 44

Figure 4.5 Schematic of the transmission setup with enlargements of the nanohole sample and microfluidic channels; the cartoon at the bottom represent an example of binding event at the metal surface inside a specific channel 45

Figure 4.6 Illustrative representation of the optics involved in the setup for intensity interrogation. From the right: laser source, 633nm; spatial filter; iris; collimating lens; iris; sample; focusing lens; CCD detector.....47

Figure 4.7 a) Example of image (part) collected by the CCD detector; b) representation of the grid and areas used by the program to evaluate the transmitted intensities from the arrays 48

Figure 4.8 a) Schematic representation of the Yee's cell, with the 3D indication of the vectors for the electric and magnetic fields. b) cartoon representing the iterative process occurring in a simulation. The behaviour of periodic boundaries is also shown [a) Reproduced with permission from[88]].....50

Figure 4.9 a) 3D image of the structure build for the simulations. All the elements required for the calculations are visible and described in the text. b) xy plane enlarged image of a nanohole at the center of the computational space (orange frame). 52

Figure 4.10a) 3D ribbon representation of the streptavidin structure with a sphere representation of the much smaller biotin in the binding site. b) Schematic diagram of the modified surface after formation of a PEG monolayer cross-linked with biotin [a) reproduced with permission from[94]] 54

Figure 4.113D cartoons explaining the steps involved in the surface functionalization with antibodies. a) formation of a SAM layer that can be covalently modified with the antibodies as in b). c) represents the surface after being coated with BSA, to avoid non-specific binding, and d) is a representation of the antigens capture by the modified surface 56

Figure 4.12 Schematic representation of the EDC-NHS chemistry for covalent attachment of proteins to an existent SAM.....57

Figure 4.13 Schematic representation of a) antibody structure and b) protein A structure ...58

Figure 4.14 Cartoon representing the surface modification with protein A [Modified with permission from [96]] 59

Figure 5.1 Overview of all the different combinations of geometrical parameters for shapes employed in this study 61

Figure 5.2a) Comparison of transmitted spectra for circular arrays with the same periodicity but different hole diameters, as indicated. b) Comparison of transmitted spectra for circular arrays with the same hole diameter (200 nm)but different periodicities. 62

Figure 5.3 Bar graph representing the values of bulk sensitivity obtained experimentally for circular arrays. 64

Figure 5.4 Bar graph representing the values of bulk sensitivity obtained computationally for circular arrays. 64

Figure 5.5 Bar graph representing the values of surface sensitivity obtained experimentally for circular arrays. 65

Figure 5.6 Bar graph representing the values of surface sensitivity obtained computationally for circular arrays. The trend confirms the bulk sensing behaviour, both experimental and calculated 66

Figure 5.7a) Polarization of the light in respect of the rectangular nanohole. Comparison between the TM and TE polarization for a) rectangular nanohole arrays, 50nm by 250nm and periodicity of 450 nm; b) rectangular nanohole arrays, 200nm by 250nm and 450 nm periodicity; d) circular holes, 150nm in diameter, periodicity of 450 nm. 68

Figure 5.8 Bar graph representing the values of bulk sensitivity obtained experimentally for rectangular arrays under TM polarized light. The trend matches what found for circular arrays, as expected. 70

Figure 5.9 Bar graph representing the values of bulk sensitivity obtained computationally for rectangular arrays under TM polarized light. The trend confirms what found experimentally.....71

Figure 5.10 Bar graph representing the values of surface sensitivity obtained computationally for rectangular arrays under TM polarized light. The trend reflects what found for the bulk sensing.....72

Figure 5.11 Bar graph representing the values of surface sensitivity obtained computationally for rectangular arrays under TM polarized light.....72

Figure 5.12 Bar graph representing the values of bulk sensitivity obtained experimentally for rectangular arrays under TE polarized light.....73

Figure 5.13 Bar graph representing the values of bulk sensitivity obtained computationally for rectangular arrays under TE polarized light. The trend confirms what found experimentally.....73

Figure 5.14 Bar graph representing the values of surface sensitivity obtained experimentally for rectangular arrays under TE polarized light. The trend reflects the results obtained for bulk sensing. 74

Figure 5.15 Bar graph representing the values of surface sensitivity obtained computationally for rectangular arrays under TE polarized light. The trend deviates from the results obtained experimentally. 74

Figure 5.18 Bar plot calculated by adding the sample-to-sample variability in Table 5.1b to the results of surface sensitivity obtained for rectangular array, under TE polarization. 77

Figure 6.1 Graph summarizing the bulk sensitivities obtained from two different spots on each grating structure. Inset: schematic reminder of the sample with the six different structures.....80

Figure 6.2 SEM micrograph showing a) the uneven features due to the fabrication process and b) the damage present on the samples.....81

Figure 6.3 Graph summarizing the surface sensitivities obtained from two different spots on each grating structure.....83

Figure 6.4 a) Plot representing the spectral shift recorded after the functionalization of the surface (red curve) and the binding of the antigens (blue curve). b) Spectral shift obtained after the functionalization of the surface (red curve) and the non-specific binding from the absorption of the wrong antigen (blue curve). 86

Figure 6.5 a) Summary of the spectral shift obtained on each grating by the surface functionalization with anti-lambda antibodies (black bars) and the absorption of the lambda antigen (red bars). b) Direct comparison of the spectral shift obtained for the Lambda absorption (red bar, as in a)) and the control experiments due to Kappa antigens binding non-specifically (black bars).....87

Figure 6.6 Representation of the spectral shift obtained from the binding of the lambda antigens (green curve) after the non-specific binding of the wrong molecules (kappa antigens, blue curve), used as negative control.....88

Figure 7.1Spectral shifts due to the different refractive index used, listed in the table on the right. Note: some data are not included for better clarity. 91

Figure 7.2 a) Spectral shifts detected after the binding of streptavidin onto the biotinylated surface at different concentrations. b) Calibration curve derived from the plot in a. The surface starts to saturate after a concentration of 5 ug/mL. 92

Figure 7.3 Langmuir fit of the data obtained for the binding of SA onto a biotinylated surface. A concentration of 1.7 μM of SA occupies 50% of the biotin sites at the surface...93

Figure 7.4 Spectral shifts detected after the functionalization of the surface with anti-lambda antigens and after the specific binding of lambda antigens. 96

Figure 8.1 Transmitted intensity monitored in time. The nanoholes arrays are in air presented large oscillations of the signal. The issue will be addressed throughout the chapter.....101

Figure 8.2 Intensity fluctuation when the temperature is left equilibrating with the environment (blue curve) or stabilized by the feedback system developed (red curve).....103

Figure 8.3 Laser stability measured in time through a photodiode connected to an oscilloscope.....105

Figure 8.4 Improvements obtained in the intensity stability after forced transfer of the fan oscillations onto the active vibration isolation table by means of an heavy object 105

Figure 8.5 Transmitted intensity in function of time recorded with the iDus Andor CCD camera.....106

Figure 8.6 Smearing of the signal due to the lack of an electronic shutter. The unwanted light could add large artifact when evaluating the information 107

Figure 8.7 Transmission spectra of the nanohole arrays used and the light source wavelength, marked at 633nm with the vertical red line. The positioning of the exciting light on the steep slope of the resonant peak allows better detection of any possible shifts109

Figure 8.8 Intensity variation when the arrays are exposed to solutions of different refractive indexes. 110

Figure 8.9 Intensity behavior in respect of time, when the nanoholes arrays modified with biotin were exposed to different concentrations of SA (1.25 μg/mL, 2.5 μg/mL and 5 μg/mL). 111

Figure 8.10 Intensity variation in respect of time of the transmitted light after the exposure to different blood samples. The surface of the nanoholes was modified with anti-lambda antibodies. The two vertical lines mark, respectively, the introduction of the different solutions and the PBS for the washing step in the microfluidic system. 112

Figure 8.11 Specific detection of the leukemia cancer marker in respect of the growth medium as control, for two other experiments. The error bars were calculated over the 7 nanohole arrays exposed to the same solution.....113

Abbreviations

SPR	surface plasmon resonance
EOT	extraordinary optical transmission
FIB	focused ion beam
IL	interference lithography
CLL	chronic lymphoid leukemia
PSP	propagating surface plasmons
LSP	localized surface plasmons
RIU	refractive index unit
LOD	limit of detection
Ig	immunoglobulin
SEM	scanning electrode microscopy
EDX	X-ray diffraction
PDMS	polydimethylsiloxane
CCD	charge-coupled device
SA	streptavidin
PBS	phosphate saline buffer
PEG	poly-ethylene glycol
BSA	bovine serum albumin
FDTD	finite-difference time-domain
RI	refractive index
TE	transverse electric
TM	transverse magnetic

Acknowledgments

Research is a learning process to achieve both personally and with the help of others. I would never have learned so much without the help of my supervisor, Dr. Alex Brolo, and all the opportunities he gave me to expand my knowledge and grow as a person.

The achievements reached in this process were also obtained thanks to the help and expertise of brilliant people in the chemistry department, as Mario, Andrew, and Chris.

These years have been tough, but also have been enjoyable, funny, interesting, full of learning and discoveries; none of these would have been possible without the awesome friends I made here in Victoria, inside and outside the lab: I will carry those memories wherever life will bring me, and you will be always in my heart.

In particular, I will never be grateful enough that I met you, Jacson; thank you for being beside me all this time, even when I was stressed and grumpy: you transformed me into the woman I am and I can’t wait to explore our future together.

At last, I would like to thank my family: sometimes less visible, but always present. They have always been supporting through this time, bearing the long distance only for the best of my future.

Chapter 1: Overview[1]

Plasmonic materials constitute one of the most explored platforms in the last decade[1-3] for biological sensing, as they offer a large range of advantages, including: facile surface chemistry for the immobilization of molecular recognition elements[4]; possibility of small sensing area[5, 6]; potential for massive multiplexing (detection of several different chemical species at the same time); easy integration with microfluidics[7, 8], leading to small device footprint, and excellent sensitivity.[9-11]

The surface-plasmons resonance (SPR) sensitivity to the dielectric environment in the vicinity of the metal surface forms the basis of the sensors[2, 3].

Periodic structures, and in particular, nanohole arrays on gold films, have already been demonstrated to be very promising sensing elements for the study of protein – protein interactions[12, 13]. The transmission of light through the nanoapertures occurs even for conditions far from the dimension limits defined by Bethe's theory[14]. This phenomenon, named "extraordinary optical transmission" (EOT),[15] allows the direct detection of adsorption and biological interactions onto the metal surface[16].

The change in refractive index due to protein binding can either be monitored as spectral variations or intensity variations of the resonant transmitted light[2, 3]. Intensity interrogation setups have already been explored in the literature, demonstrating performances comparable with the commercial benchmark[17-19].

[1] Part of this chapter was taken, with permission, from a recent publication of the author (Periodic Metallic Nanostructures as Plasmonic Chemical Sensors. *Langmuir* **2013,***accepted*)[30]

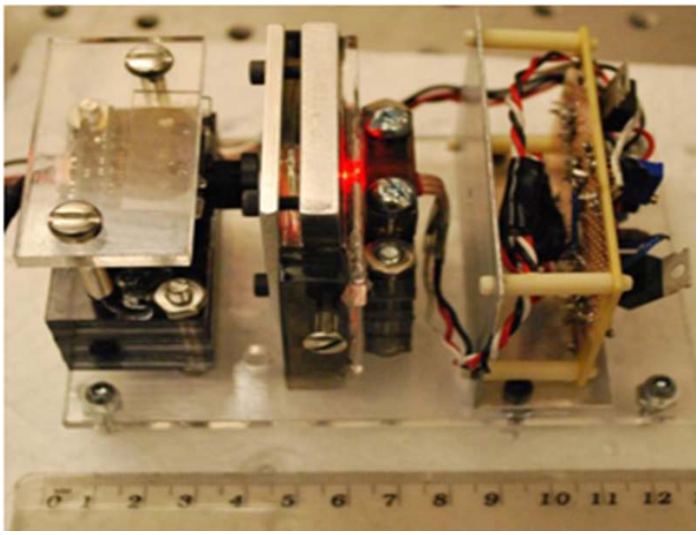

Figure 1.1Prototype developed to demonstrate the effective miniaturization and low cost opportunities possible with SPR biosensor. From the right, an LED source illuminates the sample encased into a microfluidic system and a photodiode records the intensity variation with refractive index changes. [Reproduced with permission from [20]]

Figure 1.1 shows a prototype that was kept as a model and inspiration for the research.[20] The total cost was ~$50 and is it possible to see that it spans only over 12 cm in length. A red LED light source illuminates the sample, where a CCD camera on the other side can detect the changes in intensity of the transmitted light due to the adsorption of the biomolecule of interest at the surface of the sensor.

The final goal was to build a platform capable of detecting leukaemia cancer markers with comparable (or better) limit of detection and sensitivity than the current state of the art.[21] The platform developed could provide advantages over the commercial systems in terms of miniaturization, costs and analysis time.

In order to achieve this goal, the first objective of this project was to determine a particular combination of shape[22, 23], diameter[24], polarization[17, 25] and periodicity[26] that would lead to the highest sensing performance.

FIB is normally the most common method for the fabrication of subwavelength platforms. However, structures fabricated by FIB are expensive and normally present a small sensing area (less than 30 μm^2).[27, 28] Therefore other fabrication methods, such as interference lithography (IL) and UV Nanoimprinting, have been recently studied, optimized and developed to produce new, low-cost, and efficient plasmonic biosensors[29, 30]. In addition, both fabrication methods (IL and UV nanoimprinting) are suitable for mass production, closing the gap between expensive research-grade samples and affordable substrates that can be commercialized. For the reasons just outlined, large area nanohole arrays fabricated by IL and UV nanoimprinting were studied and characterized. The future envision would be to possible integrate this platforms as an easy-to-use lab-on-chip device for diagnostics[1].

In particular, leukemia diagnosis was the real medical application chosen to prove the biosensing capabilities of these platforms and system. Leukemia is the name attributed to the cancer of the white blood cells (leukocytes). The most common type of leukemia is chronic lymphoid leukemia (CLL) that is mostly widespread among adults, with the majority being men over 50 years old[31]. The current methodology to analyse blood samples to detect this cancer are fairly costly and require some days for the results. The development of an affordable and sensitive SPR platform could improve the detection of leukemia by making it more accessible to everyone.

1.1 Thesis Organization

This thesis is organized in nine chapters. Chapter 1 provides a brief description of the main objectives of the work. Chapters 2 will provide the background concepts on surface plasmon resonance (SPR) sensing, as well as a detailed discussion on the evaluation of plasmonic

sensor performance. Some information on Leukemia cancer markers and diagnostics will also be introduced. Chapters 3 will follow with a general description of the sample fabrication and microfluidics. Chapter 4 will provide the details on the fabrication of the plasmonic structures used, the methods employed for surface modification, and the experimental conditions used throughout the work. The experimental results on the optimization of the sensing characteristics of the arrays fabricated by FIB will be described in Chapter 5. Chapter 6 and 7 will outline the sensing results obtained for large area nanoholes arrays, fabricated by UV nanoimprinting and IL, respectively.

Chapter 8 will described the roadblocks and successes encountered with the development of the intensity detection setup, including some suggestions for future works.Final remarks and conclusions can be found in Chapter 9.

Chapter 2: Background

This chapter will outline some background theory on surface plasmons, their physical properties and the most common configurations used for SPR biosensing.

The reasons and motivations behind the wide use of SPR devices as biosensor will be introduced, together with the typical parameters used to evaluate their performance. At last, there will be a brief introduction over the specific biomedical target (Leukemia) addressed in this thesis.

Part of this chapter was taken, with permission, from a recent publication of the author.[32]

2.1 Surface Plasmon Resonance

If a metal is considered to behave under the Drude model assumptions[33], then its electrons can be seen as moving freely inside the bulk material: almost like an high density electron gas, called a plasma. In particular, these free electrons on a metal surface can be excited by visible light to produce collective electronic oscillations called, by consequence, surface plasmons (SPs)[34].

SPs can be broadly classified according to the characteristics of their electromagnetic field. As shown in Figure 2.1a, there are two types of SPs: the propagating surface plasmons (PSP), occurring on a flat metal surface. Figure 2.1(a); and the localized surface plasmons (LSPs), on nanoparticles or any confined sharp features (Figure 2.1b)[35]. For both types of SPs, the field intensity is maximum at the metal surface, but they evanescently decays towards the dielectric with a decay length δ_d; typically, δ_d-values for PSPs are of the order of half of the resonance wavelength for structures, excited in the visible range[2, 33, 35].

In contrast to LSPs, PSPs travel parallel to the surface with a propagation length $\delta_{SP.}$ The magnitude of the δ_{SP} depends on the losses channels that affect the propagation at particular excitation energies: generally δ_{SP} is between 5 and 500 micrometers for experiments in the visible and near IR[35, 36].

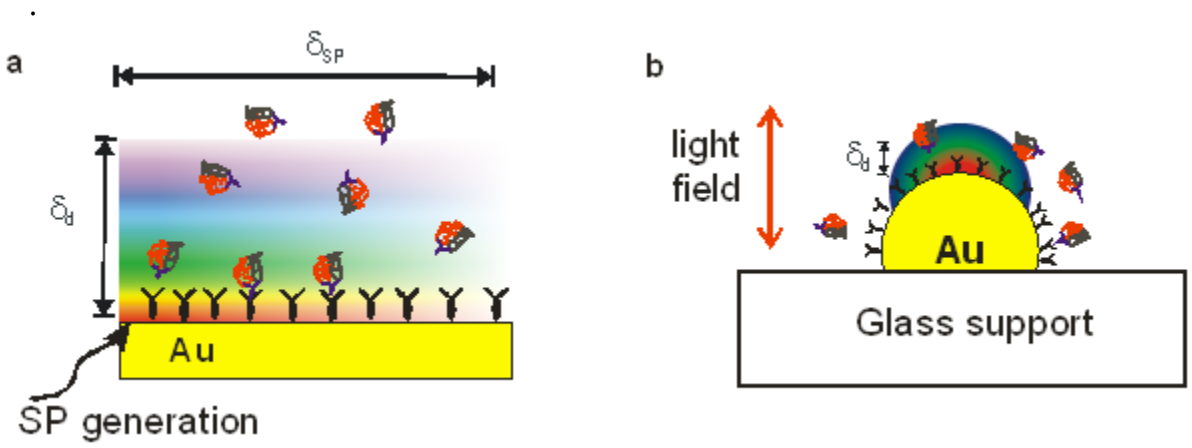

Figure 2.1a) Schematic representation of the propagation length of a PSP b) schematic representation of the field confinement typical of LSP. [Reproduced with permission from [32]]

There are three fundamental conditions for the excitation of the surface plasmons, which can be derived from Maxwell equations.

The first consideration is that SPs can only subsist on a metal surface having a negative dielectric constant: this imply that if visible light or near-IR radiations are employed to excite the plasmons, only few metals such as gold, silver and copper can be useful substrates[33]. Another important aspect regards the polarization of the incident light. As mentioned, SPs are confined to a flat surface; therefore, the oscillation of the electrons can happen only in the direction perpendicular to the interface (see inset Figure 2.2). As a consequence, only radiation with a component parallel to the plane of incidence (p-

polarized) can displace the surface charge density and generate SPs[33]. An important condition that needs to be met to excite SPs is the momentum conservation. A polished gold surface is shining because light reflects from it. In fact, SPs cannot be created on a smooth metal surface by direct optical excitation[2, 3, 37];because the SP momentum is larger than the one of a free-photon, and direct light-to-SP conversion is then forbidden.

This concept can be visualized by solving Maxwell equations for a smooth metal-dielectric interface. The resulting dispersion relationship[38] is shown in Figure 2.2, as a plot of the frequency (energy) of the wave versus its momentum parallel to the surface (x axis). The momentum vector of the surface plasmon (k_{SP}) is dependent on the dielectric constant of both the metal (ε_m) and the dielectric above its surface (ε_d), following the equation

$$\boldsymbol{k_{SP} = k_0\sqrt{\frac{\varepsilon_m \varepsilon_d}{\varepsilon_d + \varepsilon_m}}} \qquad \textbf{Eq. 2.1}$$

As a result, the k_{SP} vector will always be larger than the free photons and the two curves do not intersect. This translate into the fact that there will never be a resonance condition where the incident free light, in the visible range, will be able to excite the surface plasmons. Therefore, special coupling schemes need to be devised to allow SPs generation.

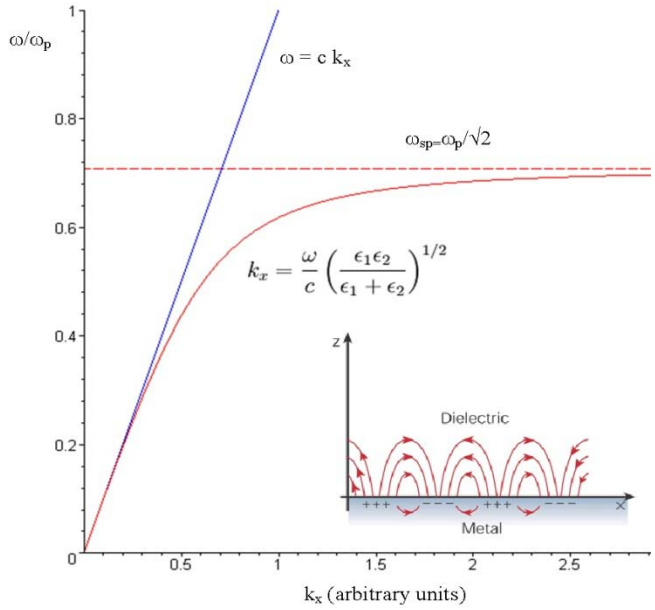

Figure 2.2 Dispersion curve of light in vacuum and surface plasmon. Inset: representation of surface plasmon oscillations [Reprint with permission from [39] and [38]]

The most common configuration for SP-based sensing is the prism-coupling excitation proposed by Kretschmann and Raether (Figure 2.3a).[40] In this case, the condition of resonance is achieved because the evanescent field from the totally reflected light from the prism side extend through the thin metal film (about 50 nm) to launch SPs on the other side of the film. The change of the dispersion curve for the light passing through the prism is shown in Figure 2.3b. The two curves (the SP dispersion and light propagating through glass) now intersect, making it possible to excite the surface plasmons[4].

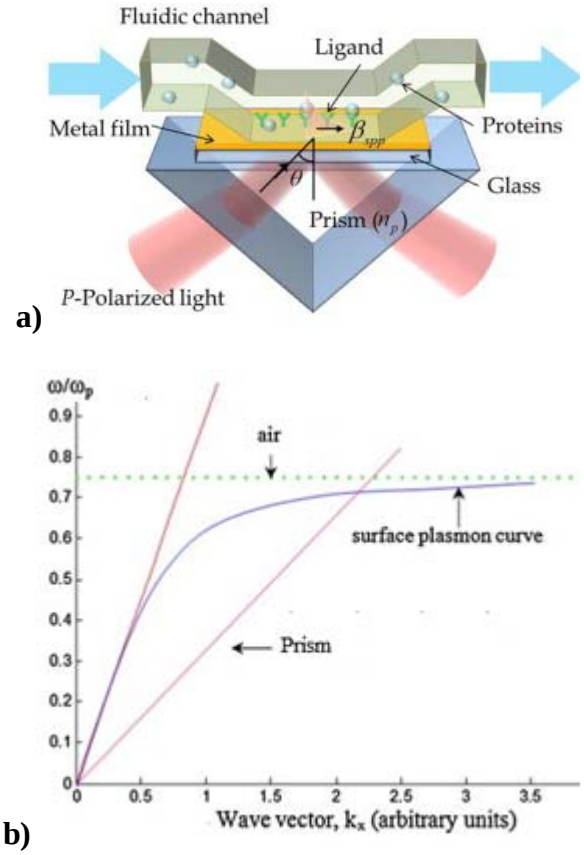

Figure 2.3 a) Kretschmann and Raether configuration, involving the use of a prism for the excitation of SPs. b) Change to the dispersion curve of light due to the introduction of the prism [Reprinted and modified with permission from [41] and [4]]

Another approach to generate SPs is by grating coupling and it employs metal films with sub-wavelength periodic corrugations, as illustrated in Figure 2.4a. These corrugations can be periodic arrays of either metallic nanoparticles supported in a dielectric substrate or sub-wavelength holes (nanoholes) perforated in a metal thin film.

These nanofeatures are essential to sustain SPs, as can be seen in Figure 2.4b and from Eq.2.2.The periodicity vector (G) from the periodic structure can be added to the momentum of the incident light (k_x), which allows a momentum-matching (resonant condition) with the SP modes[4].

$$K_{SP} = K_x + G \qquad \text{Eq. 2.2}$$

where

$$G = \frac{2\pi}{\Lambda} \qquad \text{Eq. 2.3}$$

The periodicity vector is defined in Eq. 2.3, where Λ is the periodicity of the structure.

For normal incidence ($k_x = 0$) and a square array of holes, the position of the resonant peak is given by

$$\lambda_0 = \frac{\Lambda}{\sqrt{(i^2+j^2)}} \cdot \sqrt{\frac{\varepsilon_d \varepsilon_m}{\varepsilon_d+\varepsilon_m}} \qquad \text{Eq. 2.4}$$

where *i* and *j* represent different diffraction orders.

The geometrical characteristics of the structures (type of corrugation (holes or slits), shape and periodicity[42, 43]) can be then tailored to control the resonance energy of the SPs.

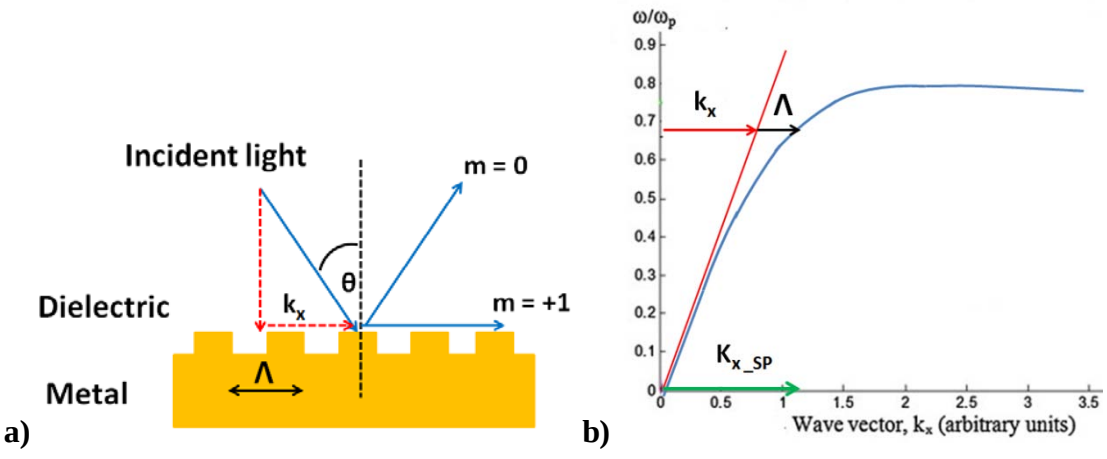

Figure 2.4 a) Grating-coupling configuration: the corrugations mediate the excitation of SPs. b) Change in the dispersion curve of light due to the periodic grooves on the metal surface [Reproduced and modified from[4]]

There are many other platforms and configurations able to excite and sustain SPs. For instance, waveguides[44] and nanoparticles[9, 10] in solution, for example, are among the main alternatives studied in the plasmonic and biosensing literature.

However, for the purpose of this thesis, only the Kretschmann configuration and the planar nanoholes arrays on gold will be addressed with further details. Moreover, the Kretschmann sensing scheme constitute the gold standard in the plasmonic field for the performance (explained in Section 2.3) achieved with the commercially available Biacore® SPR system[21]. This detection platform can achieve a bulk resolution of 10^{-7} RIU (refractive index unit) and a surface LOD (limit of detection) of 0.1 pg/mm² [45].Therefore the sensing performance of subwavelength holes arrays will be compared to the Kretschmann configuration.

2.2 Surface Plasmon for Biosensing: Detection Schemes

Plasmonic materials constitute one of the most explored platforms for chemical sensing: in fact, any architecture that support SPs are a potential chemical sensor, and proof-of-concept molecular detection has been demonstrated for virtually all of them[32].

The reason relies in the fact that SP are tightly confined to the metal surface on which they are sustained; any small variations in the physical properties at the boundary between the metal and the dielectric will cause a drastic change in the SPP wave characteristic[2, 33]. In particular, as can be seen from Eq. 2.1 the momentum of the SP (K_{SP}) is highly dependent on the environment above the metal surface; a perturbation of the refractive index n, ($\varepsilon = n^2$) due to the presence of a liquid or due to molecular absorption, will cause a detectable change in the plasmon dispersion. This is translated into a variation in the resonance

condition for exciting the SP[46]; therefore, the spectral behaviour of the light interacting with the surface plasmon can be monitored, and the variation can be used for a qualitative and quantitative detection of molecules near the surface.

Several approaches have been introduced to detect and quantify these changes, depending on which platform is being used as biosensor and the excitation method. Hereafter, the three most common approaches used with both the Kretschmann and the nanoholes arrays configuration will be explained: angular, wavelength and intensity interrogation.

In a typical experiment using the Kretschman configuration, a p-polarized monochromatic light source is used to excite the plasmons, and the intensity of the light reflected from the prism side (reflectivity, R) is measured at different angles (θ) of incidence.[2, 3, 41] An R vs θ plot, as in Figure 2.5b, will present a minimum at the angle where the incident light is absorbed to generate SPs, defined as SPR angle θ_{SPR}. As mentioned earlier, the position of θ_{SPR} is dependent on the effective refractive index at the metal surface: the adsorption of molecular species at the top, as illustrated in Figure 2.5a, will changes the conditions for SP, provoking a shift in the θ_{SPR} position in the reflectivity curve. Because the quantity $\Delta\theta$ is the measured response of the sensor, this approach is normally referred as angular interrogation.

For grating-coupling SPR (Figure 2.6c), the measurements of θ_{SPR} can also be realized using monochromatic radiation in angular interrogation (as described before for Figure 2.5b). However, in most cases reported the periodic plasmonic structures are used in the easier wavelength interrogation mode, represented schematically in Figure 2.5d.

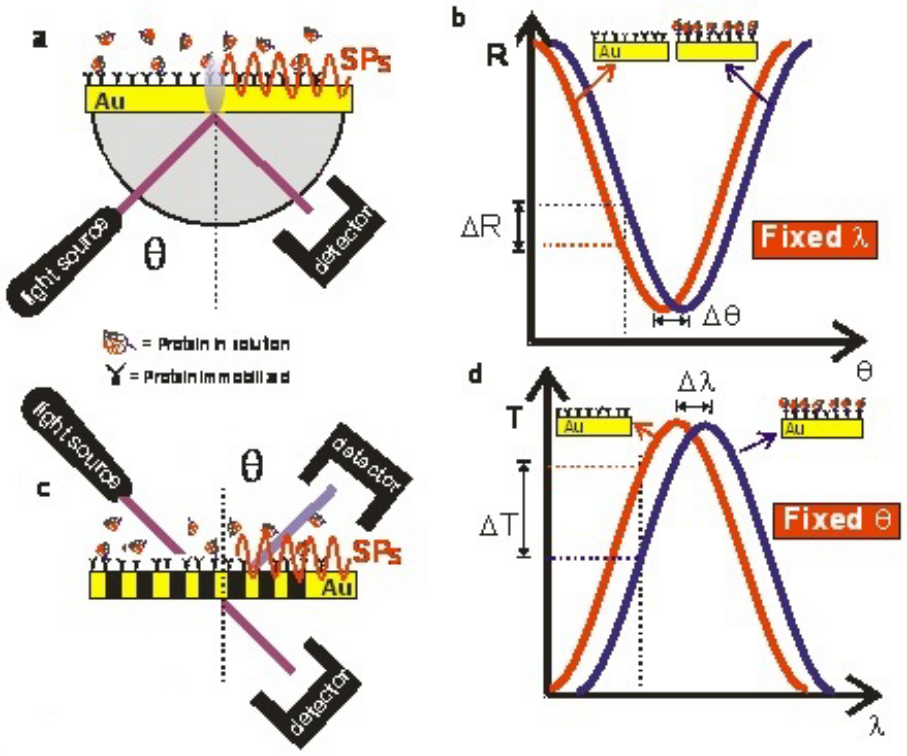

Figure 2.5 a) Prism-based configuration scheme and b) the plot of the resulting angular shift detection. c) Nanohole arrays configuration and d) the plot of the wavelength shift detection. [Reproduced with permission from [32]]

In this case, the surface is illuminated with white light at a fixed angle (normal incidence is the most common), and transmission peaks reveal the resonance conditions and their shift $\Delta\lambda$ due to refractive index change.

This configuration is possible in the case of periodic nanohole arrays because the SPs allow enhanced light transmission(T) at particular wavelengths, a phenomenon known as "extraordinary optical transmission" (EOT)[14, 15].

The physics behind this process discovered by Ebbesen in 1998 is still not completely understood[47]. Broadly speaking, the SPs propagating on the surface can channel through the holes and de-couple from the metal surface on the other side, generating a radiation related to the resonant conditions responsible for the SPs excitation itself. To summarize, if this

radiating light is collected with a spectrometer, it will be observed a peak in transmission intensity occurring at the wavelengths that match the exciting resonance conditions[48].

A third interrogation mode, normally referred to as intensity interrogation, can be applied in both plasmonic platforms described so far[2, 3]. This arrangement is represented in Figure 2.5b and Figure 2.5d by the vertical dotted lines crossing the spectra. Respectively, the changes of light intensity in the reflectivity at a fixed angle (ΔR for Kretschmann configuration) or the light transmission at fixed wavelength (ΔT for nanoholes arrays) can be monitored. The fixed angle or wavelength is chosen to be close to the minimum (or maximum) peak and in the steepest part of the curve to improve sensitivity.

The intensity interrogation mode is widely used in biomedical research, since it allows the determination of real-time binding kinetics. A typical SPR affinity plot is represented in Figure 2.6, where reflectivity changes from a fixed angle Kretschmann experiment were plotted against the elapsed time.[2, 45, 49]

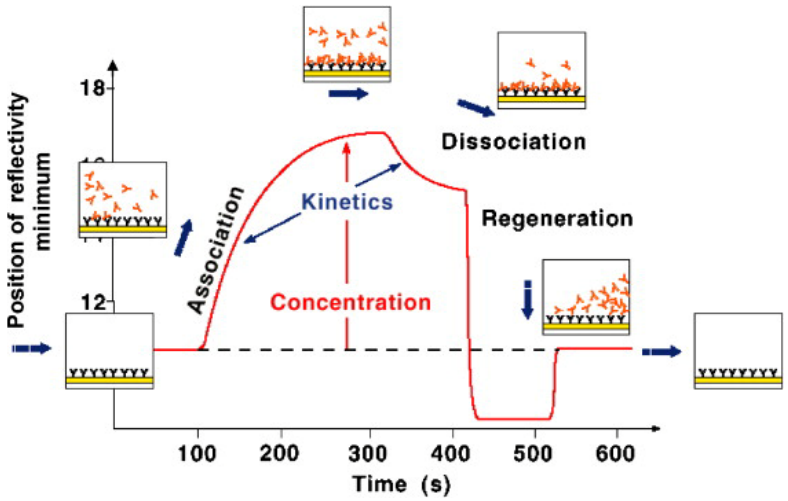

Figure 2.6 Typical kinetics curve obtained from the prism-coupled Biacore® SPR system. [Reproduced with permission from [49]]

The intensity interrogation with the Kretschmann-Raether SPR configuration is also the most common arrangement to study biomolecular interactions and affinities, available commercially from Biacore®,[21] and it constitute the benchmark for any other SPR-based biosensor.

As the main goal of the ongoing research is to match the performance of nanohole arrays with the Biacore® standards, a brief description on how plasmonic biosensors performance can be evaluated will be outlined in the next section.

2.3 Performance of Plasmonic Biosensors

As mentioned, the general objective in the plasmonic biosensing field is to produce platforms that can outperform the commercial state-of-the-art, providing additional advantages, as analysis speed, device miniaturization[5, 6] and multiplexing[7].

Several contributions participate in the outcome of a sensing platform, varying from the design and quality of the fabricated periodic structure to the method used for the detection of the sensor response, including the overall setup and instrumentation.

Figure 2.7illustrates the evanescent nature of the intensity (E^2) of the SP field, decaying exponentially from the metal surface.[2, 33] As mentioned in the previous section, the characteristics of the SP-mode depend on the refractive index within this decaying field.[46] In the case Figure 2.7a, the refractive index inside the SP field is homogeneous and the sensor is said to respond to *bulk* refractive index variations. In Figure 2.7b, on the other hand, an adlayer of adsorbate is formed, creating a local *surface* refractive index change[2, 33].

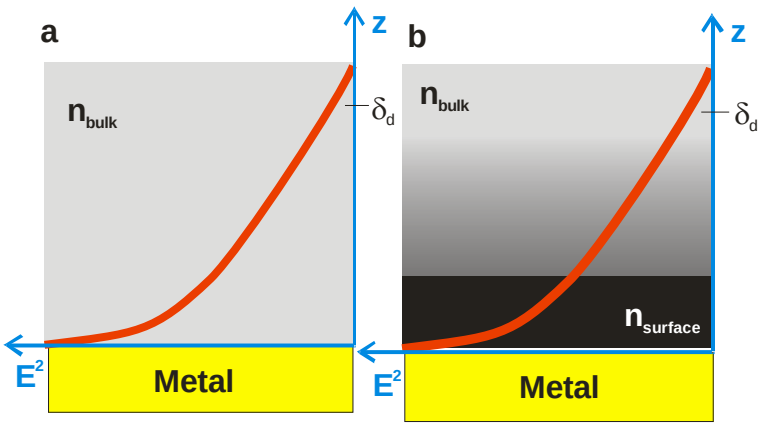

Figure 2.7 Schematic of the decay field profile (field intensity (E^2) variation in the z-axis); a) in the absence of adsorbates, where n_{bulk} correspond to the refractive index of the bulk liquid; b) in the presence of adsorbates with a refractive index $n_{surface}$

The simplest quantitative performance parameter of a plasmonic sensor is the sensitivity to bulk refractive index changes: bulk sensitivity, S_b.[2, 3] As represented in Figure 2.8, in typical experiments, the plasmonic structure is exposed to liquids with different refractive indexes, and the shifts in the SPR are recorded (Figure 2.8a).The bulk sensitivity (S_b) is the slope of the plot between the change in the measured quantity ($\Delta\theta$, $\Delta\lambda$, ΔT) vs. the refractive index of the liquids(Figure 2.8b).

It is important to point out that the sensitivity of the SPR sensor is wavelength dependent; therefore, the direct comparison of bulk sensitivities need to be considered in the same range of wavelengths[2].

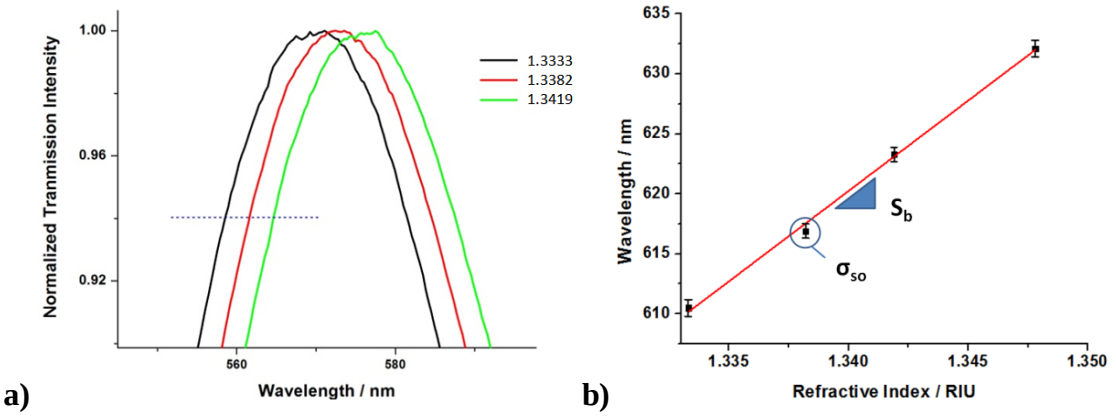

Figure 2.8a) SPR spectra obtained from a nanohole array immersed in different liquids; b) wavelength shift plotted against the refractive indexes. the bulk sensitivity (Sb) is the slope of this line.

Arrays of metallic nanoholes present a comparable S_b-values with the prism-based sensors in angular[50], intensity[18] and phase interrogation mode[51] (looking at the change in phase between p- and s-polarization of the reflected light). However, angular and phase interrogation configurations are not the best for easy improvement of optical design, miniaturization and multiplexing. On the other hand, wavelength interrogation ($\Delta\lambda$,Figure 2.5d) would easily account for those advantages, but grating-based SPR sensors are less sensitive to bulk refractive index variations in this configuration[22, 30, 52].

However, in most cases plasmonic platforms are required to detect surface binding events rather than bulk refractive indexes. Therefore, S_b is not always the best parameter to quantify SPR sensor performances. A useful index for those cases will be then the surface sensitivity (S_s), defined as the sensor response determined by an amount of adsorbed molecules on the surface.[2, 3]

Consequently, other parameters as the adlayer thickness and the surface coverage (Γ), given in number of molecule per mm^2 or mass per mm^2, are then required to evaluate S_s values.

This type of information are not easy to obtain, and independent measurements with quartz crystal microbalance (QCM)[53]or ellipsometry need to be performed. Biacore®, for example, used scintigraphy with^{14}C-labeled proteins to obtain an average unit response value per protein surface coverage[54].

The sensitivity can also be expressed in terms of the sensor response to changes in the analyte concentration (*C*) in solution (concentration sensitivity, S_c). S_c values are obviously dependent on the type of analyte and on the strength of the adsorption constant. Mostly, S_c is reported in SPR sensors for proof-of-concept evaluations. The binding pair biotin-streptavidin is widely used for this purpose, as the interaction between these two proteins is one of the strongest among biomolecules, with a dissociation constant of 10^{-14}M.[55]

Another method recently introduced for proof-of-concept is to evaluate the sensor response in terms of adlayer thickness (S_{st}).In particular, layer-by-layer deposition of positively and negatively charged polymers, such as poly(allylamine hydrochloride), PAH and poly(sodium styrene sulfonate), PSS, have been generally used.[56-60] For wavelength interrogation mode, S_{st} would be given in nm of wavelength shift per nm of adlayer thickness (nm/nm).[61]

It is good to keep in mind that the development of SPR platforms is generally driven towards the detection of the smallest concentration of analytes, including proteins, antibodies and cancer markers, which sizes are in the order of 2-5 nm.[62] This translates into the detection of a very small perturbation within the sensing volume of the SP-field (Figure 2.7). In this sense, the concepts of sensor resolution, *Res,* and limit of detection, *LOD*,

would then be the most appropriated parameters to determine the overall efficiency. The term "resolution" in SPR means the smallest detectable change in refractive index, and it is reported in RIU (refractive index units).[63] *Res* is obtained from the noise in the detector output (Figure 2.8), σ_{SO}, and the bulk sensitivity (S_b in nm/RIU), according to

$$\boldsymbol{Res = \frac{\sigma_{so}}{S_b}} \qquad \textbf{Eq. 2.5}$$

The *LOD*, on the other hand, is defined as the minimum variation of the measured quantity that the sensor can detect with a reasonable certainty (normally taken as 3 times the standard deviation of the signal); the *LOD* in expressed in surface coverage units (pg/mm^2). The ultimate resolution achieved by a state-of-the-art system from Biacore® is reported to be ~10^{-7} RIU and the typical *LOD* is below 1 pg/mm^2;[21] these are the limits to be matched by the researchers in the area developing different SPR platforms.

The performance parameters for sensor evaluation described so far are summarized in Table 2.1. The examples in the table are given for the case of wavelength modulation (Δλ).

Table 2.1 Summary of four performance parameters used in the evaluation of plasmonic biosensors (Γ: Surface coverage, g/mm²; C: concentration, mg/mL; t: film thickness, nm)

	Bulk Sensitivity	**Surface sensitivity**			**Resolution**	**LOD**
	Sb	Ss	Sc	St	Res	
Formula	Δλ/ΔRIU	Δλ/ΔΓ	Δλ/ΔC	Δλ/Δt	σ /S_b	3*σ /Sc
Units	nm / RIU	nm/g mm^{-2}	nm/gmL^{-1}	nm/nm	RIU	g/mL

Experimentally, the resolution (*Res*) is easier to be determined, since it does not require any information about the surface concentration. Improving *Res* can then be achieved by reducing noise and improving the sensitivity of the plasmonic platform[2, 17].

Data treatment algorithms can also be used to decrease the variation in the determination of the system response. For instance, a simple fit of the SPR peak, instead of using the noisier raw data, allow for a better localization of the resonance point. Many other more elaborated statistical approaches have already been implemented to provide a robust monitoring of spectral changes.[20, 64]

However, the majority of the effort in plasmonic sensor research is still centered mostly on improving sensitivity. Particularly for periodic plasmonic structures, the geometrical parameters to be explored include the size of the nanostructures, the distance between the elements of the arrays (periodicity), and the shape of the individual elements[24, 65].The effect of geometric parameters on the sensing performance of nanohole arrays will be explored in details in the first result session (Chapter 5) of this thesis.

2.4 SPR Application for Leukemia Detection

All the favorable properties of SPR-types of sensors, including high sensitivity and low LOD, justify the high research activity aimed at the development of platforms for early diagnostics. To achieve this goal, very often the targets are specific cancer biomarkers (indicators) present in blood. The cancer proteins studied in this thesis were particular antibodies found in human blood serum. The detection of offset levels of these antibodies would infer a positive diagnosis for leukemia, a white blood cell cancer.

2.4.1 Leukemia

Leukemia is the name attributed to the cancer of the white blood cells, or leukocytes. The most common type of leukemia is chronic lymphoid leukemia(CLL), mostly widespread among adults, with the majority being men.[31] The occurrence of the cancer cannot be predicted, but the ability of detecting the related cancer markers at very low concentration can allow early diagnosis and great improvement of survival rate for the patience.[31]

If a person is affected by Leukemia, his/her immune system is highly compromised, and it drastically differentiates from that of a healthy person. In particular, the antibodies distribution became dominated by only one particular protein among the several others present in the human body.

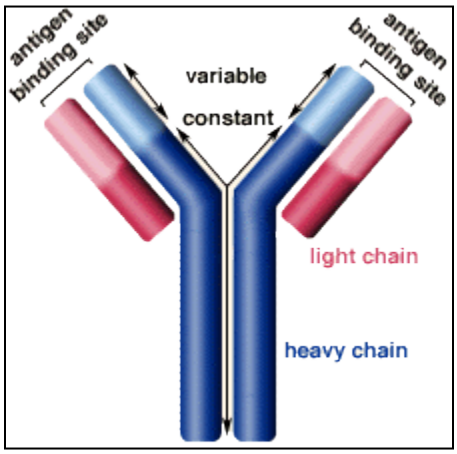

Figure 2.9Antibody structure: in nature there are 5 types of heavy chains (blue), but only two type of light chains (red). [Reproduced with permission from [66]]

Antibodies or immunoglobulins (Ig) are the proteins released by lymphocytes B into the blood to defend the organism from pathogenic factors, such as bacteria and viruses. Even if several classes or types of Igs are present in the immune system, defined on their specificity

and use, those proteins are always composed by the same basic structural units.[66] As seen from Figure 2.9, the heavy chain is the main component and the structural support, while stability and flexibility to the recognition site is given by the light chain.

There are only two genetics types of light chains in our body: kappa, κ and lambda, λ. Only one of the two classes can be expressed in all the antibodies generated by each single lymphocyte cell.[66]

In addition, all the CLL cells within one individual affected by leukemia are clones: that means they are genetically identical. In practice, these constantly duplicating cancer cells will produce only one of the mutually exclusive light chains, λ or κ. It is known that in a healthy individual, on the entire population of normal B cells, the total kappa to lambda amount ratio ranges from 0.26 to 1.65 in serum (measuring intact whole antibodies).[67]The lack of the normal distribution of light fragments is one of the bases for demonstrating/establishing a diagnosis of any B cell tumors.

The normal concentration of immunoglobulines in a healthy person serum can vary between 3 mg/mL to 7 mg/mL. On the other hand, a single monoclonal antibody overproduced by the cancer cells can reach up to 17 mg/mL. Due to the high quantities present in the blood sample, the roadblock in leukemia diagnosis is not the actual detection of the antibodies, but the discrimination of the over-expression of a particular one in respect to the others. This discrimination is normally done in the hospital by looking at the leukocyte cell producing the antibodies, and detecting possible shape and size abnormalities.

On the other hand, SPR can be used to record the ratio between the two chain isotypes of the immunoglobulines, by comparing their absorption on the surface (previously modified with antibody to capture them). Preliminary information about any kind of B cell

anomalies, in particular leukemia, can be then obtained through a quick and cheap, though efficient, analysis. This approach can be largely implemented for screening in medical clinics and improve prognosis of patients.

Chapter 3: Background on the Nano- and Micro-fabrication Methods

3.1 Introduction

In this chapter, the different methods used to fabricate and characterize the sub-wavelength plasmonic platforms, together with the microfluidic chips, will be outlined. The outcomes of the fabrication step were evaluated through scanning electron microscopy (SEM) and energy-dispersive X-Ray spectroscopy (EDX).

Another important aspect for all platforms was their integration into microfluidic chips for the delivery of solutions on top of the sensing area. The designed microfluidic patterns were fabricated by photolithography on a silicon wafer, and used as a template for the polymeric mold.

3.2 Fabrication of Nanohole Platforms

Particularly for the fabrication of nanohole arrays, three different top-down techniques were used:

- Focused Ion Beam (FIB) milling
- Interference Lithography (IL)
- UV-Nanoimprinting

Background and some details about each technique outlined, together with some advantages and limitations, will be explained in this chapter.

3.2.1 Focused Ion Beam (FIB) Milling

Research on periodic plasmonic structures and grating-based SPR sensing has increased drastically in the last few years[1]. The increased activity in this area started in the late 90's and it is correlated to the increased availability of top-down specialized nanofabrication methods, such as focused ion beam (FIB) milling.[68]FIB is a powerful technology for milling, imaging, depositing and positioning features at the nanometric scale[68].

Figure 3.1 Scanning electron micrograph of sub-micron scale crests of the University of Victoria in a Copper TEM grid, fabricated with a Hitachi FB-2100 FIB [Reproduced with permission from [69]]

In brief, a focussed beam of gallium ions, driven by high voltages (~ 40kV), can be precisely directed onto the sample surface positioned inside a vacuum chamber in a computer controlled stage. Sent at high speed, the ions acquire enough momentum to displace atoms from the material upon collisions. Detailed nanofeatures can then be created by finely manipulating the position of the ion beam, the dwell time and the number of expositions to a given area. Figure 3.1shows a UVic logo sculpted on a copper film using FIB.[69]The complex pattern of the logo was input to the FIB machine as a bitmap file. The spatial resolution of the features in Figure 3.1were about 10 nanometers.[70]

Figure 3.2 shows an example of a nanohole array fabricated by FIB: normally, the diameter (d) of the holes ranges between 150nm-300nm; the periodicity, p, defined as the distance center-to-center between the holes, has typical values of 400-650nm, in order to have SP resonance in the visible.

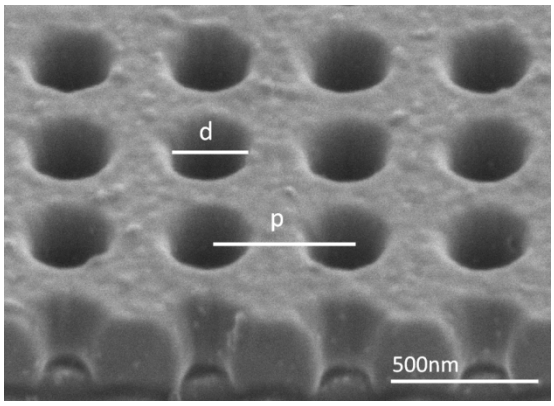

Figure 3.2 Scanning electron micrograph of a nanohole array profile fabricated by FIB. The gold layer is completely milled through, reaching down to the glass substrate.

FIB can also be used for imaging at lower driving potential. However, this is not always a suitable method, since the continuous exposure to the ions beam, required for imaging, can damage the fabricated features. Section 3.2.4will discuss the SEM, which is a common used imaging method that normally does not damage the samples.

FIB is a powerful tool that allows the milling of complex structures, periodic or not, with a high level of detail with nanometric resolution.[70] Therefore, FIB is an excellent method for systematic evaluation of geometrical parameters and fundamental understanding of their effect on the plasmonic properties of the structures; However, FIB is a serial fabrication method that requires a high-cost specialized instrumentation. The expensive instrumentation adds a significant fabrication cost to the samples generated by FIB. Moreover, the FIB method is not suitable for large area patterning, and the typical sensing

area obtained using FIB is of the order of 30 x 30 μm^2.[27] The FIB methodology is clearly too slow and expensive to be considered as viable tools for mass fabrication of plasmonic sensors or large area pattern. Recently, the fabrication focus of periodic metallic structures has changed towards the implementation of other methods, such as interference lithography[71] and UV nanoimprinting[29], that enable to achieve these goals.

3.2.2 Interference Lithography

The large area nanohole arrays studied in this thesis were fabricated using a combination of conventional interference lithography and lift-off processes.

Interference lithography derives from the superimposition of two or more coherent light beams. There can be many configurations to produce an interference pattern, and Figure 3.3 depicts two of the most used.[30, 72]

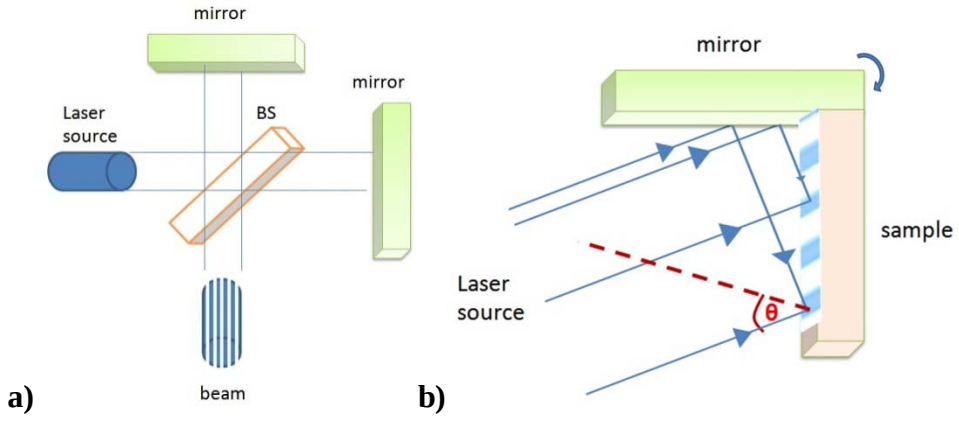

Figure 3.3 a) Schematic of a conventional light interference and b) the scheme for a Llyod-mirror interferometer implemented in the setup for the nanohole fabrication and c) (following page) the actual scheme used for this project

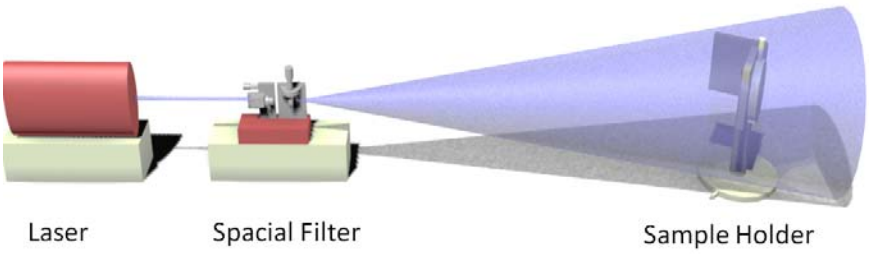

c)

Figure 3.3a depicts a common interferometer, where a light beam is split in two (using a beam splitter), and each beam half travels through different paths until they are reflected by mirrors and then superimposed in a particular target. Figure 3.3b, on the other hand, shows an alternative interferometric scheme that involves the use of only one mirror. In this case, one portion of the same wave front is freely propagating, while the other portion is reflected by a mirror first. The interference pattern occurs where these two beams superimpose, and the sample is positioned in that region. This configuration is called Lloyd–mirror interferometer[71] and it has been used in this thesis due to its simplicity.

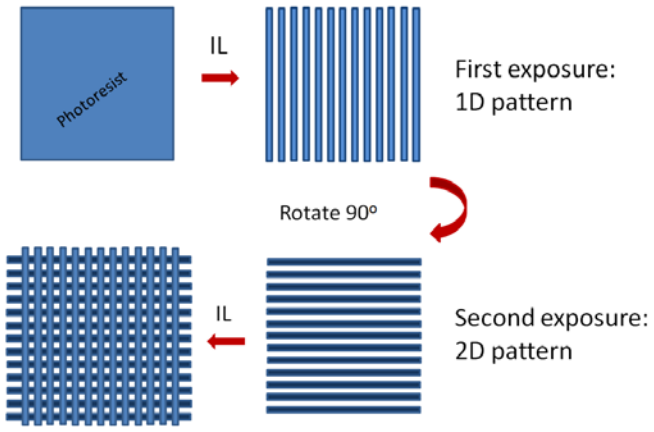

Figure 3.4 Schematic on how generate 2D patterns with IL; after the first exposure, the sample is rotated by a desired angle and expose again to the interfering light

A more detailed scheme of our particular Llyod setup is shown in Figure 3.3c. A spatially filtered and expanded laser beam impinges onto a stage consisting of a mirror perpendicularly attached to the substrate holder (as presented in Figure 3.3b) with a rotational degree of freedom (Figure 3.3b and c).

The alternated regions of light (constructive interference) will sensitize a particular polymers, called photoresist, that are sensitive to light and react to its exposure by forming new cross-link bonds in between their polymeric chains. The photoresist is spin-coated beforehand on the sample surface under yellow light, to avoid any pre-exposure to UV rays; the overall thickness will vary depending on the material used and on the desired height for the final structures.

With IL is also possible to create 2D periodic structures, as it can be seen from the cartoon in Figure 3.4. Here the photoresist is exposed once to the interference pattern, consisting of a series of parallel lines at a periodic distance. If the sample is then rotated (on the axis perpendicular to the incident beam) by 90^{o}, and expose again to the same interference pattern, a 2D grid is produced. Depending on the rotational angle chosen, the pattern will have different lattice geometries; the most common are square lattice, after rotation of 90^{o}, and hexagonal lattice, after a 60^{o} rotation.

Although the Llyod configuration allows a certain degree of control over the geometrical characteristic of the sample, these parameters are also limited by the setup itself. First of all, only periodic structures can be fabricated with the IL technique. In addition, although the total area prepared can be quiet large, it still depends on the beam size, the size of the mirror and the laser coherence length.

In particular, the periodicity (Λ) of the nano-features is one of the most important characteristics in terms of the application of the samples as plasmonic platforms, since it is mainly this value that determines the conditions of SP resonance.[2] Theoretically, the periodicity of the IL fabricated structure is well defined by the equation[73]

$$\Lambda = \frac{\lambda}{2\,\mathrm{Sin}\theta} \qquad \textbf{Eq. 3.1}$$

being λ the laser wavelength and θ the angle between the two interfering beams (defined in Figure 3.3b). On the other hand, experimentally, it is impossible to match the theoretical prediction, primarily, because the value of θ is normally far from 90^{o}, lowering the value of Λ achievable. In addition, the photoresist resolution[74], which depends on its polymeric composition, and the overall stability (thermal and vibrational) of the setup, are practical limitations that can affect the quality of the fabricated structures. In our setup, it was possible to produce very uniform, 1" x 1" large area nanohole arrays with various periodicities, ranging between 500to 700nm.IL is indeed a powerful bench-top method that can be used to produce large uniform and reproducible periodic plasmonic structures.

3.2.3 UV nanoimprinting

Another type of plasmonic structures employed in this thesis was flexible plastic 2D nanogratings, fabricated on thin sheets of polyethylene terephthalate (PET) or polyvinyl acetate (PVA). These samples can be commercially fabricated in large amounts, as they rely on an industrial procedure based on the roll-to-roll technology (*http://www.technologyreview.com/news/417307/roll-to-roll-plastic-display/*). The grating

pattern is imprinted on the plastic surface using a UV lacquer procedure (UV nanoimprinting). The general steps involved in UV nanoimprinting are illustrated in Figure 3.5[75].

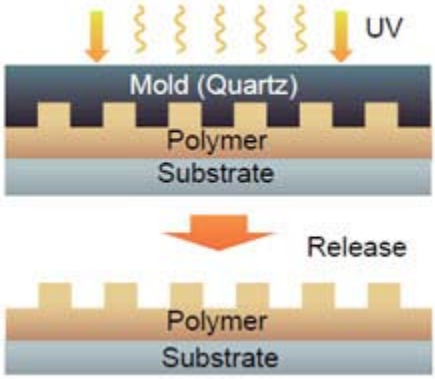

Figure 3.5 UV nanoimprint process scheme: the low cost and the mass fabrication is due to its simplicity. [Reproduced with permission from[75]]

A large area mold with the predefined topological patterns, normally fabricated by e-beam lithography or FIB, is pressed together against the plastic substrate, coated with a photosensitive material. The pattern is, therefore, transferred by mechanical deformation. The system is then illuminated by UV light to make the change on the photoresist permanent (see Figure 3.5). The last step is then the evaporation of the chosen metal.

Figure 3.6 shows the schematic and the SEM of the structures studied in this thesis. For simplicity, the structure in Figure 3.6will be called nanohole (NH)-like.

UV nanoimprinting has several qualities: first of all, it is a simple and relative low cost method.[76] It has already been implemented in large area fabrication of large sample volume, making it a good fit for possible industrial applications.[75, 77]

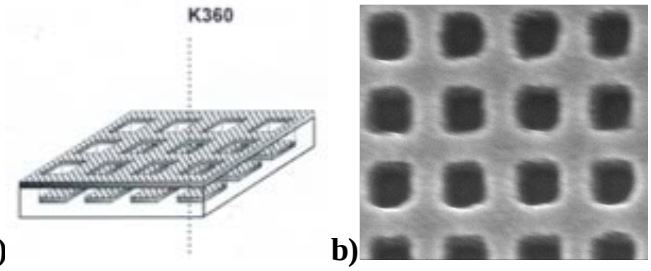

Figure 3.6 Two different representation of the structure employed; a) cartoon and b) SEM micrograph of the large area nanohole

On the other hand, unfortunately, some problems were encountered with this technique. In particular, the resolution of the method is estimated to be about 10nm[77], but this value can easily increase, mainly by the presence of defects on the surfaces involved or by trapped air bubbles between the mold and the photoresist. Moreover, the mold itself has a tendency to quickly degrade, due to the medium-high pressure involved, leading to less sharp features. Some comments on the uniformity of the gratings and sample-to-sample variability will be outlined in Chapter 6.

3.2.4 Scanning Electron Microscopy (SEM)

Scanning electron microscopy (SEM) is the most appropriated technique to evaluate the quality of the fabricated nanostructures.[78] As the name suggests, to be able to visualize features with this instrumentation, a focused electron beam is scanned over the sample placed in a vacuum chamber. Figure 3.7 represent the main processes involved in the interaction of electrons with the material of interest. The images are produce by collecting the back-scattered and secondary electrons expelled from the surface being bombarded.[79]

The back-scattered electrons are generated directly by the incident beam hitting the sample; those particles, expelled from the inner orbitals, have high kinetic energy and carry the

information about the morphology of the sample, as well as a general information about the atomic composition of the material (refer to Section 3.2.5 for actual determination of atomic composition).

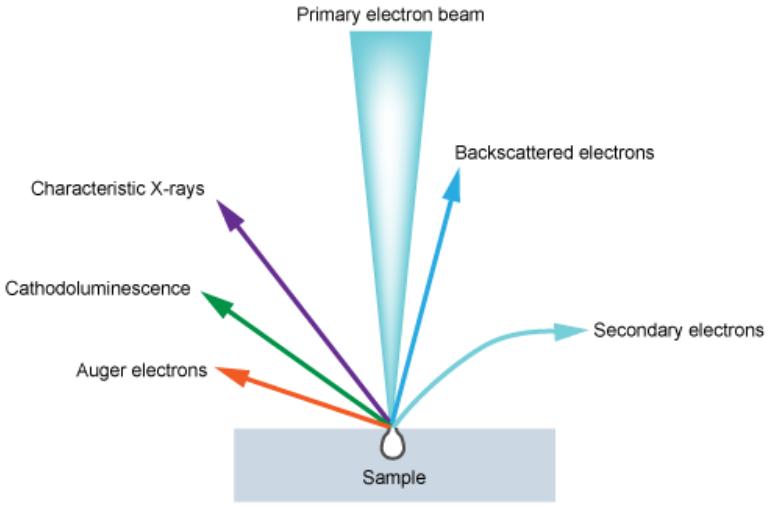

Figure 3.7 Electronic composition for a SEM image. [Reproduced with permission from 62]

The secondary electrons, on the other hand, are the ones generated in a two step process: an electron coming from the source hit and displace a/some electrons inside the material that consequently knock a second electron off the surface. Those charged particles originate normally from the most superficial layers, adding details to the morphological image: the features can then be seen at a very high resolution.

3.2.5 Energy-Dispersive X-Ray Spectroscopy

EDX is an analytical technique used to determine the atomic composition of a material or compound. The X-ray radiation is sent to bombard the material under study. The high energy photons eventually knock off one of the core bound electrons, creating a

vacancy in a inner orbital shell that is rapidly filled by one of the outer electrons. the energy difference from the relaxation is released and captured by the detector.[80]

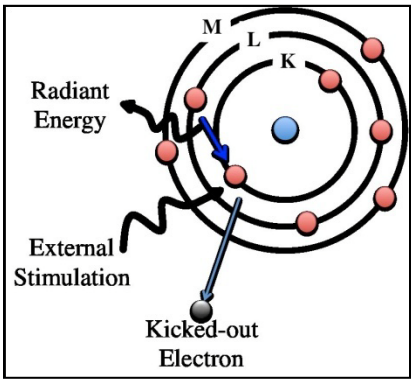

Figure 3.8 Schematic of the EDX process [Reproduced with permission from [80]]

This technique is based on the fact that the electrons on each atom are bound in a unique way to its nucleus, allowing an elemental characterization through the specific energy released from these interactions.

Figure 3.8 represent the different energy levels associated with different orbitals; the electrons belonging to the K shell, being the closest to the nuclei, will be the ones releasing the most energy. To give an example, the value for the most intense transition (Kα) for Gold is 68.805 KeV, while for Silica is 1.740 KeV.[80] This clear difference was used to define the color map in Figure 3.9, obtained through the Hitachi-4800 SEM setup (source of the striking beam) in conjunction with a Bruker X-ray detector. It was possible to see the gold surface as “red”, while the silica from the glass underneath was depicted as “green”: this confirmed the complete milling of the gold layer. This aspect is very important, as the plasmonic characteristic and behaviour of the sample would be different if part of the gold

layer would remain at the bottom of the wells. This technique was used to confirm that the protocol used with the FIB was consistently achieving the desired results.

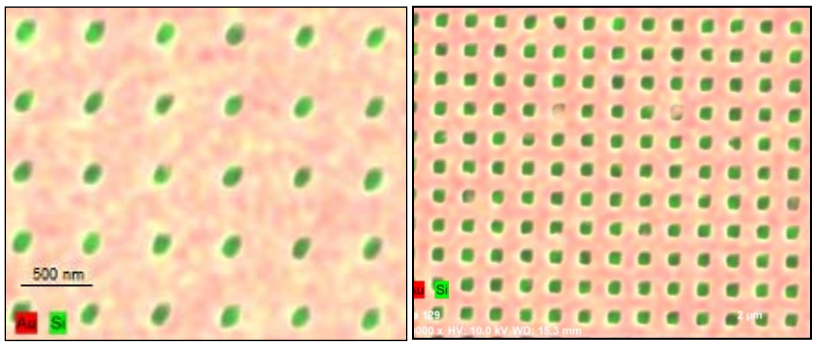

Figure 3.9 EDX images obtained for gold surfaces with nanoholes on glass substrates

3.3 Microfluidic and Photolithography

The delivery of solution to the plasmonic sensing surfaces was realized using the microfluidic technology. The fabrication of the microfluidic chip involved several steps: first, a silicon master plate was made by photolithography[81], reproducing the negative of the pre-defined microfluidic scheme (mask). After that, a flexible polymeric mold was created using this master, sealed onto the gold surface and employed for the liquid delivery.

The design of the microfluidic scheme involved several considerations, and Figure 3.10 illustrate three important parameters: the width, w, of the channel (represented in white); the spacing, s, between channels and d, the diameter of the small reservoir.

First of all, a proper spacing between channel *s* (120μm) was chosen to obtain enough separation between the sensing elements, as well as enough surface contact between the final mold and the gold surface; since proper adhesion is really important to avoid possible leaks and solution mixing between channels.

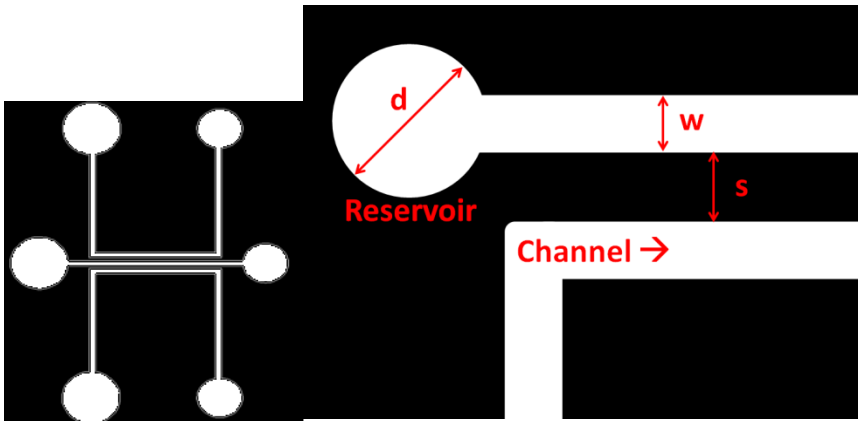

Figure 3.10 Picture of the photolithography mask used and enlargement of a detail to show the parameters considered

The width of the channels, *w* (250 μm), on the other hand, was made large enough to reduce flow resistance, and, most importantly, to have enough space to position the nanohole arrays sensing elements right in the middle of the channel. There are two advantages in doing so: first, at the middle of the channel, the flow experienced on top of the array should be completely laminar; second, light diffraction by the wall of the channels can be excluded during the collection of the optical data, eliminating possible interferences in the transmitted spectra.

The diameters of the circular reservoirs, *d*= 0.9 mm and d= 1.1 mm, were slightly bigger than the diameter of the connecting micrometric Teflon tubes (1/16inch outer diameter). The larger value for the outlet reservoir was to decrease the resistivity of the flow.

The length of the channels themselves was chosen by taking into consideration the whole experimental apparatus used for the measurements (see Section 4.3.1). In another words, it was important to allow the microscope 50x objective lens to access every spot. A

length of 1mm and horizontal expansion of 2mm were realized, as limit to those two measures was only the size of the gold slide itself (2.54cm x 2.54cm).

With the mask ready, the silicon master plate reproducing the final designed pattern was then fabricated by photolithography.[82] Photolithography is the process that uses diffuse UV light to write patterns on hard substrate by sensibilizing a photoresist spin-coated on the surface; a simple photolithography scheme is reproduced in Figure 3.11.

As it is possible to see, there are two types of photoresist: 1) a positive photoresist, in which the regions exposed to UV radiation cannot be removed by a developer solution, remaining on the substrate and producing the positive image of the mask; 2) a negative photoresist, which will generate a negative image of the mask.

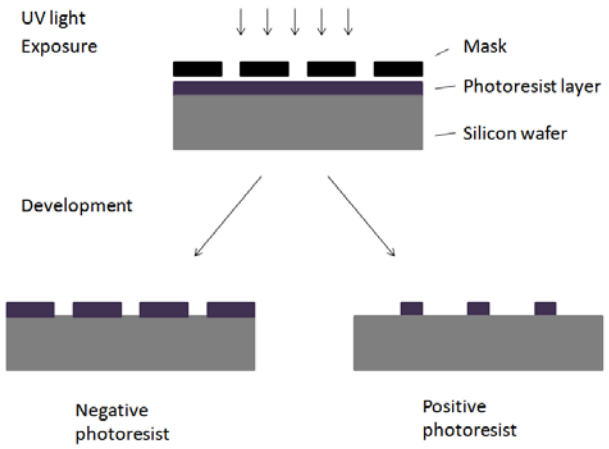

Figure 3.11 Schematic for a photolithography process

As final step, the wafer prepared was then used as a template to produce the microchannel mold, made by polydimethylsiloxane (PDMS), as shown in the scheme in Figure 3.12.[83]

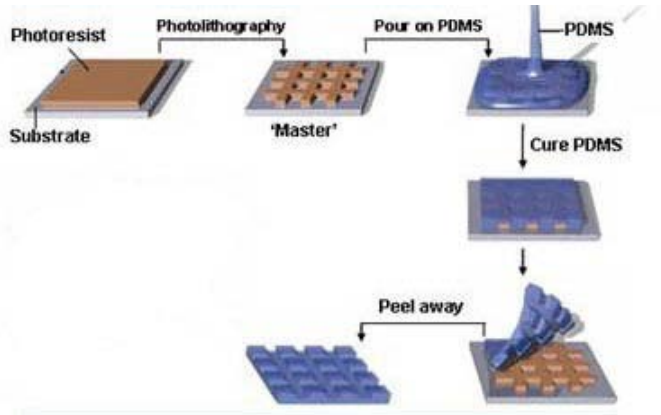

Figure 3.12 Schematic of a typical microfluidic chip fabrication with PDMS. [Reproduced with permission from[83]]

This particular silicon-derived material is widely chosen because of its transparency, due to the nature of the experiment, and for its impermeability. Since PDMS is highly hydrophobic, aqueous solutions cannot infiltrate inside the polymer, avoiding swelling the channel and damaging the structures.

Briefly, the PDMS need to be degassed under vacuum, before and after being in contact with the master silicon plate. It is then placed in the oven for the curing step, and once cooled down, it can be gently peeled off the master for use.

Chapter 4: Experimental Setup

In this chapter, the instruments, materials, conditions and procedures used in the experiments will be outlined. First, the specifics of the fabrication of the three plasmonic platforms studied in this thesis, nanoholes fabricate by FIB; large area nanoholes made by IL; and nanoholes on plastic substrate obtained by UV nanoimprinting, will be discussed. Secondly, the experimental setups and detection schemes of the optical systems will be described, together with the data analysis and post-processing algorithms. At last, the different types of surface chemistry employed for the modification of the gold layer will be discussed, together with the solutions preparation, handling, and protocols for the sensing experiments.

4.1 Sample Fabrication

4.1.1 Fabrication of Nanohole Arrays by FIB

The FIB system was an Hitachi FB-2100 FIB, capable of 3-6nm resolution and 90,000 magnification.[84] The principle of the technique were described in Section 3.2.1.The plasmonic platforms fabricated by FIB were nanoholes arrays milled on gold coated glass slides. The slides were 1 square inch (FEI-DB-234, from Platypos-technologies) glass coated with a 100nm thick gold layer. The gold film was deposited on top of a 5nm chromium layer, to improve the adhesion of the gold film.

Independent of the geometrical characteristic of the fabricated holes, the fabrication conditions were found optimal at 75number of passes, with 10μs dwell time for each scan,

using a focused beam of 40kV at 30μA.Both the gold and the chromium layers were completely carved throughout using these milling conditions.

Figure 4.1shows some examples of images taken with an Hitachi- 4800 scanning electrons microscope, capable 1- 2nm resolution at optimized working conditions.[85]

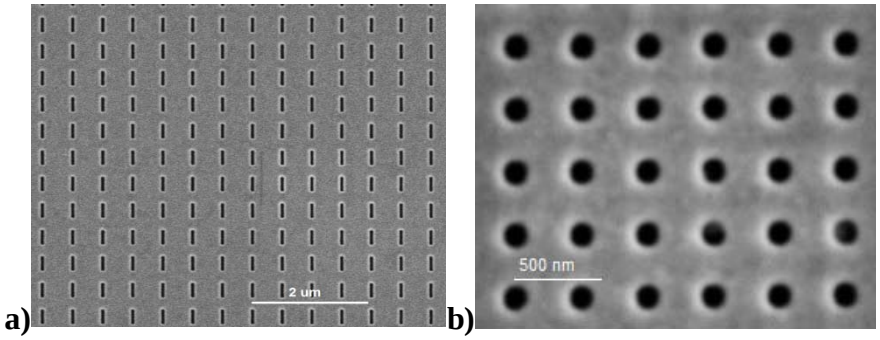

Figure 4.1 SEM images of two samples of nanoholes arrays fabricated by FIB

The SEM images were obtained with 1kV driving potential for the focused beam, and with a 13000x and 22000x magnification, respectively (i.e., an imaging of a 100 μm human hair would have a diameter of half meter for this magnification conditions). Figure 4.1a depicts an array of rectangular holes, 50nm of width and 250nm of length, with a periodicity of 400nm.Figure 4.1bpresents a close-up of a circular nanoholes array. The hole diameter was 200nm in diameter and they were spaced by 400nm apart.

4.1.2 Large Area Nanoholes Fabricated by IL

A positive 550nm-thick photoresist layer (SC-1827, Room and Haas) was deposit onto a glass slide and exposed twice to the same interference fringe pattern, upon rotation of the sample by 90º, to produce a 2D square lattice template (as described in Section 3.2.2 or see Figure 3.4). The blue visible light (457.9nm) from an argon ion laser (90CFred,

Coherent) illuminated the sample with a dose of 65mJ/cm^2. The cured photoresist was then exposed for 40 seconds to its commercially available developer (Microposit 351, Rohm and Haas, 1:3 diluted in water) to reveal the pattern. Figure 4.2a shows the scanning electron microscopy (SEM) images of one of the templates made in photoresist. In Figure 4.2b the final large area nanohole array, obtained after gold deposition and liftoff, as described in section/figure 3.x, can be seen.

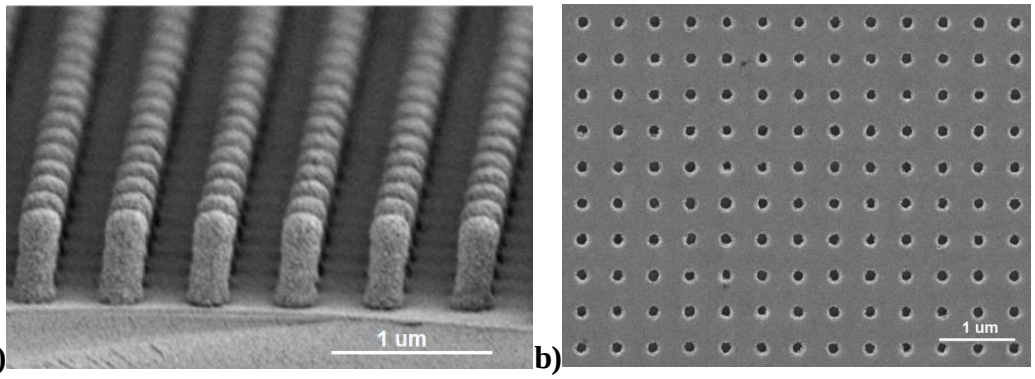

Figure 4.2 SEM image of a) photoresist template and b) large area (2cm by 2cm) nanoholes array after gold deposition and photoresist removal

The periodicity of the columns was 600 nm, with a hole diameter of 230 nm. It is important to notice how sharp and vertical are the sides of the column. The large aspect ratio (height/diameter) of the columns is fundamental for the realization of cylindrical, well-defined nanoholes (as in Figure 4.2a).The final step of the nanohole array fabrication involve the deposition of an 80 nm thick gold film by electron beam sputtering (EvoVac by Angstrom Engineering).The photoresist template was removed with acetone (lift-off) to generate the gold nanohole array. All the IL samples were fabricated by Dr. Jacson Menezes, a postdoctoral fellow at the Brolo group.

4.1.3 Nanoholes on Plastic Fabricated by UV nanoimprinting

Ready-to-use grating structures (with metal already deposited on the plastic grating) were obtained from (Louisenthal GmbH). The samples were covered by an 80 nm thin gold layer. Because of the poor adhesion between the plastic and the metal film, a new set of samples were fabricated in our laboratory using bare plastic gratings obtained again from Louisenthal GmbH. The metal deposition step were realized using our e-beam evaporator (EvoVac by Angstrom Engineering),but, in this case, a 2 nm chromium layer was deposited before the 80 nm gold layer to improve the stability of the samples.

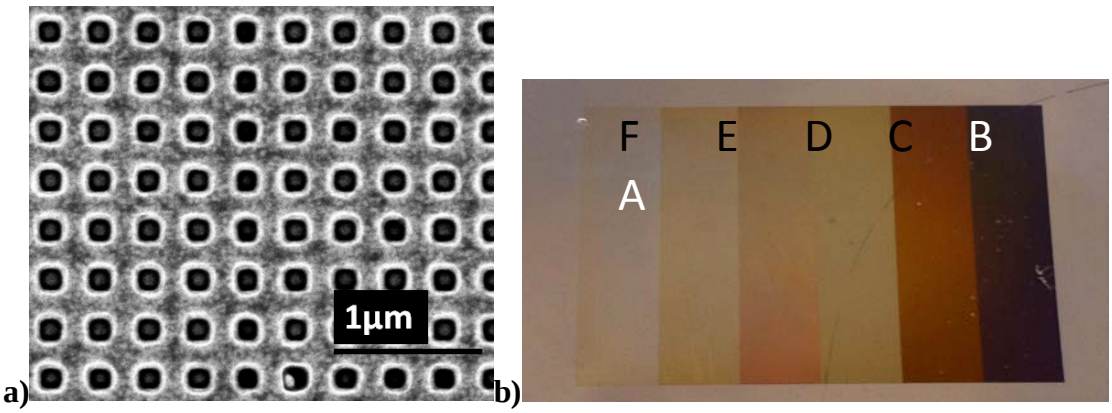

a) **b)**

Figure 4.3 a) SEM micrograph of nanoholes made by UV nanoimprinting; the size of the feature is 200 nm and the periodicity is 330 nm. b) Photo of the whole substrate showing the six different gratings and their labels

Figure 4.3a shows a SEM micrograph of one of the structures used; the size of the square features is 200nm x 200 nm, while the periodicity is 330nm. Figure 4.3b, on the other hand, is a picture of the different gratings, with distinct periodicities, and, consequently, different colors. In total, 6 different grating structures, with specific geometric characteristics were

used and labeled from A to F. The gratings geometrical parameters, as periodicity and hole dimensions, were determined by SEM, and they are summarized in Table 4.1.

Table 4.1. Geometrical characteristics of the nanoholes gratings studied

	Size/nm	**Periodicity** / nm
A	300	400
B	200	330
C	100	240
D	150	400
E	100	320
F	-	-

4.2 Photolithography and Microfluidic chip

In the specific of this photolithography process, the positive photoresist SU-8 (Microchem) was spin coated over a 4 inches silicon wafer, and pre-baked on a hot plate (65 ^{o} and 95^{o}) for a total of 35minutes. After being aligned under the mask, the polymer was exposed for 120 seconds to diffused UV light. A post-baking step (65^{o} and 85^{o}, for a total of 12minutes) was necessary before developing (removing) the material not exposed to light.

The details of the procedure are available on the photoresist supplier website, Microchem, and it was verified that satisfactory results were achieved: Figure 4.4a demonstrates that features with clear edges were obtained and with appropriate thickness (~ 0.1 mm). To create the mold in PDMS, the polymer was first placed under vacuum for 20minutes, to release any major gas in the matrix. After being poured over the silicon wafer, to avoid any bubble, it was placed under vacuum for another 20minutes. The wafer was then

cured in the oven for 25minutes at 80^{o}C; once cooled down, it was then peeled off and stored. The final assembly of the microfluidic chip on the nanohole array gold sample can be seen in Figure 4.4b.

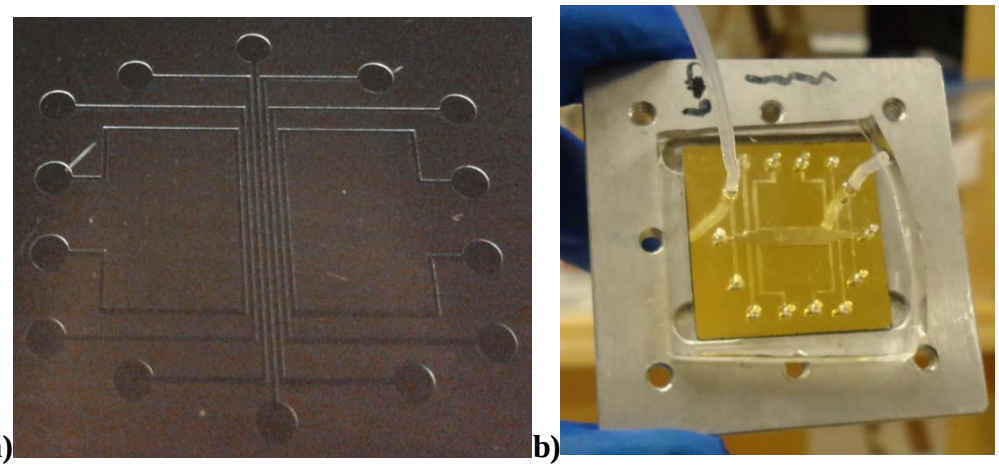

Figure 4.4 a) Image of the silicon master plate produced by photolithography. b) Image of the PDMS microfluidic chip assembled onto the gold nanoholes substrates; one inlet and one outlet teflon tubings for microfluidic are also shown

4.3 Optical and Chemical Sensing Setups

4.3.1 Transmission Detection

One of the main advantagesof SPR biosensor based on gratings, such as nanoholes arrays, is the possibility of working in both normal transmission and wavelength interogation mode (Section 2.2). As mentioned before, the simpler optics of this configuration improves the chances for miniaturization and allow the possibility of more cost effective devices.

Figure 4.5 represents a scheme of the optical setup used for chemical sensing with the plasmonic structures integrated on the microfluidic chip. As it can be seen in Figure 4.5, an

halogen lamp (100W) coupled on an Olympus upright microscope was used as white light source. An Olympus 50x objective lens (NA = 0.25, f = 180mm) was used to focus the light onto the nanohole arrays (both large area arrays or 15 x 15 μm^2arrays fabricated by FIB) inside the microfluidic channels.

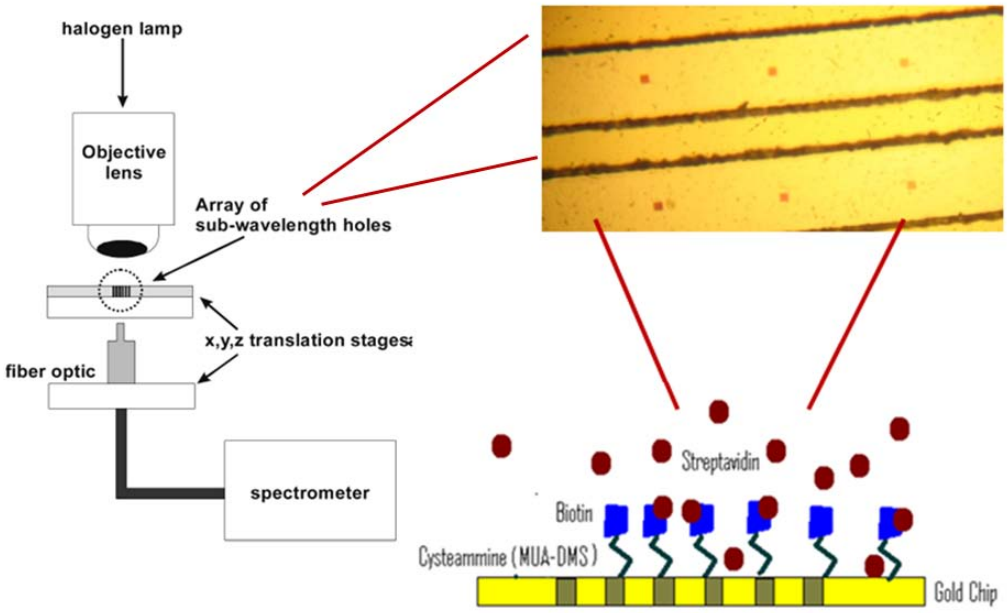

Figure 4.5 Schematic of the transmission setup with enlargements of the nanohole sample and microfluidic channels; the cartoon at the bottom represent an example of binding event at the metal surface inside a specific channel

The transmitted light was then collected through a fibre optic and directed to an Ocean Optics spectrometer (USB 4000). Each recorded spectrum was actually the average of 5 slightly smoothened (BoxCar = 10) individual spectra. The integration time, related to the amount of light collected per spectra, was varied each time. The reason behind it was to maintain a working range close to the detector saturation; the different integration times were taken into account when the spectra were analyzed and compared to each other.

The insets in Figure 4.5shows both a picture of nanohole arrays inside the microfluidic channels, and a schematic of the binding events during a biosensing experiment.

Two different control/blank spectra were also collected in every experiment. The first is referred as "*white light*", being the transmission of the light through a 10 μm^2 gold carved hole. The second control is referred as "*dark*", being the background detector noise in the absence of light.

In order to evaluate the performance of the nanoholes and decrease post-processing time, the spectra collected were analyzed with a script written in Matlab. To summarize, the code operated as following: first, the *dark* background control was subtracted from each spectrum, to regenerate a zero baseline; afterwards, this new spectrum was scaled by its integration time and divided by the *white light* spectra. This was made in order to eliminate the influence on the transmitted spectra of the light source itself. This latter data set was then normalized and plotted with the other spectra obtained at different refractive indexes. The shift in wavelength was automatically observed and recorded at the normalized intensity of 0.9 (90%) for each peak: this position was chosen because it has the highest slope (derivative), and therefore it is the best place to detect small variations.

The wavelength shifts were then plotted against the different refractive indexes (or concentrations of the molecule of interest in binding events) in order to determine the sensitivity of the device, as explained in Section 2.3.

This particular detection method was used to obtain most of the results in this thesis, displayed in Chapter 5, Chapter 6, Chapter7. This approach was considered the best to obtain very comparable results for the many different situation in which it was applied.

Now, in the literature, [86,87] other methods can be found with less data modification, and therefore less error propagation that can be uptake for the analysis.

4.3.2 Intensity Detection with a Charge-Coupled Device (CCD)

Another configuration often used in bioplasmonic research is the monitoring of the changes in the transmitted light intensity (Section 2.2). This setup has shown to have performances quite comparable with the Biacore benchmark[18, 19], and therefore was chosen to be explored in this thesis.

Figure 4.6 is a schematic representation of the setup built in the lab. Briefly, a 633 nm diode laser (Ultra Low Noise, Coherent) beam was first spatially filtered through a 16x objective lens coupled with a 25μm pinhole, followed by an iris. The more homogeneous beam was then collimated and again filtered with another iris before hitting the sample. The light transmitted through the nanoholes was then collected into a CCD (CoolSnap HQ^2, Photometrics).

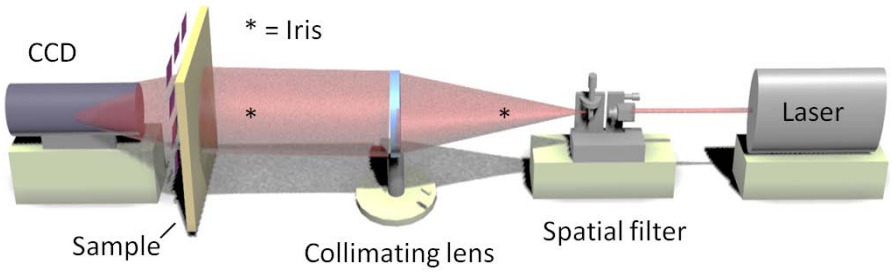

Figure 4.6 Illustrative representation of the optics involved in the setup for intensity interrogation. From the right: laser source, 633nm; spatial filter; iris; collimating lens; iris; sample; focusing lens; CCD detector.

Figure 4.7a shows part of a typical image obtained from the CCD, in black and white, where the bright spots are the individual nanohole arrays. The large field of view of the camera and the size of the sensor chip allowed us to image, in each frame, up to 7 by 7 arrays of nanoholes, 250μm apart. This aspect is extremely important for multiplexing, as it allows the detection of different solution concentrations, or different biomolecules, together with the controls at the same time.

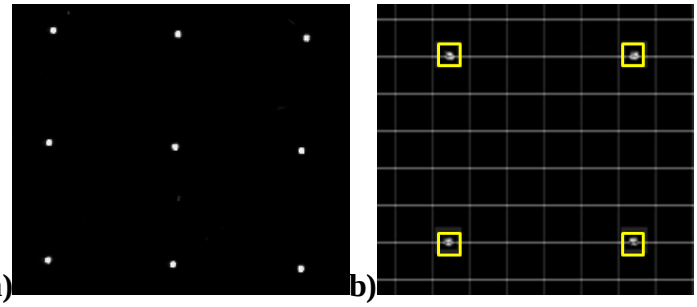

Figure 4.7 a) Example of image (part) collected by the CCD detector; b) representation of the grid and areas used by the program to evaluate the transmitted intensities from the arrays

The ability of the detector to acquire frames at a very high speed rate, as less than 70msec apart, resulted in the collection of a very high number of data. In doing so, it was possible to average the information (intensity variation) resulting from the images. The actual measurements considered, then, were more statistically robust, as well as the fluctuations due to instrumentation noise were decreased. In fact, it is believed that the major source of noise in this detection system is the so-called *shot noise*, from Poisson statistics of the photon flux, which is proportional to the square root of the light intensity.[2] One of the most common ways to limit this noise is to work close to detector saturation, acquire very rapidly a lot of pictures and average them. Because of the amount of data collected, another code written in Wolfram Mathematica was used for the analysis step.

It is helpful to remind that the focus of the measurements is to detect intensity variations in time of the transmitted light from the nanohole arrays. Specifically, an intensity value is associated with each pixel of the images collected, stored as a 16 Bit gray scale. As a consequence, only the pixels carrying the information from the arrays needed to be selected and evaluated.

The program automatically located the positions of the arrays (in pixels) with the help of a grating, and define small “working” areas around them, as shown in Figure 4.7b. Afterwards, the sum of all the intensity values in between these areas were acquired for each frame. After averaging, the obtained values were plotted against time. Results, discussion and comments on these experiments will be found in Chapter 8.

4.4 FDTD Simulation

The finite-difference time-domain (FDTD) method is based on the approximation of finite differences on both the spatial and temporal derivatives present in Maxwell’s equations, the curls, between magnetic and electric field. The FDTD algorithm in a 3D space is based on a special volume, called the Yee’s cells, where the electric and magnetic fields are staggered in both space and time. In Figure 4.8a it is possible to see the representation of the field vectors orientations in the Yee cell. The size is a very important parameter, defined through the dimensions of the mesh during calculations. Finer mesh dimensions yield more precise approximations of the field components. The drawback is that the computing time will increase exponentially as the mesh size decreases; a compromise needs to be found, in particular if the dimensions of the feature are kept 1:1 in the simulation.

As the electric and magnetic fields are related to each other, the algorithm needs to analyze both of them in a step-sequence method. Figure 4.8b schematically represents the situation

for a 2D case. Starting from the two adjacent electric fields, the program estimate the following magnetic field, and so on. The process is repeated until all the fields have been obtained over the desired structure or space considered.

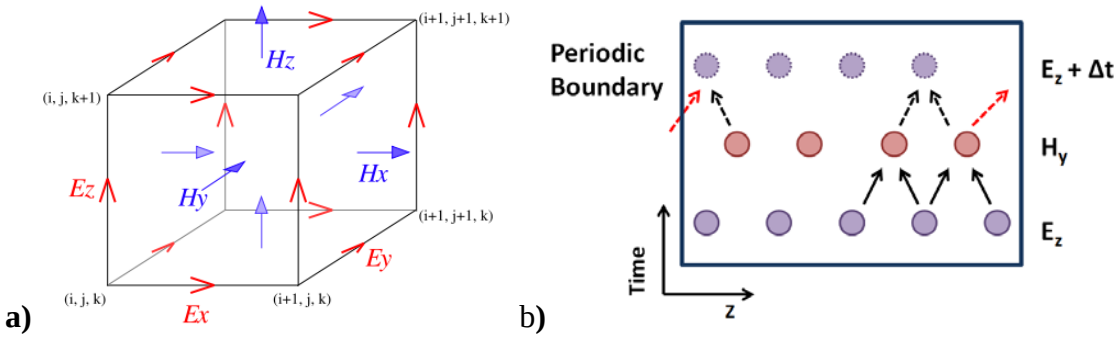

Figure 4.8 a) Schematic representation of the Yee's cell, with the 3D indication of the vectors for the electric and magnetic fields. b) cartoon representing the iterative process occurring in a simulation. The behaviour of periodic boundaries is also shown [a) Reproduced with permission from[88]]

Very important considerations need to be made for when the program reaches the boundaries of the space being simulated. Each FDTD simulating platform might have slightly different boundary definitions. In this study, the software *FDTD Solutions 7.0* by Lumerical was used, which contains three main types of boundary conditions[89]: perfect matching layer (PML), metal, and periodic. In the first situation, the field is completely absorbed by the PML and it is lost outside the computational area. On the contrary, if the boundary is chosen to be a metal, considered as a perfect reflective material, all the energy will bounce back into the simulation volume. For periodic structures, as in our case, the condition chosen for the boundary was "periodic". This means that the field components hitting the boundary in one direction will re-enter is the simulating area at the opposite end. It is like looping everything back inside the simulation volume, as shown by the red arrow in Figure 4.8.

Figure 4.9a and b display the computing space and the structures chosen for the simulations at two different viewpoints. There are many elements present in the structure, each one with specific parameters essential to the good outcome of the calculation. From the bottom to the top, the parameters are:

- *Glass substrate support*: light blue; refractive index (RI) of 1.5; thickness equal to 500μm (although not as thick as the real substrate, ~1mm, it is large enough for the purpose of the simulations).
- *Thin chromium layer*: black line; RI defined by Palik[90]; thickness equal to 2 nm.
- *Gold layer*: yellow; RI as defined by Christy and Johnson[91]; thickness equal to 100 nm.
- *Nanohole*: brown contour on the top face and greenish colour in Figure 4.9b; variable opening sizes; shape and RIs depending on the specific calculation run; thickness of 100 nm.
- *Dielectric above the surface*: black; variable RIs depending on the calculation; thickness of 500 μm, which is well beyond the SP decaying field.

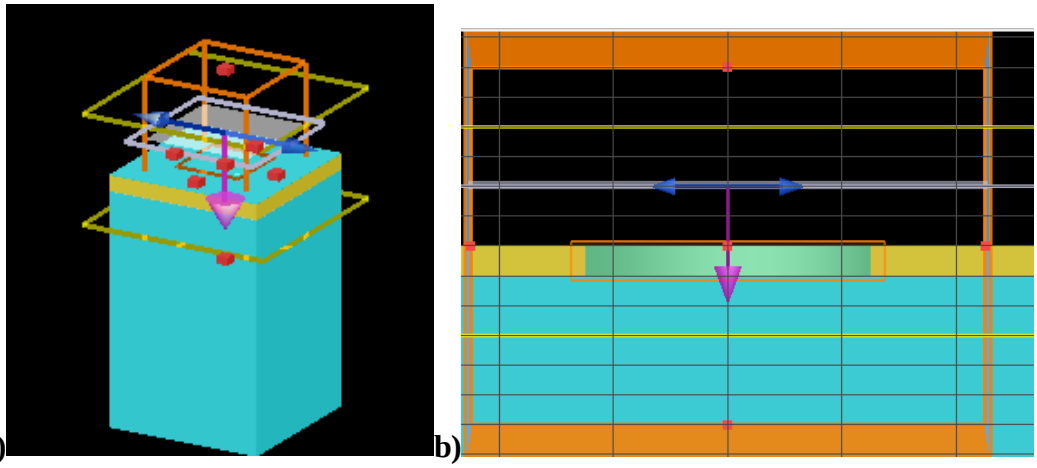

Figure 4.9 a) 3D image of the structure build for the simulations. All the elements required for the calculations are visible and described in the text. b) xy plane enlarged image of a nanohole at the center of the computational space (orange frame).

The light source was chosen to be a plane wave, represented by the blue double-arrow in Figure 4.9b. The orientation of the double arrow coincides with the polarization direction . The direction of propagation is indicated in Figure 4.9b by the pink arrow.

The two light yellow screens in Figure 4.9b are the reflection detector, above the surface, and the transmission detector, underneath the structure, respectively. Although only the transmission data will be analyzed, it was important to have the reflection data to validate the effectiveness of the calculation. The orange cube in Figure 4.9a defines the simulation space, in this case taken symmetric to the structure for simplicity.

The transmitted frequencies obtained from the simulations were converted into wavelengths and the consequent spectra were analyzed and compared to the experimental data (Section 4.3.1).

The simulations were run with the help of Dr. Aftab Ahmed and Dr. Hao Jiang, Post-Doc fellows in Prof. Reuven Gordon's lab (Dept. Electrical Engineering).

4.5 Surface Chemistry

Surface chemistry is probably the most important step in the development of a biosensor, as it constitute the recognition element for the molecules being detected.[92] If the modification of the surface is not done properly, the whole system fails. In particular for this thesis, two particular surfaces events were studied: biotin and streptavidin recognition and the capture of Leukemia cancer markers. Both systems will be described more in details in the next sections.

4.5.1 Biotin and Streptavidin

Biotin and streptavidin (SA) are two very well-known biomolecules in the biosensing field because of their strong affinity. The dissociation constant is so low, ($K_D = 10^{-14}$M) that their bond is considered to be the strongest among the non-covalent interaction, and it can resist to fairly harsh conditions of pH, temperature, and solvents.[55] For being so robust and fairly simple to handle, the biotin-SA binding pair if often used in proof-of-concept of the plasmonic platforms.[6, 71] The gold surface was functionalized with biotin, and the modified sensor surface was exposed to different concentrations of SA. The spectral shifts, described in Section2.3,were related to the SA-biotin binding. The reason behind this choice is that, as it is possible to see from Figure 4.10a, biotin is a relative small molecule in comparison to SA.[55] The spectral shift given by the latter binding onto the former would be more significant than vice versa.

The first step in modifying a surface is the placement of a linker that can covalently anchor the molecules to the metal surface. The covalent bond between the metal surface and the monolayer is crucial for the stability and the surface density of the biomolecular

receptors. This can be achieved with the use of thiol-terminated organic molecules, which are able to organize themselves in a self-assembled monolayer (SAM) by hydrophobic interactions.

Due to its known non-fouling properties (necessary to avoid the physisorption of unwanted molecules, known as non-specific binding), poly-ethylene glycol (PEG) was chosen as a suitable linker.[93]

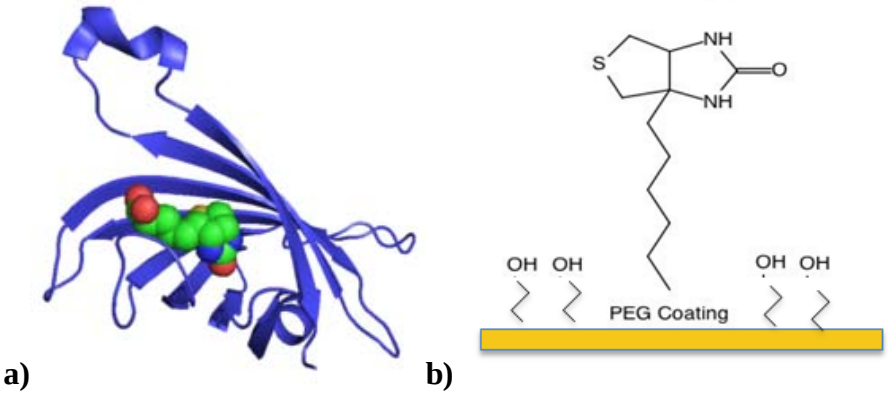

a) **b)**

Figure 4.10a) 3D ribbon representation of the streptavidin structure with a sphere representation of the much smaller biotin in the binding site. b) Schematic diagram of the modified surface after formation of a PEG monolayer cross-linked with biotin [a) reproduced with permission from[94]]

In order to obtain more reproducible and reliable results, an one-step chemistry was pursued. Thiol-polyethyleneglycol-biotin conjugated is available commercially, and it can be easily used to produce the surface modification represented in Figure 4.10b.Specifically, the gold slides were first cleaned with ethanol and acetone in a sonicator for 10minutes. The slides were rinsed with the same solvents and nitrogen dried; the cleaning step was repeated one more time. Rapidly, the samples were drop coated with 1mM ethanoic solution of HS-PEG-Biotin (654KDa, Nanoscience) for 3hours, at room temperature. After the elapsed

time, the slide was rinse first with ethanol, and then with a phosphate saline buffer, PBS, (Sigma, diluted ten times) before being nitrogen dried.

The spectra of the biotin-coated surface were then recorded, and compared with the ones acquired after the binding of the SA solution (Streptavidin from Streptomyces Avidinii, Sigma).

4.5.2 Surface Modification for Leukemia Detection

As described above, the molecules biotin and streptavidin constitute a specific and strong recognition pair. However, for almost any other protein present in blood or express on a cell membrane, the best recognition element is a specific antibody, which can only target that particular protein with fairly strong affinity. Nowadays, there are complementary antibodies available for the most common cancer markers studied in research (PSA for prostatic cancer; EGFR for lung cancer; etc.), operating either as therapeutic molecules or just as recognition elements.[95]

a) 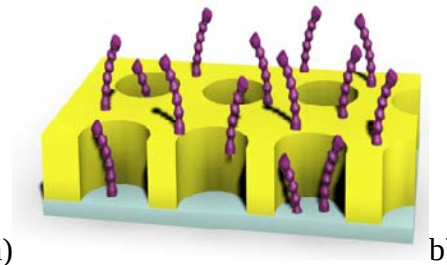 b) 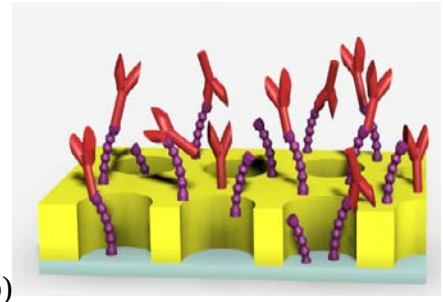

c) 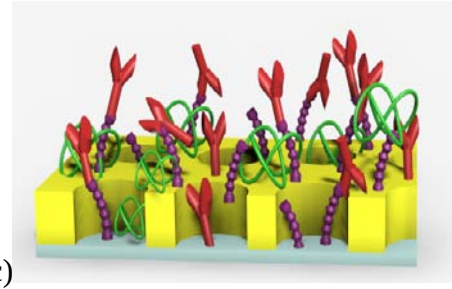 d) 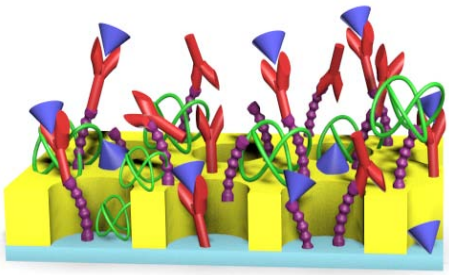

Figure 4.113D cartoons explaining the steps involved in the surface functionalization with antibodies. a) formation of a SAM layer that can be covalently modified with the antibodies as in b). c) represents the surface after being coated with BSA, to avoid non-specific binding, and d) is a representation of the antigens capture by the modified surface

As described in the introduction Section 2.4.1, the target molecules for the detection of leukemia are the kappa and lambda chains of human antibodies. This can be a little confusing, as both the target (antigen) and the detection molecule are classified as antibodies. To avoid any further confusion, the human antibodies present in the patients sample to test will be called antigens. On the other hand, the probing molecules on the surface ready to capture and detected the antigens will be called antibodies. These antibodies have a fairly general specificity; in fact, they need to detect any conformation of the human kappa or lambda chains, and not, as in most of the cases, just a specific molecule. They can then be obtained from other species (not human), such as rabbit, mouse or goat, to meet these parameters.

Figure 4.11 represent a cartoon of one of the most used method to functionalize a metal surface with antibodies.[2, 3] As in Figure 4.11a, the first step is the formation of a monolayer (purple), covalently linked to the metal through a sulphydryl (thiol) group. This linker molecule is carboxyl-terminated, in order to allow further modification with a protein. The schematics of the following step are represented in Figure 4.12. Through the use of the

activating compound 1-Ethyl-3-(3-dimethylaminopropyl)carbodiimide (EDC), N-Hydroxysuccinimide (NHS) can react with the hydroxyl group of the carboxylic acid to form an ester bond. NHS is a good leaving group that can be displaced by any primary amine.

In a protein, this primary amine group can be found in three different amino acids (histidin, arginin and lysin) and at one end of the protein chain. Now, as shown in Figure 4.11b, the protein of interest, in this case the antibody (in red), is covalently linked to the monolayer and therefore to the metal surface.

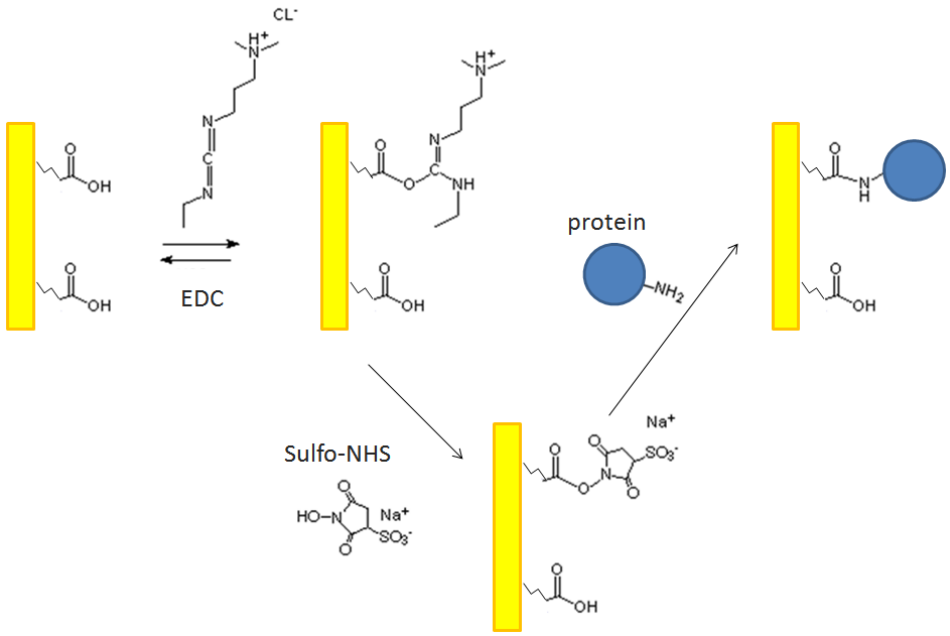

Figure 4.12 Schematic representation of the EDC-NHS chemistry for covalent attachment of proteins to an existent SAM

The following step is a non-specific exposure of the surface to bovine serum albumin (BSA), represented in green in Figure 4.11c. This protein will serve for two purposes: first, to de-activate any unreacted NHS; second, due to its non-fouling properties, to create a

better surface against non-specific binding.[2] Figure 4.11d displays a final representation when the antigens are introduced and possibly bind to the functionalized surface.

However, looking back to Figure 4.11b, there is a major drawback in this scheme: the binding of the proteins to the surface is completely conformational unspecific. This results in no control on the orientation of the probing antibodies or molecule at the surface, introducing a fairly large sample to sample variability .

After realizing this issue, another more robust and reproducible method was implemented. It is known that a specific protein, called Protein A, has strong affinity for the constant region (Fc) of antibodies;[96] this particular region, shown in Figure 4.13a, is at the opposite side of the lambda and kappa chains. This means that if the protein A binds an antibody, the regions we would like to target will be always exposed.

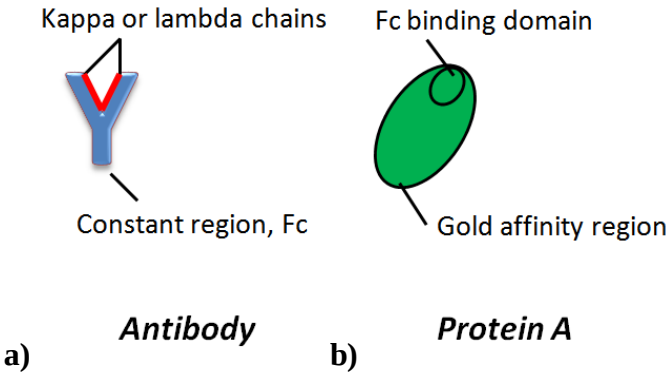

Figure 4.13 Schematic representation of a) antibody structure and b) protein A structure

In addition to this great advantage, protein A has a fairly strong affinity for gold surfaces. As it can be seen from the cartoon in Figure 4.13b, protein A binds to the metal surface with a region that does not contain the antibody recognition sites. These information were transformed into a simpler gold functionalization methodology. The protocol followed to

obtain the modified surface, represented in Figure 4.14, is outline hereafter.[96] Most important to be noted, the probing antibodies had a more controlled orientation, allowing better surface reproducibility and homogeneity.

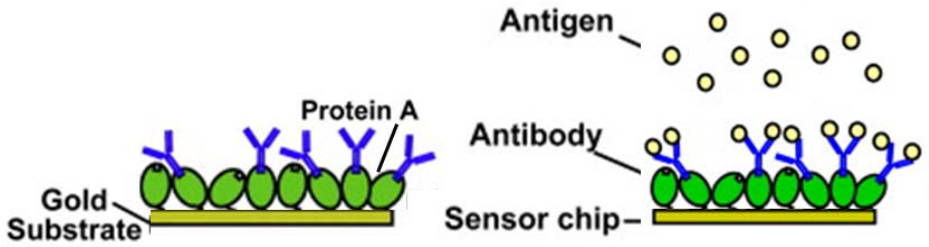

Figure 4.14 Cartoon representing the surface modification with protein A [Modified with permission from [96]]

The gold slides were first cleaned with ethanol and acetone in a sonicator for 10minutes. The slides were rinsed with the same solvents and then nitrogen dried; the cleaning step was repeated one more time. Rapidly, the samples were drop coated with 1mg/mL solution of Protein A (from Staphylococcus Aureus, Sigma) overnight, stored at $+4^{o}$ C.

After the elapsed time, the slides were rinse gently with PBS before being nitrogen dried. A 100 μg/mL solution of goat anti-human kappa chain or goat anti-human lambda chain (Abnova Taiwan Corporation) was left on the surface to absorb for 2 hours, at room temperature. Again, the slides were rinse gently with PBS before being nitrogen dried.

The spectra of the antibody-coated surface were then recorded, and compared with the ones acquired after the absorption of the human kappa or lambda antigens, from human blood samples of Leukemia patients. The patient samples were kindly provided by Dr. Cheng Wang, hematopathologist at the Mt. Sinai Hospital, Toronto, ON. Each serum sample was diluted in order to have an average concentration of antibody of ~ 100μg/mL.

Chapter 5: Results on the Geometrical Influence on the Performance of Nanohole Arrays Fabricate by FIB

In this chapter, in particular, it will be presented a study on how the geometrical characteristic of the FIB-fabricated nanohole arrays (size, shape and periodicity) can influence their sensing performance. The purpose was to define the parameters that would lead to the most sensitive platform. At first, an overview of the parameters chosen for this study will be presented. Then, a brief introduction of the finite-difference time-domain (FDTD) simulation and theoretical background will be mentioned. At last, the results obtained, for both bulk and surface sensitivities, will be presented and compared with the numerical simulations. The results will be regrouped and presented for different hole shapes, with a final comparison at the end.

All the experimental spectra in this section were obtained in transmission mode and wavelength interrogation, as described in Section 4.3.1.

5.1 Geometrical Parameters

Figure 5.1summarizes all the different parameters explored in this study. As it is possible to see, two different shapes, circular and rectangular, were chosen for the subwavelength holes. The circular holes are the most commonly used in biosensing, and there are considered as the benchmark[16, 32, 48]. The rectangular shape was chosen in order to evaluate the effect of sharp edges, having some localized surface plasmons, on the sensor performance. In addition, polarization-dependence studies were performed for the rectangular structures. Square structures were also tested at first, but as they didn't show any improvement in respect of circular holes, the attention was focused on rectangular structures only. The

distance center-to-center between holes(periodicity)ranged from 400nm to 650nm, with increasing 50 nm steps. The diameter of the circular holes were100nm, 150nm, 200nm, 250nm.For the rectangular holes, the dimension of one edge of the structure was kept constant at 250 nm, while the size in the other dimension was varied. The values were chosen to be 50nm, 100nm, 150nm and 200nm, leading to aspect ratios of 5, 2.5, 1.67, 1.25, respectively.

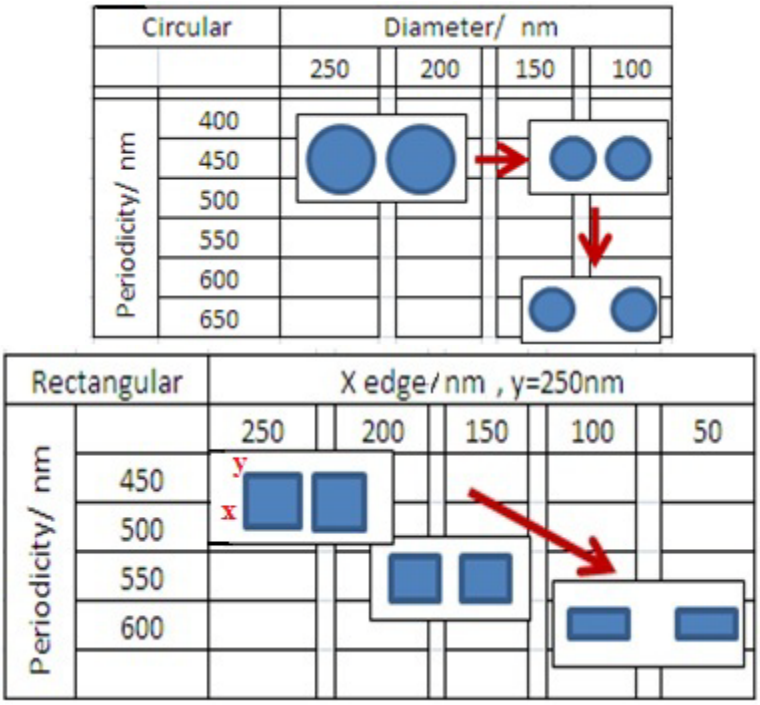

Figure 5.1 Overview of all the different combinations of geometrical parameters for shapes employed in this study

Before looking at the sensing capabilities, it was interesting to see how these two geometrical parameters (size and periodicity) had an effect on the white light transmitted spectra in air. Figure 5.2apresents the white light transmitted spectra at one specific periodicity, 400nm, as the size of the feature was varied. It is possible to see that the amount

of light transmitted is proportional to the size of the hole. This doesn't mean that the largest hole diameter is the most sensitive, but it presents the larger signal-to-noise ratio for the transmitted spectrum.

Figure 5.2b, on the other hand, represents the comparison between the transmitted spectra of all the periodicities for one circular array with constant 200 nm diameter . Is it possible to see that the plasmonic resonance peak shifted towards longer wavelength when the periodicity is increased, in agreement to Eq. 2.4in Section2.1.

In addition, new plasmonic orders appeared at shorter wavelength, as the periodicity is increased (Figure 5.2b). It is very important to mention that for the purpose of this work, the (1,0) transmission order, indicated in Figure 5.2b, was the only one monitored.

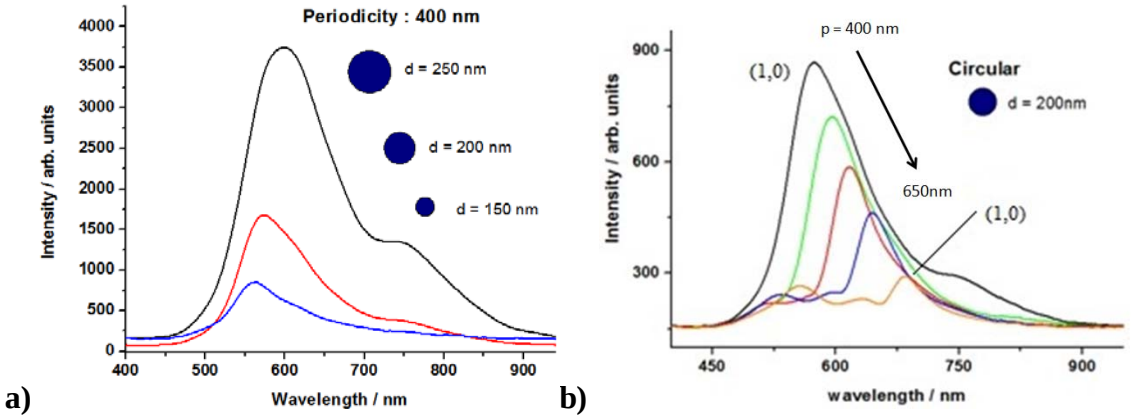

Figure 5.2a) Comparison of transmitted spectra for circular arrays with the same periodicity but different hole diameters, as indicated. b) Comparison of transmitted spectra for circular arrays with the same hole diameter (200 nm)but different periodicities.

All the combinations of size, periodicity, and polarization were evaluated for rectangular holes, totalling 72 structures. Both bulk and surface sensitivity were measured for all of them, as described below.

5.2 Circular Holes

As mentioned before, the purpose of this study was to find how the several geometrical parameters have an effect on the performance of the arrays as biosensors. At first, the evaluation was made through the comparison of the values of bulk sensitivities, obtained from each structure. The experiments were run by simply varying the concentration of ethanol-water solutions (different refractive indexes) and recording the spectral changes of the light transmitted through the nanohole arrays.

Figure 5.3 summarize the bulk sensitivity results for circular nanoholes arrays.

For the bar graphs in Figure 5.3, the two horizontal axes are the different periodicities of the arrays and the diameters of the holes. The heights of the columns are the bulk sensitivities given on the vertical axis.

The experimental values for the sensitivities were obtained by averaging all the data collected from several tests run, either on the same sample or on different samples. As the sample-to-sample variability was fairly high (and it will be discussed later), the sensitivities were first normalized and compared within each data set. This procedure kept the overall trend intact within a dataset, allowing a better estimate of the overall experimentally-obtained performance.

It is noticeable in Figure 5.3 that the highest sensitivities are found for the 500nm periodicity and for 250nm, 200 nm and 150nm hole diameters (maximum sensitivity was for 500 nm periodicity and 200 nm diameter sample). Fairly high sensitivities were also observed for the 250nm diameter samples, particular to the ones with at 400nm periodicity. The overall trend in Figure 5.3 seems to imply that the sensor performance in terms of bulk sensitivity deteriorates as the periodicities of the arrays increased.

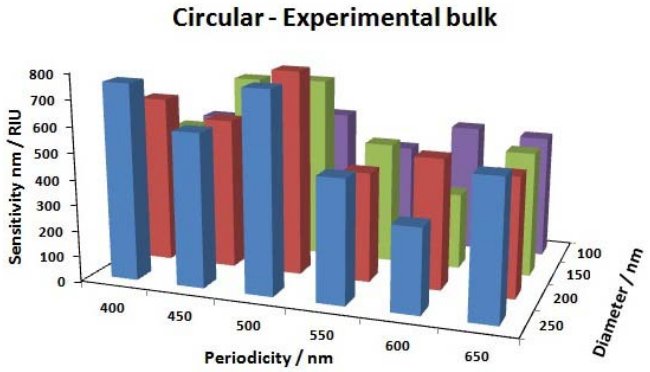

Figure 5.3 Bar graph representing the values of bulk sensitivity obtained experimentally for circular arrays.

Figure 5.4 presents the simulated results (discussed in Section 4.4) for geometric parameters that coincide with the circular arrays discussed in Figure 5.3. It is very interesting to notice that the simulated performance results were a good match to the results obtained experimentally. A little surprising was the fact that the bulk sensitivities achieved experimentally were a little higher than the simulated. In fact, for the 200nm diameter-500nm periodicity array, it was found a an experimental bulk sensitivity of 792 nm/RIU, but only of 520 nm/RIU through the calculations.

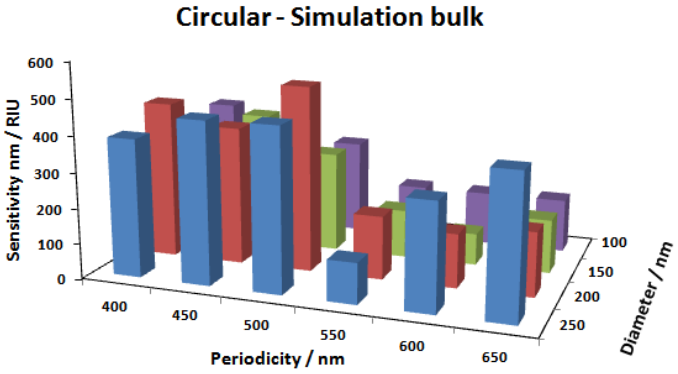

Figure 5.4 Bar graph representing the values of bulk sensitivity obtained computationally for circular arrays.

The plausible reason to explain this situation is that some conditions used during the simulation were not exactly reproduced, as part of the analysis described in Section 4.3.1. The computational test might not quantitatively replicate the experiments in the lab, but they do match qualitatively.

The surface sensitivity was also analysed, in order to determine if the trend observe for bulk sensing (Figure 5.3) was maintained.

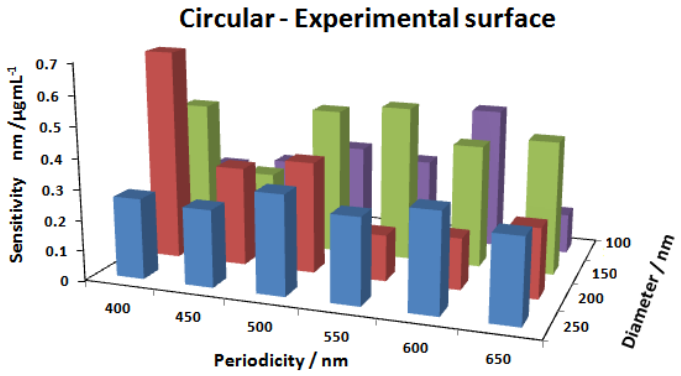

Figure 5.5 Bar graph representing the values of surface sensitivity obtained experimentally for circular arrays.

The gold surface was functionalized with biotin, and exposed to different solution of SA, as described in Section 4.4.1. Figure 5.5 illustrate the findings obtained experimentally. As it is possible to observed in Figure 5.5, the best surface sensitivity (0.73 nm/µgmL^{-1}) was observed for the 200 nm hole diameter and 400nm periodicity.

Figure 5.6 indicates that the trend in surface sensitivity is not confirmed by the simulated results, as observed for the bulk sensitivities (Figure 5.3 and Figure 5.4). Although the trends in surface sensitivity are different for the experimental and the numerical data, the simulations showed that the array with the best surface sensitivity is the same as it was

found for bulk sensitivities (Figure 5.4). The possible discrepancy between the experimental S_c and the simulated data can be explained by the fact that the actual spectral shifts recorded in order to obtain the S_c are much smaller than the ones in bulk sensitivity experiments.

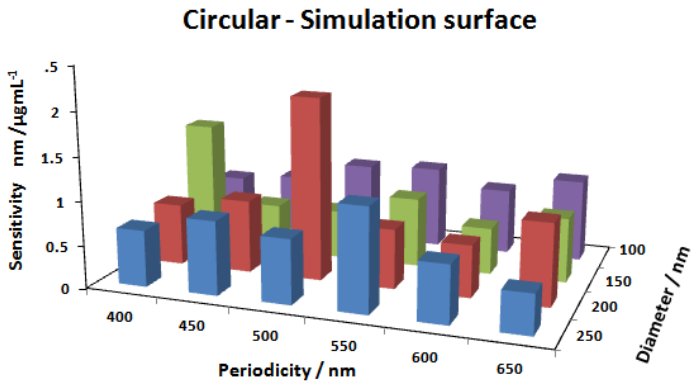

Figure 5.6 Bar graph representing the values of surface sensitivity obtained computationally for circular arrays. The trend confirms the bulk sensing behaviour, both experimental and calculated

These shifts are, in some cases, close to the error in determining the wavelength (0.2 nm), causing an extra variability in determining the peak position. Furthermore, the experimental data were collected from samples (gold films) that contained several arrays of nanoholes (24 in total). This means that the sample had to be moved on the microscope stage after the addition of each solution to take the spectra. Although extreme precaution and attention was given to re-position each array in the same spot as the previous data acquisition, this procedure adds a source of error. For bulk sensing experiments, this aspect was negligible because slight spectral variations could be overcome by the large changes in wavelength measured. In the surface sensitivity case, however, the small difference in positions might have introduced a fairly large relative error.

5.3 Rectangular Arrays

As mentioned before, rectangular shape holes were also fabricated in order to test the effect of the light polarization on the performance of the sensors. It is known in the literature that sharper features focus the electric field around the apex/corners, with a consequent increase in the sensitivity[22]. However, for anisotropic structures, the magnitude of the field enhancement would be different for different polarizations..Figure 5.7a schematically represent the two orientations of the light polarization relative to a rectangular hole. In that schematic, the transverse electric polarization (TE) is defined as perpendicular to the long edge of the nanohole, fixed at 250nm in length. The transverse magnetic polarization (TM), on the other hand, would be the perpendicular to the short edge. It is important to remind that the width of the slits tested was as narrow as 50nm. In this situation, the electric field could couple with the field on the other side of the structure, possibly enhancing even more the sensing capabilities.[97] Figure 5.7b shows the transmission spectra, in water, of one of the rectangular nanohole array, periodicity of 450nm and aspect ratio of 5 (250nm/50nm).

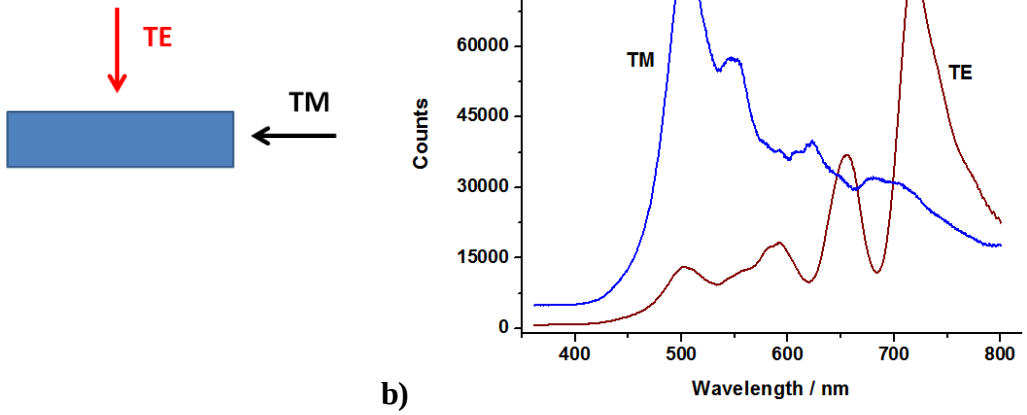

a) **b)**

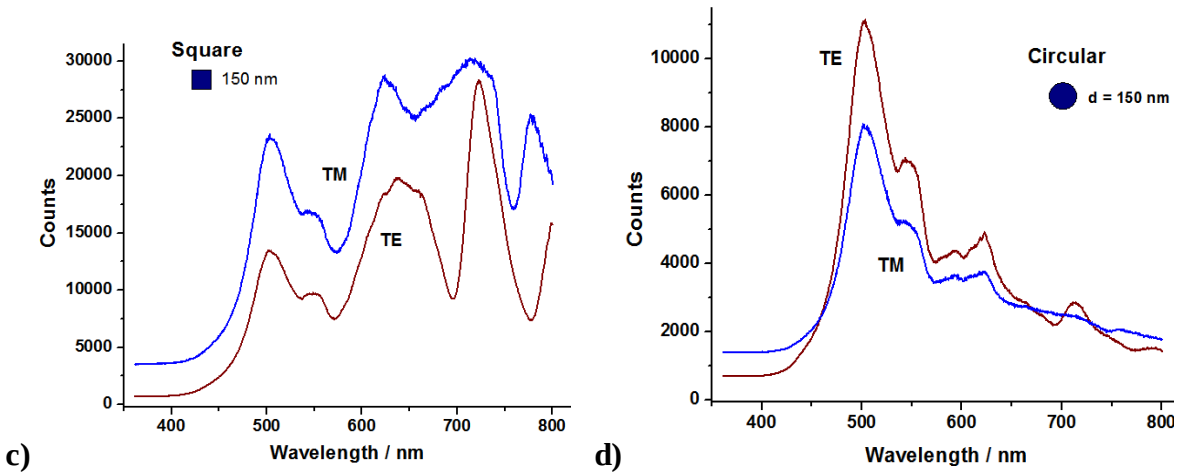

Figure 5.7a) Polarization of the light in respect of the rectangular nanohole. Comparison between the TM and TE polarization for a) rectangular nanohole arrays, 50nm by 250nm and periodicity of 450 nm; b) rectangular nanohole arrays, 200nm by 250nm and 450 nm periodicity; d) circular holes, 150nm in diameter, periodicity of 450 nm.

Clearly, there is a large difference in the plasmonic resonances detected by both polarizations. To carefully ensure that the spectra did not contain artifacts, the same type of polarization measurements were done for both a circular and a wider rectangular nanohole array, depicted in Figure 5.7c and d. According to Figure 5.7d, the circular structure (diameter 150 nm, periodicity 450nm) present very minimal variations due to the different polarization, as expected. Further, the box-square array in Figure 5.7c (150 nm in size, periodicity 450 nm), does present some discrepancies between the TM and TE polarization, although being more symmetrical, the effect is not as visible as in Figure 5.7b.

It is important to note at this point that the TM spectra were enlarged 8 folds to be easily comparable with the TE spectra, for all the graph in Figure 5.7. This difference can be attributed to many factors; in particular, the reflection from the optics involved in the system

and the spectrometer grating in the detector can favourite the efficiency of transmission of one polarization in respect to the other. The possible influence of this low transmission intensity in the evaluation of the results will be discussed more in detail later in this session. Another important considerations in Figure 5.7b, is that the TM transmission spectra is very similar to the one observed for the circular hole array (Figure 5.7d). The large peak experienced with the TE polarization at longer wavelength in Figure 5.7b agrees well with previous work in the literature[98]. Resonances at longer wavelength (700nm to the near infra-red) are normally more sensitive to bulk refractive indexes changes, due their the higher plasmonic penetration length and fewer losses[99].

It is then expected that the TM polarization would lead to a sensor performance comparable to the one encountered for circular holes. Furthermore, the TE polarization should show enhanced sensitivity for structures with high aspect ratio (narrow rectangular apertures) at larger periodicities.

5.3.1 TM Polarization Studies

Figure 5.8 represents the experimental results for bulk sensitivities obtained for all the arrays of rectangular holes under TM polarized light. As predicted, the better performance parameters were found to be very consistent with the ones determined for the circular hole case (Figure 5.3). In particular, it can be concluded that the best performing array for bulk sensing have a periodicity of 450nm and holes with an aspect ratio of 1.25 (250nm by 200nm) . The fact that the values of sensitivities for the narrowest rectangular apertures (50nm by 250nm) were fairly below average can be connected with the less intense transmitted light in those cases. The causes could be either the less amount of light detected

deriving from the optics as discussed earlier, or the less transmitted light by the small size of the structure itself. The consequence is a lower signal-to-noise ratio, introducing variability in the determination of the spectra. In some cases, it was impossible to evaluate a value for bulk sensitivities. In average, all arrays of narrow rectangular holes tested with TM polarization were found to be the least consistent with each other for different experiments. Figure 5.9 presents the results for bulk sensitivities of arrays of rectangular holes that were calculated computationally. The trend of the simulations agree with the experimental results, but experimentally, the highest sensitivity found was lower than the one obtained for circular arrays, with a S_b of 527.6 nm/RIU.

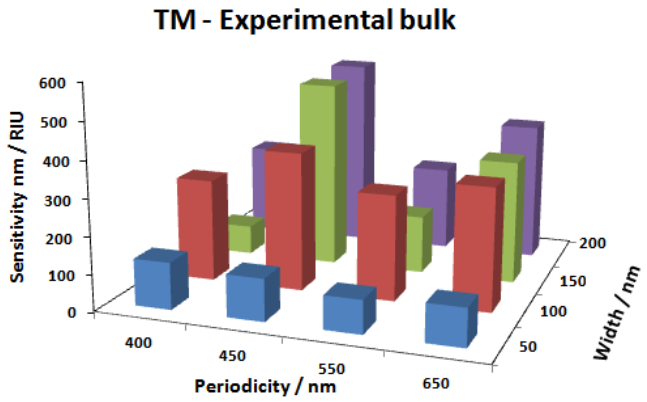

Figure 5.8 Bar graph representing the values of bulk sensitivity obtained experimentally for rectangular arrays under TM polarized light. The trend matches what found for circular arrays, as expected.

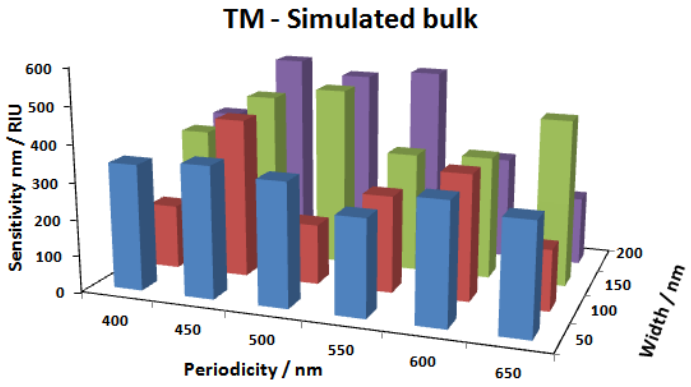

Figure 5.9 Bar graph representing the values of bulk sensitivity obtained computationally for rectangular arrays under TM polarized light. The trend confirms what found experimentally.

The experimental surface sensitivities were measured and their values are summarized in Figure 5.11. It was interesting to notice from Figure 5.8 that the best surface sensitivity was found for the same geometrical combination than for bulk sensing. The rectangular array with aspect ratio of 1.25 and periodicity of 450nm had the largest surface sensitivity at $0.65 nm/\mu g m L^{-1}$.

The simulated surface sensitivities are summarized in Figure 5.11. These results display that the best performing array had a periodicity of 400nm and aspect ratio of 1.67 (250nm/150nm). Although not perfectly matching the experimental results, still the trend of having large aspect ratio structures with low periodicity is respected and confirmed. Further, this trend reflects again the behaviour noticed for circular holes.

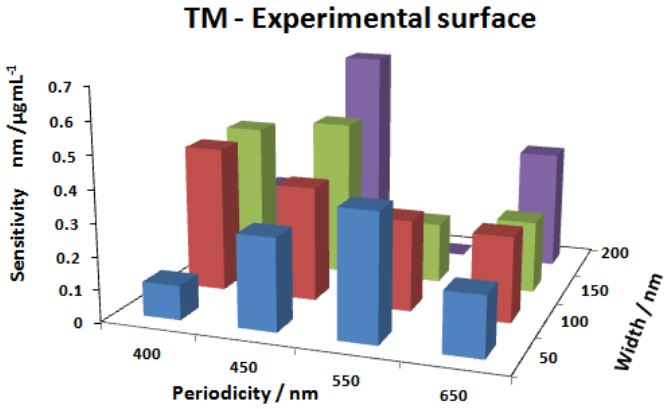

Figure 5.10 Bar graph representing the values of surface sensitivity obtained computationally for rectangular arrays under TM polarized light. The trend reflects what found for the bulk sensing.

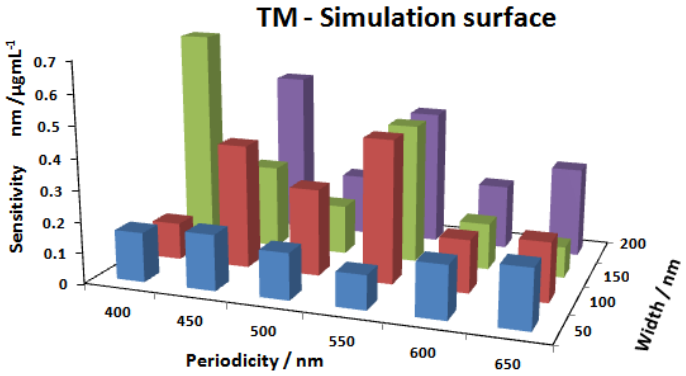

Figure 5.11 Bar graph representing the values of surface sensitivity obtained computationally for rectangular arrays under TM polarized light.

5.3.2 TE Polarization Studies

Figure 5.12 shows the measured bulk sensitivities under TE polarized light. Figure 5.13, for comparison, represents the calculated performance by FDTD. Although in the latter the trend is more consistent and uniform, the arrays performance determined experimentally match nicely the simulation data.

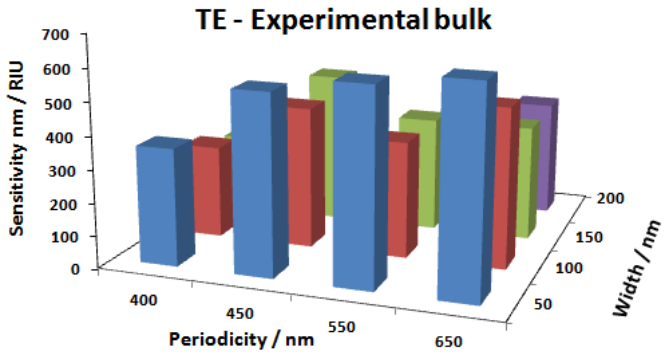

Figure 5.12 Bar graph representing the values of bulk sensitivity obtained experimentally for rectangular arrays under TE polarized light.

It can be determined from Figure 5.12 that the combination of highest aspect ratio rectangular hole (250 nm by 50 nm) with the highest periodicity (650 nm) led to the best bulk sensitivity. In terms of absolute values, a bulk sensitivity of 628.44 nm/RIU was determined experimentally while the simulations yielded 631.93 nm/RIU for that array.

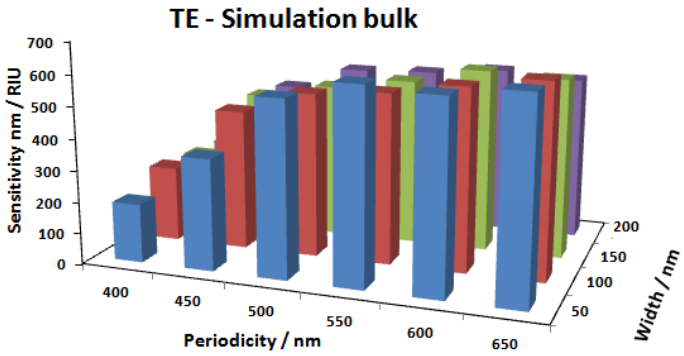

Figure 5.13 Bar graph representing the values of bulk sensitivity obtained computationally for rectangular arrays under TE polarized light. The trend confirms what found experimentally.

Different trends were found for the experiments that determined the surface sensitivities through the detection of SA onto the biotinylated surface (described in Section 4.4.1). As it

can be seen in Figure 5.14, the experimental trend replicates the behaviour found for bulk sensitivities. The combination narrower rectangular hole (higher aspect ratio) and larger periodicity presented the best performance in terms of surface sensitivity. The experimental data did not exactly match the trend found for the FDTD simulations, shown in Figure 5.15.

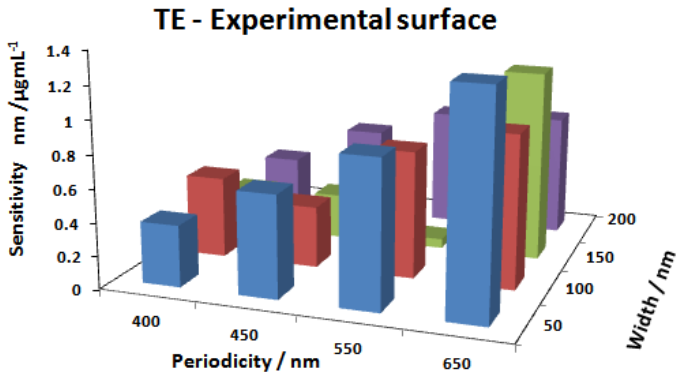

Figure 5.14 Bar graph representing the values of surface sensitivity obtained experimentally for rectangular arrays under TE polarized light. The trend reflects the results obtained for bulk sensing.

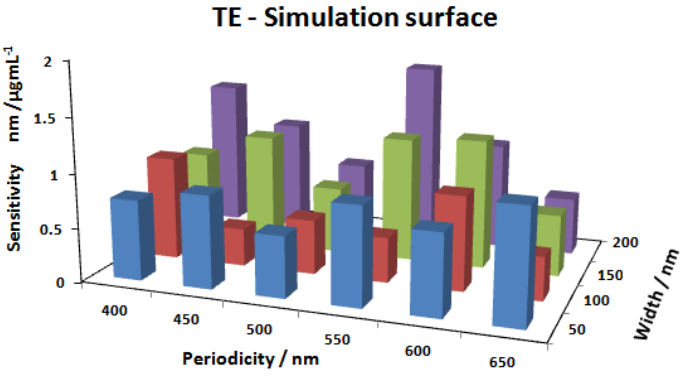

Figure 5.15 Bar graph representing the values of surface sensitivity obtained computationally for rectangular arrays under TE polarized light. The trend deviates from the results obtained experimentally.

A possible explanation for the mismatch could be found in the mash size used for the simulations. Unfortunately, these particular simulations were run with a larger mesh size

(3nm) that is not the ideal to detect surface binding events. Simulations with 1nm mesh size will be performed to support the experimental data.

5.3.3 In-sample and Sample-to-Sample Variation

During the analysis of the experiments, some variability between in-sample measurements and sample-to-sample were found.

The in-sample variation can be due mainly to the re-usage of the surface. Although the cleaning steps were performed thoroughly, it is almost impossible to return the sample to its original conditions.

The sample-to-sample variability, on the other hand, should originates mainly from the fabrication of the structures themselves. The gold film could present different roughness even before the milling of the holes. Further, some variation could have been introduced during the FIB fabrication.

In both cases, another sources of variation could be the experimental conditions, reagent used (fresh or stored solution) and the fact that the sample was moved on the microscope stage for the recording of the spectra themselves.

Table 5.1a and b resume, respectively, the in-sample variation and the sample-to-sample variation encountered for rectangular (TE polarization) for bulk sensing.

As it is possible to see, the in-sample variability is lower in average, with a main value of 19.3% (Table 5.1a). On the other hand, the sample-to-sample variation was found in average to be 30.3%.

This range of value was consistent for all the other analysis performed in this chapter for bulk sensing.

Surface sensing, also for the reasons already introduced earlier in section 5.2, presented a slightly higher average of variation, with 25% for in-sample and 40.1% for sample-to-sample.

In order to roughly estimate the possible error in the analysis caused by the variability just mentioned, an example of the 2D surface plot for rectangular holes (TE) was re-plotted. In the new graph in Figure 5.18 the average surface sensitivity values presented earlier in Figure 5.14 were summed to the respective values of the sample-to-sample variation associated with them.

Table 5.1 Example of the in-sample and sample-to-sample variation found in the analysis performed. The values refer to experiment conducts with rectangular holes, under TE polarization

a) **IN -Sample**

%	Periodicity /nm			
Width /nm	**400**	**450**	**550**	**650**
50	28.3	23.9	26.8	11.5
100	13.5	25.8	18.9	10.7
150	15.1	25.0	29.2	12.0
200	8.6	26.3	18.3	8.3

b) **Sample-to Sample**

%	Periodicity /nm			
Width /nm	**400**	**450**	**550**	**650**
50	48.8	16.2	16.7	9.1
100	45.6	39.2	44.7	35.7
150	32.6	26.6	16.7	34.1
200	43.2	27.1	32.9	15.3

Although there is some visible variation between the two graph, it is not pronounced enough to modify the trend discovered earlier for best performing geometrical parameters.

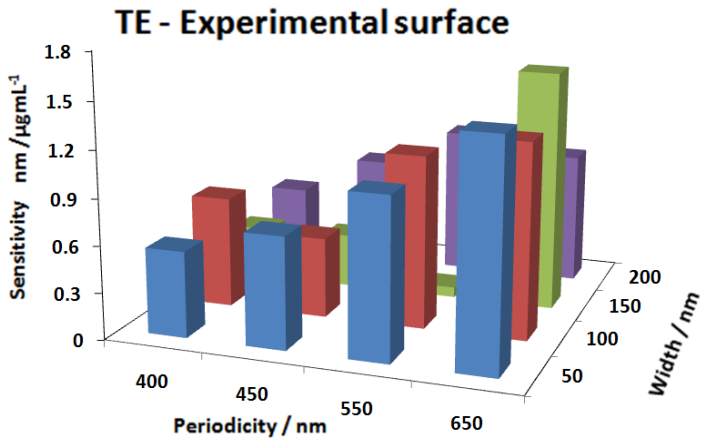

Figure 5.16 Bar plot calculated by adding the sample-to-sample variability in Table 5.1b to the results of surface sensitivity obtained for rectangular array, under TE polarization.

5.4 Final Remarks

Table 5.1summarizes the best sensitivities obtained from the different nanohole arrays investigated in this chapter. Clearly, the arrays of rectangular holes, probed under TE polarization, showed improvements relative to the TM polarization. Further, when the circular arrays are taken as standard, the narrow rectangular holes presented the highest surface sensitivity, almost a two folds increase relative to the other structures. However, the bulk sensitivity was found smaller, in contradiction with the larger enhancement expected. Possibly, the extra coupling of the field happening between both sides of the rectangular structure is responsible for the better surface performance; however this effect is not as strong when averaged over the whole decaying sensing field (~200nm) in bulk sensitivity tests. The fact that longer periodicity were favourite in respect of short spacing could be a reflection of the better penetration length and less losses[99] at higher wavelength, resolving in better performances.

Table 5.2 Summary of the best performance parameters obtained for the different nanoholes arrays

	Circular	*Geometry*	***Rect. TE***	*Geometry*	***Rect. TM***	*Geometry*
Bulk Sensitivity S_b, nm / RIU	792	d = 250 nm	628.5	a.ratio: 5	527.6	a.ratio: 1.25
		p = 400nm		p = 650nm		p = 450nm
Surface Sensitivity S_c, nm/μgmL^{-1}	0.73	d= 250 nm	1.33	a.ratio: 5	0.65	a.ratio: 1.25
		p = 400nm		p = 650nm		p = 450nm

Chapter 6: Plasmonic Sensing using Large Area Nanohole Arrays Fabricated by UV Nanolithography

In this particular section, large area nanohole arrays fabricated by UV nanolithography will be evaluated as possible plasmonic biosensors. These flexible and cheap platforms are suitable for mass production, possibly narrowing the gap between the lab and the commercial market.

The performance of these substrates as chemical sensors was first evaluated from bulk sensitivity measurements. Then, the surface sensitivity was determined, through the detection of SA absorption onto a biotinylated surface. At last, and most importantly, the detection of antigens from leukemia patient blood samples will be demonstrated using this platform.

All the spectra were acquired in transmission and wavelength interrogation mode, as described in Section 4.3.1.

6.1 Bulk Sensitivity

Different solution of deionazed (DI) water and ethanol were made in order to achieve 4 different refractive indexes:1.3332, 1.3359, 1.3382 and 1.3459. The RI values were determined with a PAL-RI Pocket Refractometer (Atago), comparable with literature values. An equal amount of each solution (500 μL) was placed on top of the surface, and then covered with a thin cover glass for a uniform distribution of the liquid. After the measurements, the solution was washed away with pure DI water and the samples were nitrogen dried. The sample was always kept untouched on the microscope stage throughout

the whole experiment, to be the best comparable possible between each measurements. For each refractive index, the spectra were acquired at least at two different locations on the same grating geometry(Figure 4.3b). The final sensitivities were then calculated for all the different spots, in order to evaluate the uniformity of the platform. In addition, different samples were tested. Samples 1 2 were didn't present a chromium layer between the gold and the plastic substrate. Sample 3, however, was deposited in this lab, allowing the addition of a 5nm chromium layer (Section 4.1.3) to improve the adhesion of the gold to the plastic. The performance of Sample 3 is displayed in Figure 6.1, where multiple columns represent the bulk sensitivity values obtained in the two different regions of the grating.

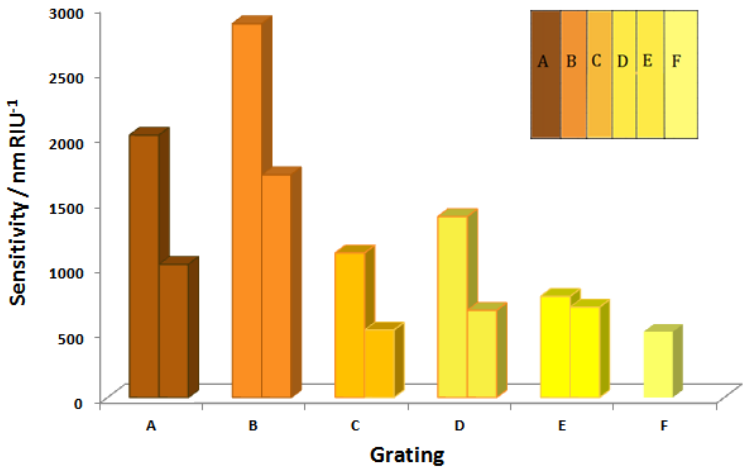

Figure 6.1 Graph summarizing the bulk sensitivities obtained from two different spots on each grating structure. Inset: schematic reminder of the sample with the six different structures

The bulk sensitivity values from Figure 6.1and the ones from the other two samples are summarized in Table 6.1a and b. Figure 6.1and Table 6.1 indicate a relative large spatial and sample-to-sample variations. The deviation on the same sample can be explained by defects in the fabrication process, and this was confirmed by the SEM micrographs shown in Figure

6.2. The images taken from different regions on the structures presented uneven features depending on the location.

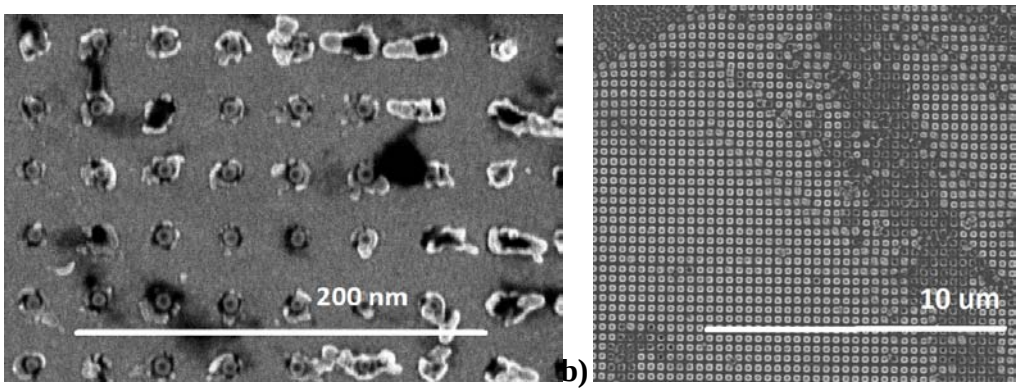

Figure 6.2 SEM micrograph showing a) the uneven features due to the fabrication process and b) the damage present on the samples.

On the other hand, the main reason behind the sample-to-sample variations is the damage present on the structures, as in Figure 6.2b. Samples 1 and 2 didn't have the chromium layer between the gold and the acetate substrate to improve adhesion, which had a direct consequence in the performance (bulk sensitivities are given in Table 6.1). Possibly due to improper handling during shipping or the lack of proper storage after fabrication, the gold layer might have come off, affecting the optical properties of the structures. On the other hand, this consideration can be used as a proof that indeed the better adhesion of the gold due to the chromium layer improved the stability of the gratings. This was translated, as outlined in Table 6.2, in a greater performance of Sample 3, almost three folds in some regions tested. In particular, the grating referred as "B" showed an outstanding sensitivity of 2870.5 nm/RIU, much higher than the one obtained with nanohole arrays made by FIB (Section 5.4.3).

Further, the output noise was found to be 0.45 nm, by averaging 10 different spectra without fitting. As a consequence, the resolution of the platform was found to be 3 10^{-4} RIU.

Some of these achievements were obtained with the help of Talon Jones, a summer student in Prof. Brolo's lab.

Table 6.1 Summary of the performance obtained from Sample 1 and Sample 2, both without the chromium layer. The geometrical parameters of the structures are outlined in Table 6.2

Sample 1	**Sensitivity/nm RIU^{-1}**	
Grating	*Spot 1*	*Spot 2*
A	179.23	160.3
B	175.98	99.648
C	246.59	184.54
D	267.24	235.79
E	50.6	-
F	39.129	-

Sample 2	**Sensitivity/nm RIU^{-1}**	
Grating	*Spot 1*	*Spot 2*
A	545.91	315.39
B	441.6	131.22
C	378.95	318.95
D	689.29	534.02
E	446.98	428.75
F	444.97	285.99

Table 6.2 Summary of the performance of Sample 3, taken for all the structures in two different points. In the fourth column, it is shown an estimate of respective resolutions. The geometrical parameters of the structures are outlined in the last two columns.

Sample 3	**Sensitivity/nm g mL^{-1}**		**Resolution / RIU**	**Size**	**Period.**
Grating	*Spot 1*	*Spot 2*	*Noise, σ = 0.45 nm*	/ nm	/nm
A	2015.5	1022.6	2.36 10^{-4}	300	400
B	2870.3	1710	1.65 10^{-4}	200	330
C	1109.8	517.7	4.28 10^{-4}	100	240
D	1389.8	669.2	3.42 10^{-4}	150	400
E	776.8	693.4	0.61 10^{-3}	100	320
F	504.15	1022.6	0.94 10^{-3}	nd	nd

6.2 Biotin-SA

As a proof-of-concept for surface biosensing, the large area nanohole array samples were tested for the detection of streptavidin binding onto a biotinylated surface. The preparation of the modified gold surface with biotin was as described in the experimental Section4.4.1.Four different solution concentrations of SA were used: 1.25µg/mL, 2.5µg/mL, 5 µg/mL and 10 µg/mL.

All spectra were collected in air, starting with the dried biotin-modified surface. Each solution of SA was then placed on the surface for 20 minutes. The sample was washed with PBS and gently nitrogen-dried before the next measurements. Again, the sample was never touched or moved throughout all the experiments.

The surface sensitivity obtained from Sample 3 is plotted in Figure 6.3, and summarized in Table 6.3. Unfortunately, due to the lack of gold adhesion, it was not possible to perform this type of experiments on the samples without the chromium layer (Samples 1 and 2).

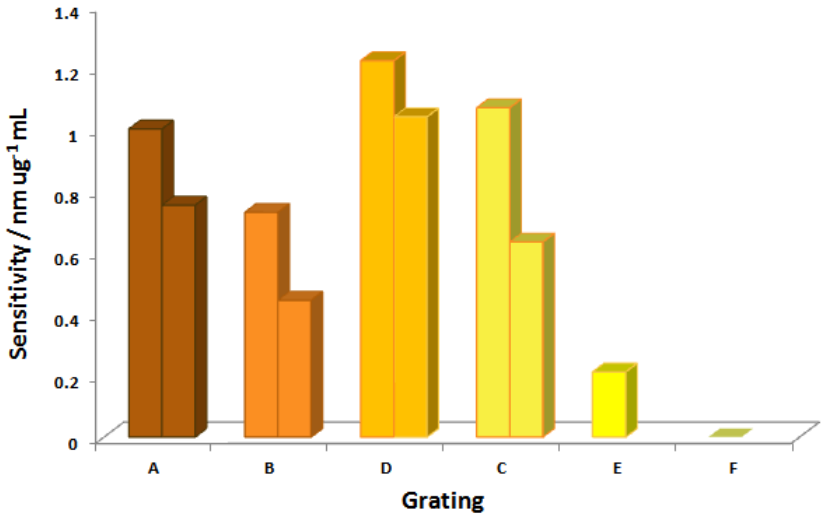

Figure 6.3 Graph summarizing the surface sensitivities obtained from two different spots on each grating structure

Figure 6.3 confirms that the best performances in terms of surface sensing are from the structures A to D, in agreement with the results for bulk sensitivity presented in Figure 6.1 and Table 6.1. As mentioned earlier, it was possible to determine by the SEM micrographs that the E and F structures (Figure 6.2a depicts the structure E), being the one with the smallest features, are also the most uneven or damaged. This is the main reason behind their poor performance. Also, it can be noticed that the surface sensitivities are more uniform than the bulk sensitivities. The D structure, with 1.3 nm / μgmL^{-1},presented the best performance, but this value was not too different than observed for the other geometries (gratings A – C). The variability within each structure, however, is still reason of concern for precise quantification.

Table 6.3 Summary of the performance in surface sensing of Sample 3, obtained for all the structures at different points

Sample 3	**Sensitivity / nm μg·mL^{-1}**	
Grating	*Spot 1*	*Spot 2*
A	1.0008	0.7533
B	0.7298	0.4444
C	1.2226	1.04
D	1.0696	0.6336
E	0.2113	-
F	-	-

The values of the surface sensitivities themselves, ranging from 0.8 nm/ μgmL^{-1} to 1.3 nm/ μgmL^{-1} are very comparable with the ones obtained for the nanohole arrays fabricated by FIB and discussed in Section 5.4.3.

Unfortunately, the large improvement in the performance of these grating for bulk sensing was not translated for the surface sensing performance. In the future, it is advisable to re-test the platform, with new samples, for the surface sensitivity.

6.3 Leukemia Cancer Marker Detection

After proving the ability of this sensor to detect surface binding events, it was decided to test the platform for the detection of leukemia cancer markers.

The surface was functionalized as described in the experimental Section 4.4.2. In these specific measurements, the surface was modified with goat anti-human lambda chain antibodies. Consequently, the human serum samples containing over-expressed lambda chain were used for the binding experiments, while the sera with excess of kappa antigens were used as negative controls.

All the spectra were collected in air, starting from the dried protein A-modified surface. The solution of anti-human antibody was incubated for 2 hours on the surface sample. The solutions containing either the over-express lambda antigens or the over-expressed kappa antigens were left to react for 1 hour. After each step, the samples were washed with PBS and gently nitrogen dried before the measurements. The sample was never removed from the microscope stage during an experiment.

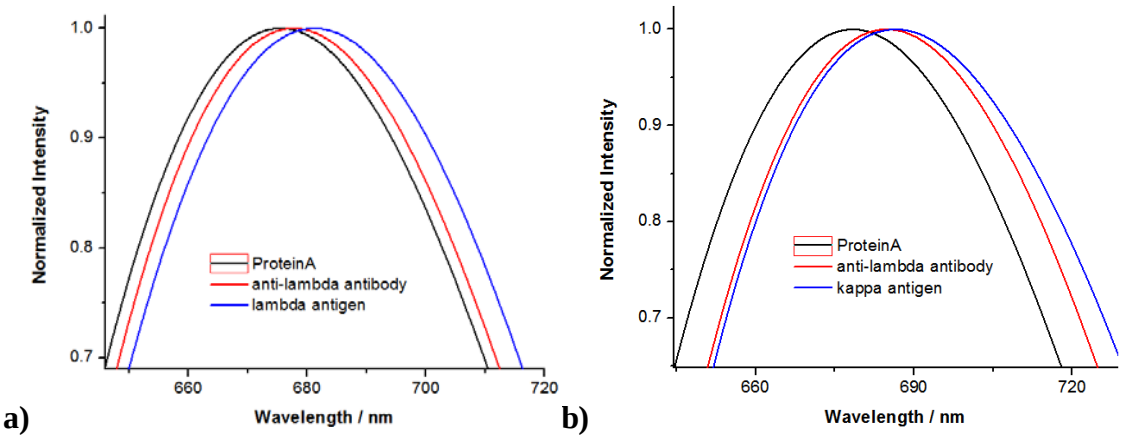

Figure 6.4 a) Plot representing the spectral shift recorded after the functionalization of the surface (red curve) and the binding of the antigens (blue curve). b) Spectral shift obtained after the functionalization of the surface (red curve) and the non-specific binding from the absorption of the wrong antigen (blue curve).

Figure 6.4a and b shows the different spectra obtained from two different spots of the same grating(grating A to be specific). The sample was cut in half and the experiment was carried on simultaneously and identically on both pieces. The black curves are the spectra obtained from the surface functionalized with protein A. The red spectra were obtained after the anti-lambda antibodies modification. Figure 6.4a then, shows the spectral shifts obtained after the binding of lambda antigens. On the other hand, a much smaller shift due to the interaction of the surface with the negative control (kappa antigens) is noticed in Figure 6.4b . In the case of the negative control, no shift at all is expected. However, some non-specific binding events will always occur, as both the serum solution is rich in other proteins that can also adhere on the surface, and the antibody affinity and specificity is never 100%. This explains the small shifts seen in Figure 6.4a.

The graphs in Figure 6.5 summarized all the wavelength shifts obtained from the different gratings, both for the actual lambda antigens detection (Figure 6.5a) and their respective

comparison with the control experiments with the kappa proteins (Figure 6.5 b). As earlier, spectra were recorded from more than one location on the samples. As an example, the results for experiments realized in a different position in sample A is presented in Figure 6.5as“a2”.

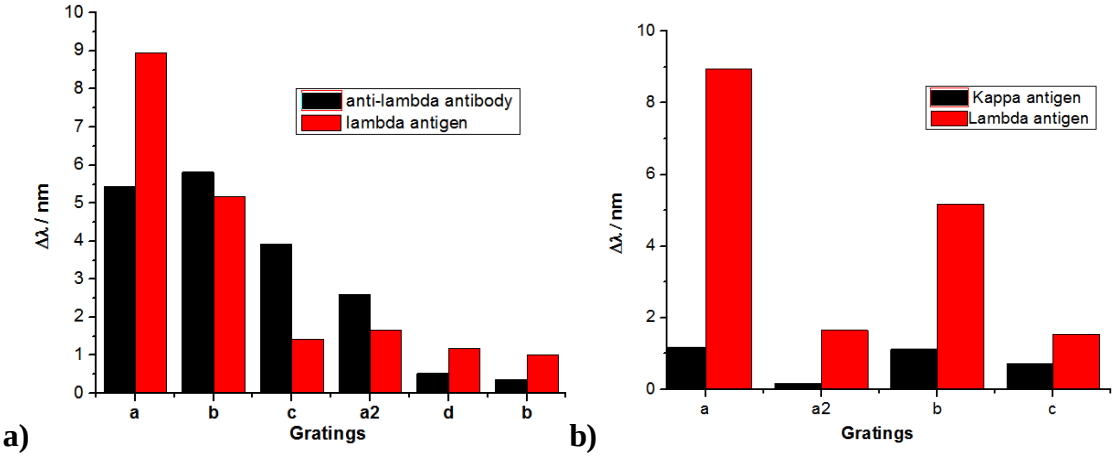

a) **b)**

Figure 6.5 a) Summary of the spectral shift obtained on each grating by the surface functionalization with anti-lambda antibodies (black bars) and the absorption of the lambda antigen (red bars). b) Direct comparison of the spectral shift obtained for the Lambda absorption (red bar, as in a)) and the control experiments due to Kappa antigens binding non-specifically (black bars)

The shift generated by the detection of the right antigens was significantly larger than the control changes. The results clearly prove that the detection of a specific cancer marker was obtained, and that this platform can be indeed employed for biosensing.

To prove even further that the surface and the platforms are specifically selective, another test was conducted using the sera samples. After recording the negative control shifts (from kappa antigens), the sample was left untouched and one grating (B) was exposed to the presence of the lambda over-expressed solution. The rationale was that if the

shift recorded was due only to non-specific binding, then the surface should still be very receptive for the right antigen. In another words, the specificity of the anti-lambda antibodies should have been preserved and they should capture their counterpart, generating a greater plasmonic shift.

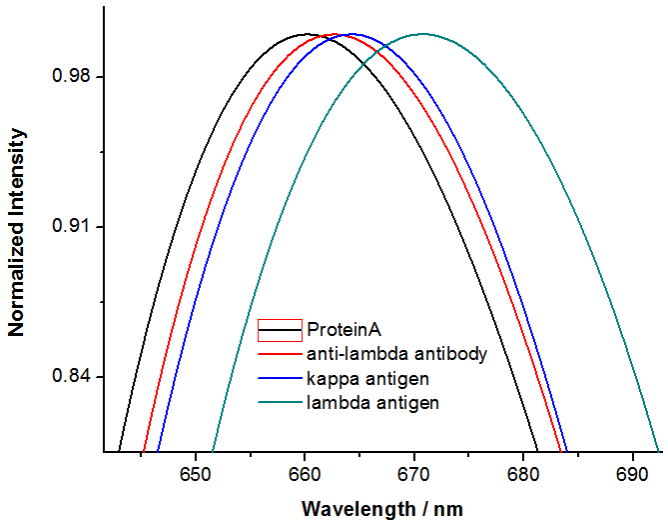

Figure 6.6 Representation of the spectral shift obtained from the binding of the lambda antigens (green curve) after the non-specific binding of the wrong molecules (kappa antigens, blue curve), used as negative control.

The results for that experiment is shown in Figure 6.6.It can be seen that the spectral change due to the functionalization of the surface (red curve) and the shift from the non-specific binding of the kappa antigens (blue curve) are found to be relatively small, as expected. Finally, Figure 6.6shows a much larger shift (green curve) due to the specific binding of the lambda molecules.

Overall, this plastic platform demonstrates large capabilities as biosensors and they might find a real use in medical diagnosis. The structures A, B and D showed the best sensing

performance (both for bulk and surface sensitivities). In this case, however, it is hard to attribute the differences in the performance to geometrical parameters, because of fabrication defects (E and F in particular).

Moreover, these three performing gratings have similar periodicity (B : 330nm, A and D: 400nm), but different size features (A : 300nm, B : 200nm and D: 150nm); a direct correlation might be hard to find.

With the advantages of being cheap, flexible and amenable to mass production, these large area sensing platforms constitute a good candidate for integration in lab-on-a-chip type of devices.

Chapter 7: Plasmonic Sensing using Large Area Nanohole Arrays Fabricated by IL

In this particular section, large area nanoholes made by IL will be the platforms evaluated as possible plamonic biosensors.These substrates can present a lot of advantages. First of all, there is the possibility of large volume fabrication, as the samples are reproducible and homogeneous; moreover, due to the large sensing area, they are ideal for multiplexing detection.

As in the previous chapters, the bulk sensitivities were determined first. Then, the surface sensitivities were evaluated using the SA binding onto a biotinylated surface. Finally, the detection of antigens from a Leukemia patient blood sample will also be demonstrated.

All the spectra were acquired in transmission and wavelength interrogation mode, as described in Section 4.3.1.

7.1 Bulk Sensitivities

Different solution of DI water and ethanol were made in order to achieve 9 different refractive indexes from 1.3329 to 1.3427 (Table inset in Figure 7.1). The RI values were determined with a PAL-RI Pocket Refractometer (Atago).

An equal amount of each solution (100 μL) was placed on top of the gold surface, and then covered with a thin cover glass for an uniform distribution of the liquid. For each refractive index, 10 measurements were acquired, and the average of those spectra was used to determine the sensitivity. Each solution was washed away with pure DI water and the

sample was nitrogen dried. The sample was always kept untouched in the same position throughout the whole experiment, to be absolutely comparable between each measurements. In Figure 7.1presents the plot of the averaged spectra for different refractive indexes. The shifts were evaluated at 0.9 (90%) of the normalized intensity, as it was considered the steepest part of the curve. As summarized in Table 7.1, at the end of this chapter, the bulk sensitivity was found to be 1026.38 nm/RIU. The noise in wavelength detection was found to be, on average around0.18 nm, leading to a sensing resolution of 1.75 10^{-4} RIU.

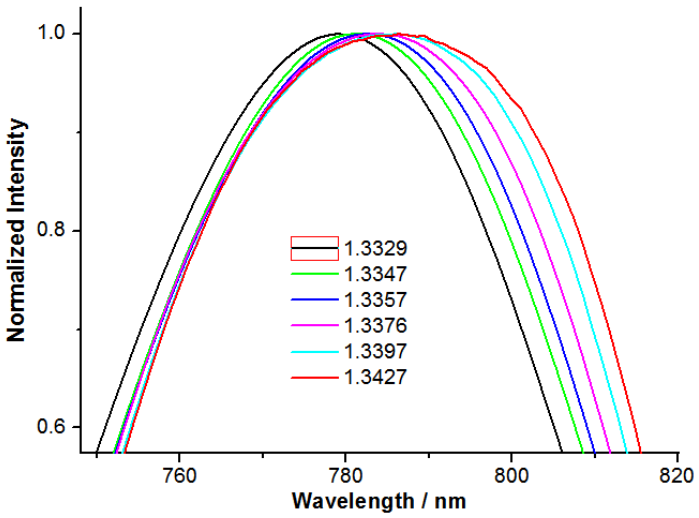

Refractive Indexes
1.3329
1.3347
1.3357
1.3365
1.3376
1.3388
1.3397
1.3409
1.3416
1.3427

Figure 7.1Spectral shifts due to the different refractive index used, listed in the table on the right. Note: some data are not included for better clarity.

7.2 Surface Sensitivity

As in the previous two chapters of this thesis, for the evaluation of the surface sensitivity, a proof-of-concept system was used. The large area nanoholes array was tested for the detection of streptavidin binding onto a biotinylated surface, prepared as described in the

experimental Section 4.4.1. Three different concentrations of SA were used: 2.5 µg/mL, 5µg/mL and 10 µg/mL. The spectra were collected in air, starting with the dried biotin-modified surface. Each solution of SA was then placed in contact with the surface for 20 minutes. The sample was washed with PBS and gently nitrogen dried before the measurements were taken. Again, the sample was never touched or moved throughout the experiment.

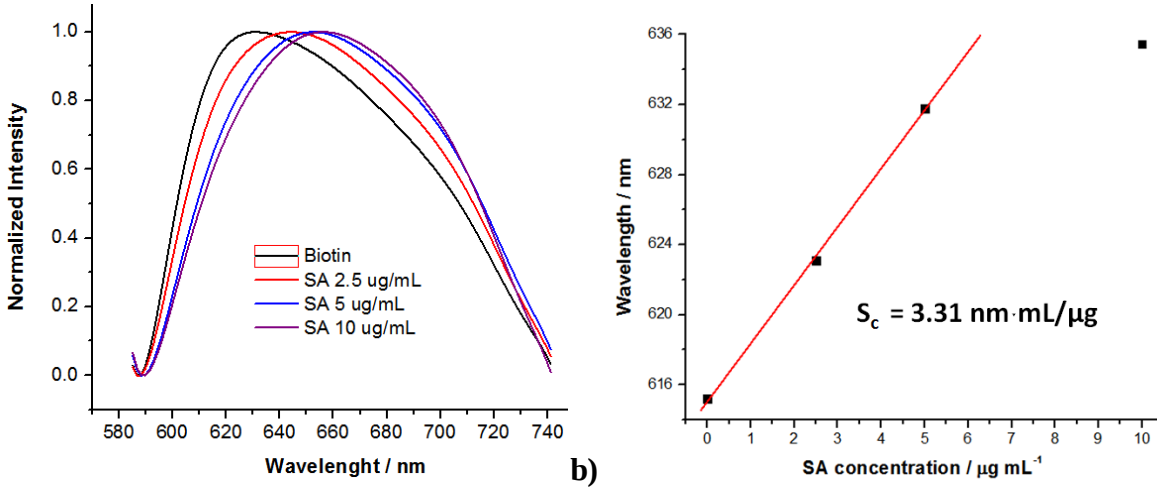

Figure 7.2 a) Spectral shifts detected after the binding of streptavidin onto the biotinylated surface at different concentrations. b) Calibration curve derived from the plot in a. The surface starts to saturate after a concentration of 5 ug/mL.

The transmitted spectra, as well as the calibration curve obtained, are represented in Figure 7.2a and b, respectively. As before, each spectra or point plotted is the average of 10 different measurements. In Figure 7.2b, it is possible to observe that the relationship between the concentration of SA and the spectral shift is not linear in the whole range, which can be attributed to surface saturation at higher SA concentrations. The combination of fairly large concentrations (µM range) with a strong binding affinity (K_D: 10^{-14} M in

solution) and a long reaction time (20 minutes) have allowed the SA to reach equilibrium with the biotin molecules present at the surface.

With the curve obtained, it was possible to evaluate the surface equilibrium constant, K_D. As illustrated in Figure 7.3, the data were fitted with a 1:1stochiometric ratio Langmuir model, following the equation[100]

$$\theta = \frac{\theta_{Max} \cdot C}{K_D + C} \qquad \textbf{Eq. 7.1}$$

Where θ are the free sites, θ_{Max} are the bonded sites at equilibrium and C is the concentration of the analyte, SA in this case. With this model, it was found a $K_D = 1.7\ 10^{-7}$ M.

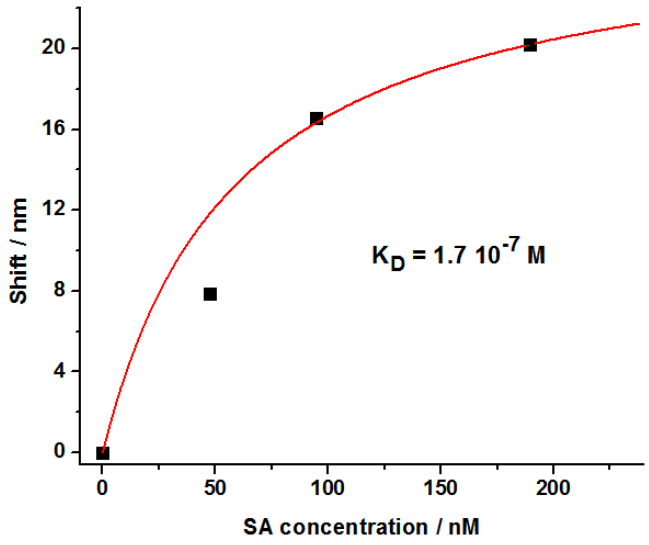

Figure 7.3 Langmuir fit of the data obtained for the binding of SA onto a biotinylated surface. A concentration of 1.7 µM of SA occupies 50% of the biotin sites at the surface.

This K_D value can be interpreted as the concentration of analyte (SA) required to occupy 50% of the surface binding sites (biotin).[100] This value is obviously different form the one

reported in literature of 10^{-14} M[55], implying a that a much lower concentration of SA should completely saturate all the biotin molecules present.

The great difference originates from the fact that one value was determined in solution, while the other one was obtained through a surface experiment. In fact, our results agree with previous surface binding evaluations of the SA – biotin pair that reported a K_D= 2.43 10^{-8} M.[101] There several explanations for the large mismatch .The most important fact would be steric accessibility and the possibility of wrong orientations for some molecules anchored on a rigid substrate. Protein denaturation may also occur during the surface modification. Moreover, stereo-conformation and repulsion due to the high proximity of the binding sites might limit, or influence, the absorption of the analytes.

The surface sensitivity extracted from the linear component of the curve in Figure 7.2b,at lower concentrations, was found to be 3.31 nm/μgmL^{-1}.This value is much higher than the obtained for the nanohole array fabricated by FIB or from the arrays fabricated by UV Nanoimprinting. The variations between each measurements were found to be, on average,0.154nm, leading to a LOD of 46.5 ngmL^{-1}, or 6.02 nM. All these values are summarized in Table 7.1.

7.3 Detection of Leukemia Cancer Markers

After proving the ability of this sensor to detect surface binding events, the platform was tested with leukemia blood samples, for leukemia diagnostic, as described in Section 4.4.2.

The surface was functionalized as described in the experimental Section 4.4.2. In this specific measurements, the goat anti-human lambda chain was chosen as the antibody

immobilized at the surface. As a consequence, the human serum sample containing over-expressed lambda chain was used for the binding experiments.

The spectra were collected in air, starting with the dried protein A modified surface. The solution of anti-human antibody was left to react for 2 hours on the sample to functionalize the surface. The solution containing the over-express lambda antigens was left to react for 1 hour. After each step, the sample was washed with PBS and gently nitrogen dried before the measurements were taken. The samples were never touched or moved throughout the experiment.

The recorded transmitted spectra are presented in Figure 7.4. As before, each spectra or point plotted is the average of 10 measurements.

It was detected a 10nm shift for the lambda antigens present in solution at a concentration of ~100μg/mL. An error variation of 0.21nm between each single measurements was estimated, which can be considered a very small value for this type of experiment.

This experiment proved the ability of the sensor and the setup to detect specific molecules in a rich medium, and that it could be integrated and employed in cancer diagnosis. However, to determine the real effectiveness of the platform, further experiments and controls need to be performed.

First of all, the counterpart of what just tested should be studied: the surface should be modified with anti-kappa, and the binding of kappa antigens should be monitored.

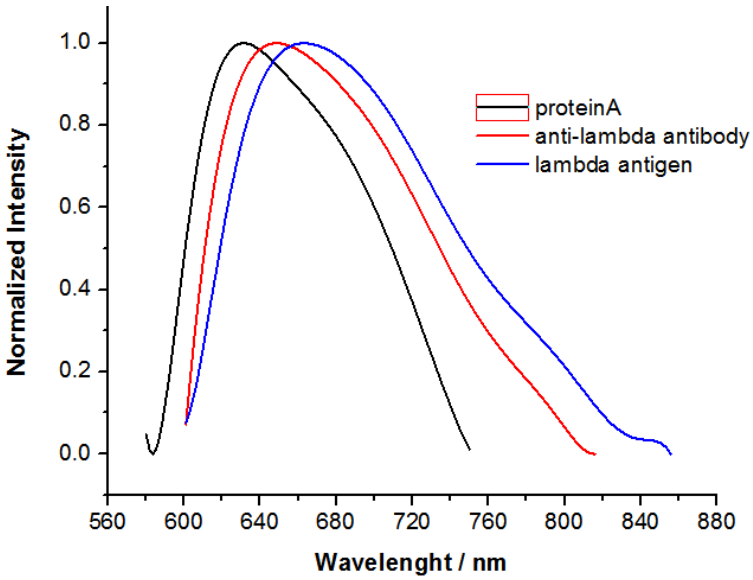

Figure 7.4 Spectral shifts detected after the functionalization of the surface with anti-lambda antigens and after the specific binding of lambda antigens.

Further, at least three controls experiment should be evaluated. The most useful control would be to test the modified surface with the wrong antigen, i.e., having an anti-lambda functionalized metal in the presence of a kappa antigens solution. If a spectral shift is detected, it should be attributed to non-specific binding and taken into consideration in any future measurements to eliminate false positives. Another control would be to test the functionalized surface against a solution without any antigens. This solution would have the same composition of diluted human plasma, rich in all the proteins and other molecules normally presents, except for the antibodies. Again, the possible spectral variation recorded should be related to non-specific binding, and considered as background noise when conducting the real test. Last, a quick test should be performed, using solutions with normal levels of kappa and lambda chains, as from an healthy person. The spectral shift, if any, should be the same on both anti-kappa or anti-lambda functionalized surfaces, as these antigens are equally present in the blood sample. In particular, these variations should be

fairly small, because the presence of the antigens is not as high as in a cancer patient, and they could constitute possible quantitative cut-off values between healthy and unhealthy.

Table 7.1 Summary of the performance achieved with large area nanoholes array made by IL for both bulk and surface sensing

Bulk Performance	
Sensitivity, S_b	1026.38 RIU
Noise, σ_s	0.18 nm
Resolution, *Res*	1.75 10^{-4} RIU

Surface Performance	
Shift detected	1nm / 10 μgmL^{-1}
Noise, σ_s	0.21 nm
Limit of Detection, *LOD*	6.02 nM

In particular for surface sensing, the results present in Table 7.1 are fairly good if compared with the other platforms studied in this thesis and various transmission measurements found in literature[12, 102]. The reason behind this achievement can be found in the large area platform characteristics. First of all, all the light coming from the objective lens is employed for the sensing, as the nanoholes completely fill (and beyond) the illuminated spot. Being the light spot size roughly 100 μm^2, for arrays of nanoholes made by FIB probed with the same setup, this is not possible, as their size is only 15x15 μm^2. The plasmonic shift is therefore measured over a larger sensing area (almost 7 times), allowing better and more robust detection of even smaller variations.

Another consideration can be also made by looking at the slightly different data collection setup. The collection of the zero-order transmitted light was made, as usual, through a fiber optic. However, the position of the core of the fiber was changed; more

specifically, the fiber was kept 1.25cm away from the gold structures. In this configuration, only the most collimated rays radiating from the surface will be collected, obtaining a more spectrally pure transmission. Particularly, this was obtained because the platform was not in the focal point of the objective lens: being out of focus implies that the light field hitting the sample is even larger than what described before. As a consequence, this type of improvement can be registered only because of the large area on which the nanoholes are spread.

The difference between the two setup configurations (collimated and focused acquisition) was clearly defined by other experiments conducted with Dr. Jacson Menezes, a Post-Doc working in Prof. Brolo lab.

Another main characteristic involved in the improved surface sensitivity is the uniformity of the sample, for two different reasons. First, if the sample is not homogeneous, the transmitted spectra will be broader and less defined. The sharpness of the peak also have an influence on the detection of spectral changes. Second, if the sample is homogeneous, it can be used for multiplexing, as the performance of each region of the platform is directly comparable with the others. In addition, due to the reproducibility of the fabrication by IL, sample-to-sample variation decreases, leading to more comparable performances. These last two considerations are the main weakness that need to be addressed of the large area nanoholes by UV nanoimprinting described in Chapter 6.

Overall, these large sensing platforms present several advantages, as multiplexing detection and the possibility to be produced in large volumes. With the performances

demonstrated in this chapter it is believed that constitute a great candidate for the development of a lab-on-a-chip type of device.

Chapter 8: Development of a Reliable Biosensing Scheme for Multiplexing

In this chapter will be presented the development and implementation of the detection scheme described in Section 4.3.2. This is possibly the first step towards reaching the ultimate miniaturized system described in the overview (Chapter 1, Figure 1.1).

The detection scheme was based on intensity monitoring, rather than wavelength interrogation, for two main reasons. First, CCD detectors are known to be very sensitive to changes in intensity, increasing the performance of the gold nanohole biosensor by lowering the LOD.[7, 19] Furthermore, the use of a wide CCD chip as readout element would introduce an important aspect that was not yet being tested in this thesis: the possibility of multiplexing. In fact, with the potential of recording images with a field of view of ~ $2mm^2$,[103] it was possible to monitor the behaviour of 7-by-7 arrangement of nanohole arrays, integrated with microfluidic channels, simultaneously.

The process of developing this detection platform was not without roadblocks and issues. This chapter will discuss how some of these problems were addressed and some of the solutions achieved. The final results and data obtained with the setup developed so far will also be presented.

8.1 Hardware Characterization

Once the optical setup, described in Section 4.3.2, was implemented, the first tests with nanohole array samples fabricated by FIB were performed. Some of those tests simply required the transmission of light through the holes and monitor the intensity response to evaluate the stability of the system. Figure 8.1 represents an early example of the outcome,

plotted as normalized intensity versus time. Each line represents the signal transmitted through one array. The structures were exposed to air, as no liquid was present inside the microfluidic channels. The images were collected for 100 μs each, with an interval of 1 second between them.

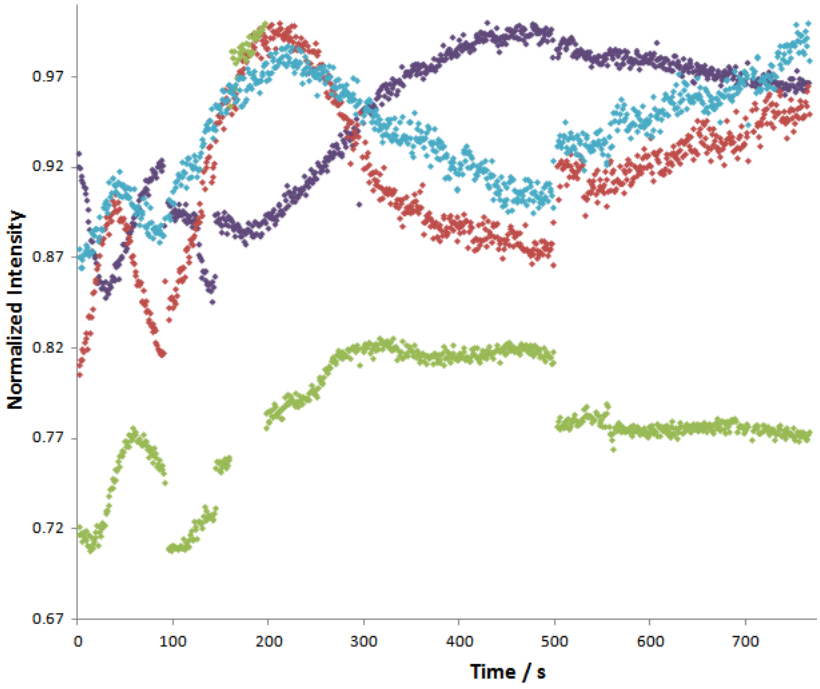

Figure 8.1 Transmitted intensity monitored in time. The nanoholes arrays are in air presented large oscillations of the signal. The issue will be addressed throughout the chapter.

Very large signal fluctuations (when it should be a flat line) are shown in Figure 8.1that could not be attributed to any effect related to the sample. Instead, the reason could rely on the different components of the optical system and possible environmental interferences (temperature variation, vibrations, humidity, etc).

Therefore, this section will be a systematic walk through each of these components and aspects, with some descriptions of the testing performed to characterize them, and the attempts to solve each of the issues.

8.1.1 Environmental Interference

Temperature was one of the first elements thought to cause the oscillations in the data. In fact, it is know in the literature that the refractive index of water changes 10^{-4} RIU per 1 degree Celsius.[104] This value is much higher than the resolution sought (10^{-7} RIU) and obtained[7, 19] for this type of setup, therefore a tighter temperature control was needed.

As the room is not temperature controlled, it was thought to create a sealed macro-environment around the setup to have stable temperature during the experiments. However, the temperature variation that mainly would affect the outcome would be the one happening in the solutions inside the microfluidic channels. For this reason, a feedback control was created with a LabView program, micrometer-size thermocouple (NI USB-TC01, National Instrument)and a flexible silicon heater (Omegalux, SRFR series). The thermocouple was positioned inside one of the channels dispensing solutions onto the arrays. The temperature reading was recorded by the program, which would adjust the voltage of the heater positioned on top of the syringes dispensing the liquid.

Figure 8.2 represents the two situations with and without the temperature feedback. With the blue curve, the temperature of the solutions fluctuates significantly, reflecting the slow equilibrium being reached inside the macro-environment created. On the other hand, shown by the red curve, with the feedback control the temperature was set and maintained slightly higher than the environment, resulting in a much stable behavior.

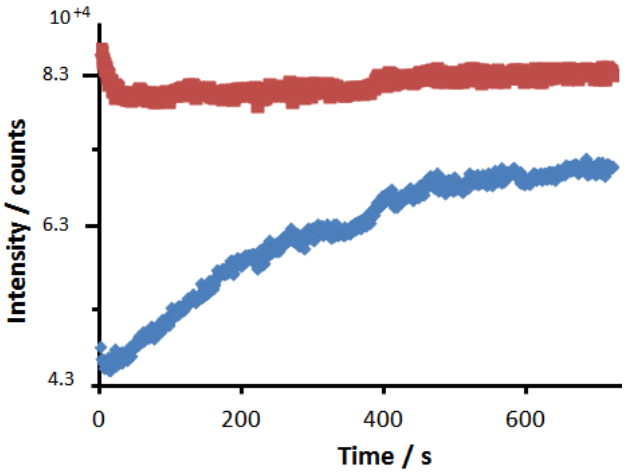

Figure 8.2 Intensity fluctuation when the temperature is left equilibrating with the environment (blue curve) or stabilized by the feedback system developed (red curve).

The LabView program was developed with the help of Andrew MacDonald, an electronics expert working in the Dept. of Chemistry. Although the issue was not yet completely solved, we believe that this achievement improved the system and will become very useful when lower resolutions and LOD will be sought.

8.1.2 Opto-mechanic

Another aspectthat needed control was the mechanics and the optics involved in the setup. The components were reduced to the essential minimum, shortening the light path and decreasing sources of fluctuation. The fact that the optics was maintained simple was also seen as advantage for future translation into possible portable devices. The light from the laser source was monitored at each level of interaction with the optics, excluding each element to be source of visible variation. Once it was confirmed that everything was

perfectly aligned, the attention was moved onto the two major reasons possibly causing the oscillations recorded: the laser source and the CCD detector.

8.1.3 Light Source

With always the idea of future miniaturization in mind, a compact, but stable, diode laser was implemented as light source for the system. The Coherent Ultra Low Noise laser diode module was chosen in particular for the following characteristics[105]:

- Root Mean Square (RMS) noise <0.06%
- Power stability ±1%
- Wavelength = 635 ±5 nm
- Temperature coefficient 0.2nm / ^{o}C
- No warm-up time

The source was tested by recording the laser intensity for 30 minutes with a photodiode connected to an oscilloscope (TPS2000B, Tektronix). The outcome is represented in Figure 8.3, as voltage plotted versus time. It was observed the following:

- RMS Noise < 0.73%
- Power stability ±1%

It was concluded that this source, although stable, does not quiet perform as described in the RMS Noise specifications. It should be more than sufficient for preliminary test and bulk sensing; however, the difference might be large enough to generate noise that would interfere with the sensing of biomolecules on the surface, decreasing the performance and the LOD.

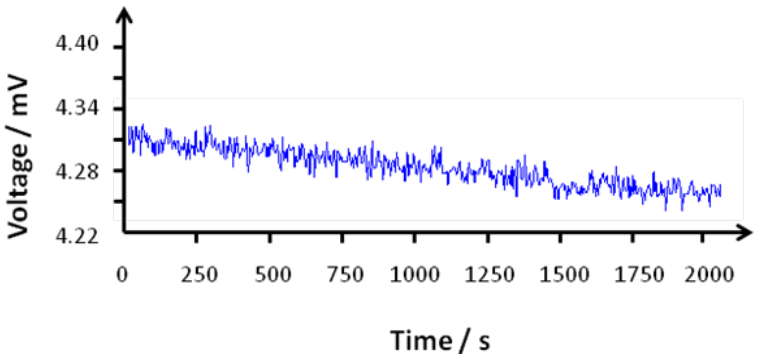

Figure 8.3 Laser stability measured in time through a photodiode connected to an oscilloscope

8.1.4 CCD Detector

The HQ2 CoolSnap CCD from Photometrics was the detector implemented in the setup. Unfortunately, it was soon discovered that it might have been the main cause of the signal fluctuation. First to be noticed were the variations generated by the fan, positioned on the rear of the device, to cool the camera. When a Michelson interferometer was built on top of the camera, clearly the interference fringes were seen oscillating only when the fan was turned on.

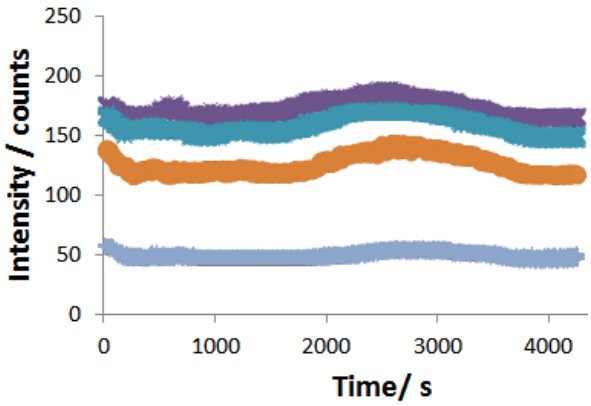

Figure 8.4 Improvements obtained in the intensity stability after forced transfer of the fan oscillations onto the active vibration isolation table by means of an heavy object

The only possible way thought to improve the situation was to place an heavy object on the camera, in order to transfer all the vibration to the active air-dumping table. Definitely some improvements were seen, as depicted in Figure 8.4. The graph represents the variation of intensity in time after the weight was placed. The different curves are for the behavior of different nanoholes arrays. However, this did not solve all the problems. In fact, even with the vibration being dumped, in most of the cases a fairly large oscillation was still seen (as in the orange curve above).

It was noticed that the response of the camera required some time before becoming stable, and the amount of time needed could vary without prediction, lasting sometimes hours. Very likely, the thermoelectric cooling of the device might need to be adjusted.

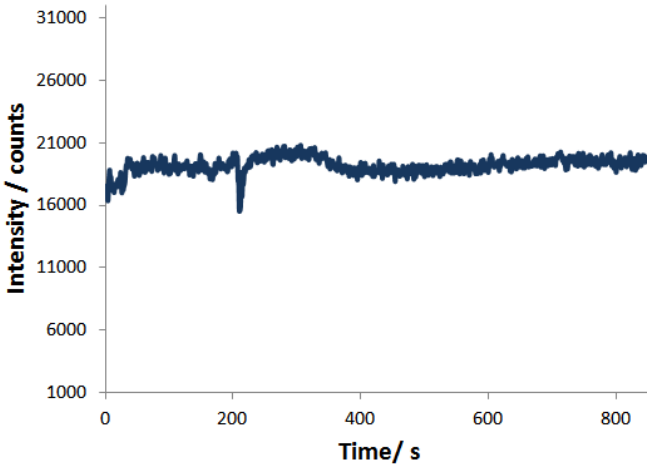

Figure 8.5 Transmitted intensity in function of time recorded with the iDus Andor CCD camera

As a final proof-of-concept, another CCD camera, an iDus camera by Andor, was used to collect the same data. In repeating the test, the light transmitted through the arrays was monitored. In Figure 8.5 is plotted the result, again, as intensity in respect of time from

one single array. Without any waiting time it was found a much higher overall stability, confirming that the previous detector wasthe main source of the variations.

However, although much more stable, there were two intrinsic roadblocks preventing the use of this camera as definitive detector for the system. First of all, the camera has no electronic shutter: this translated into a “ghost” or smear effect on the images. This effect can be clearly seen in the Figure 8.6, where the nanoholes arrays inside microfluidic channels are represented. In fact, the readout time is so long that during the reading of the signal, the pixel are still collecting photons, adding unwanted artifacts to the evaluation of the intensity values.

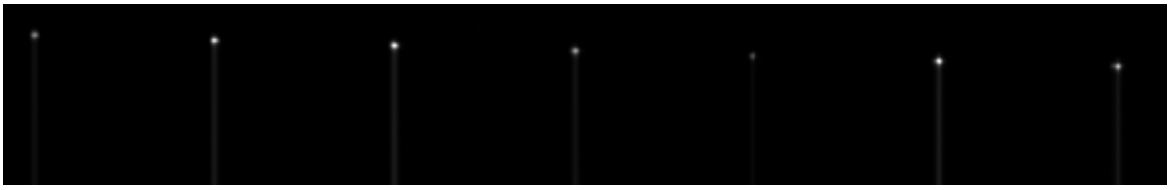

Figure 8.6 Smearing of the signal due to the lack of an electronic shutter. The unwanted light could add large artifact when evaluating the information

The other problem can also be seen in Figure 8.6. In fact, only one row of the 7 by 7 arrays can be monitored at the same time, reducing the possibility of multiplexing and data averaging.

The fact of having 7 different columns was very important for the biosensing performance of the platform, particular for the leukemia experiments that we envisioned.

Our final goal was the detection of leukemia cancer markers, and in particular the ratio between two molecules, the lambda and the kappa antigens. Therefore, both molecules need to be detected at the same time, for direct comparison. Some controls need to be performed

as well, to prove the reliability of the system and discard possible non specific binding results or false positives, as described in Section7.3.

The ideal leukemia diagnose sensing experiment devised was as following:

- Three columns of nanohole arrays would be modified with anti-lambda antibodies, and three with anti-kappa antibodies; a seventh column would be left unmodified. The surface chemistry would be done using a microfluidic chip.
- The three columns containing arrays functionalized with the same antibodies would receive the following solutions: kappa-antigen blood sample, lambda-antigen blood sample and a control (growth medium). In this way, the detection of specific cancer markers would have two specific controls *in situ.*
- The unmodified arrays, would be exposed to PBS only, to determine possible fluctuations or intensity changes due to the light source or environmental interference.

The number of rows, as the number of nanohole arrays present in the same microfluidic channels, should have been at least three. The data from the different arrays would have been averaged, for a more reliable test and a more statistically robust outcome. In order to reach this ideal situation, the setup was characterized, although it was not perfectly optimized. The characterization was obtained working at the optimum conditions available to establish a performance baseline, described hereafter, that in the future could only be further improved.

8.2 Preliminary Results

As always, the device was tested for bulk and surface sensing, before approaching the medical application (leukemia detection). In all the results outlined below, nanoholes made by FIB were used as the sensing platform. The diameter of the structures was 250nm, while the periodicity of the arrays were chosen to be 450nm for two reasons: first, it was proven in Section 5.4.3 to be one of the most performing combination of geometrical parameters.

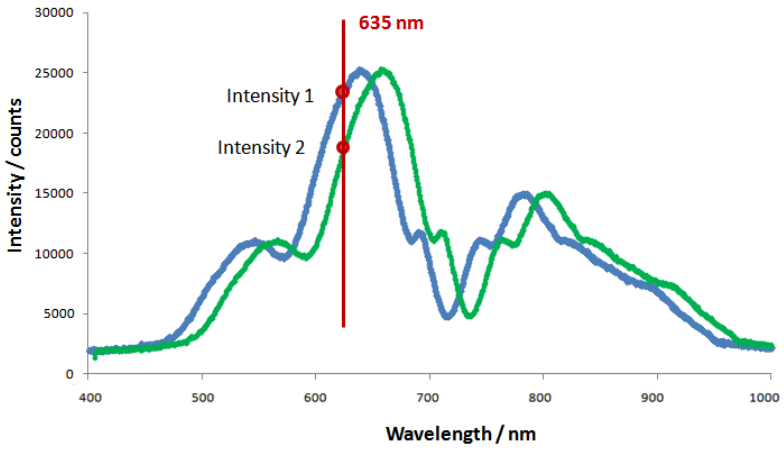

Figure 8.7 Transmission spectra of the nanohole arrays used and the light source wavelength, marked at 633nm with the vertical red line. The positioning of the exciting light on the steep slope of the resonant peak allows better detection of any possible shifts

Most important, as represented in Figure 8.7, the wavelength of the laser (635 nm, red vertical line) is probing a very steep part of the plasmonic resonant peak. Any red-shift of the curve due to changes on the surface would be easily detected as a lower transmitted intensity. The event would reflect the situation represented by the points named Intensity 1 and Intensity 2 in Figure 8.7.

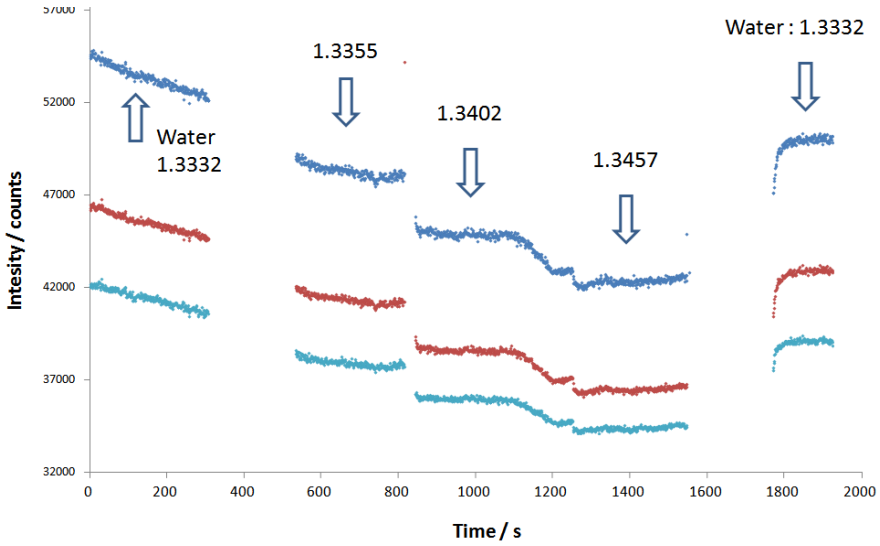

Figure 8.8 Intensity variation when the arrays are exposed to solutions of different refractive indexes.

Figure 8.8 represent the results from an experiment for bulk refractive index sensing. The change in intensity has been plotted against time, following the exposure of three arrays to solutions of different refractive indexes, as indicated. The data collected revealed a bulk sensitivity of 2897 ΔI% / RIU. Despite the much larger performance in comparison to the value obtained in the previous sections, due to the noise of the setup, the resolution was only 1.6 10^{-4}RIU. This value is clearly far from the expected resolution for this type of measuring system.

The noise became even more influent when the surface sensitivity was evaluated. Figure 8.9 depicts the intensity behaviour recorded when the biotinylated arrays were exposed to different concentrations of SA: 1.25 μg/mL, 2.5 μg/mL and 5 μg/mL. From the graph it is possible to see a decreasing in intensity due to the streptavidin molecules binding onto the surface. The surface sensitivity was calculated by taking the average intensity of the initial PBS solution and the PBS data points after each SA binding event.

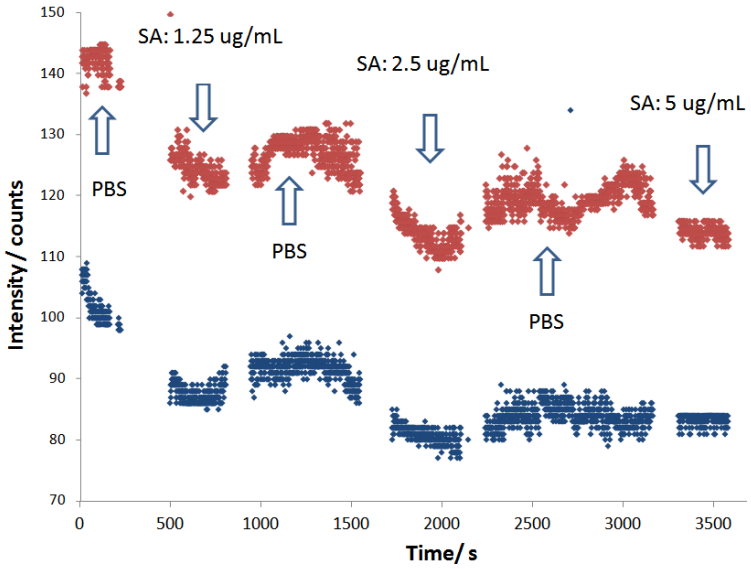

Figure 8.9 Intensity behavior in respect of time, when the nanoholes arrays modified with biotin were exposed to different concentrations of SA (1.25 µg/mL, 2.5 µg/mL and 5 µg/mL).

The performance was 3.6 nm/µgmL^{-1}, higher than what encounter before for large area nanohole arrays, but probably not as reliable. Unfortunately, the large noise does not allow the determination of an LOD value for this experiment.

Having great care in monitoring the stabilization of the system, and after the above improvements were implemented, some surface sensing experiments involving the leukemia cancer markers were performed. The gold surface was functionalized with anti-lambda antibodies. Four different solutions were flown over the arrays in four different microfluidic channels, as described before. The solutions were lambda-antigen solution; kappa-antigen solution; growing media, without any antigens as first control; PBS as second control.

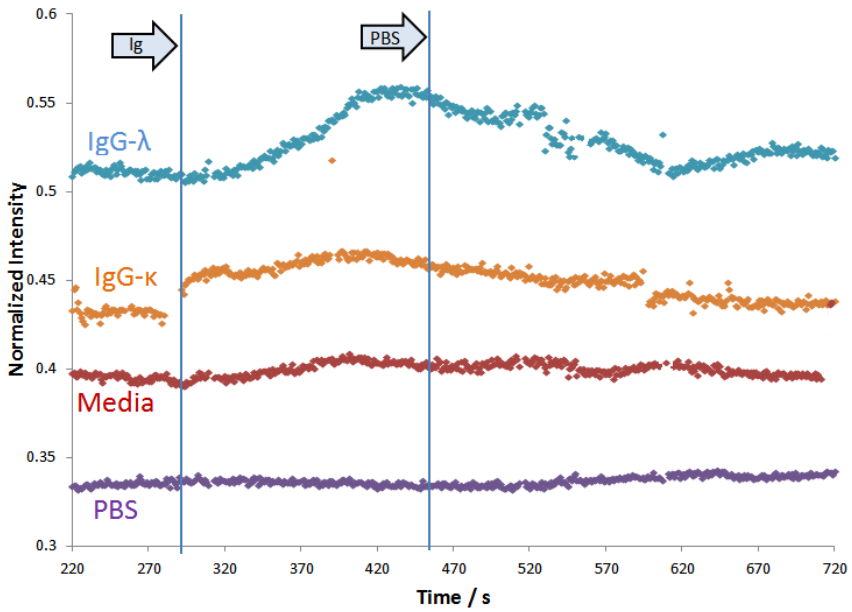

Figure 8.10 Intensity variation in respect of time of the transmitted light after the exposure to different blood samples. The surface of the nanoholes was modified with anti-lambda antibodies. The two vertical lines mark, respectively, the introduction of the different solutions and the PBS for the washing step in the microfluidic system.

Figure 8.10 represent the behavior of the normalized intensity when each different sensing element was exposed to the different solutions. Clearly, when the lambda antigen reached the surface, the specific binding with its antibody generated the largest intensity change, as predicted. The kappa-antigen solution and the growing media generated a small variation as well, demonstrating the occurring of false-positive events and non-specific binding. The PBS signal, at the bottom, reflects the overall stability of the system.

The experiment was repeated another two times, with the respective outcomes represented in Figure 8.11.

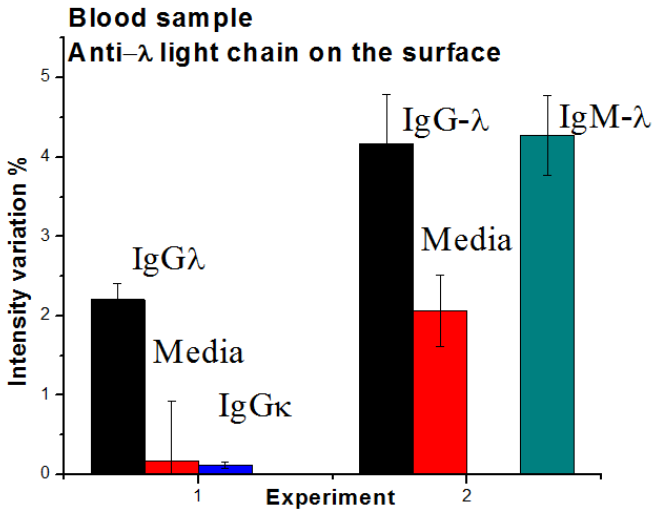

Figure 8.11 Specific detection of the leukemia cancer marker in respect of the growth medium as control, for two other experiments. The error bars were calculated over the 7 nanohole arrays exposed to the same solution.

Here the average percentage intensity variation is summarized and plotted for the different solutions being tested. The error bars indicate the variability encountered for all the 7 arrays present in the same microfluidic channel. In both cases, non-specific binding, generated by the physisorption of the numerous molecules present in the growing media, is fairly large. However, it can be statistically distinguished from the detection of the real antigen, the lambda light chain.

In conclusion, the detection scheme for intensity modulation sensing has been developed and characterized. Although with some issues of stability, this instrumentation has been proven able to achieve performances comparable to other detection scheme previously used, demonstrating lot of potential.

Chapter 9: Conclusion

In this thesis, it was demonstrated that periodic plasmonic structures are promising sensing platforms that combine the regular advantages of SPR (surface-specific label-free sensing) with the possibility of enhanced optical and fluidic integrations. In particular, arrays of nanoholes in metal thin films can now be mass-fabricated at low-cost by several different approaches, indicating that barriers for their commercialization at competitive prices are no longer a limitation. This thesis reported SPR sensor applications using platforms fabricated by FIB, IL and UV Nanoimprinting. The quality of the sensors was indicated by using bulk and surface sensitivities, *LOD*s and resolutions as common performance evaluation parameters. The resolution appears to be the best parameter to compare different sensors, since it takes into account both the sensitivity and the noise.

For easy comparison, Table 9.1belowsummarizes the findings of the performances for all the structures studied in this project.

Table 9.1 Summary of the performance values obtained for all the periodic structures studied. Transmission and Intensity define the different type of data monitoring and acquisition.

	Transmission				**Intensity**
Fabrication	*FIB circular*	*FIB slit-TE*	*IL*	*UV-Nanoim.*	*FIB*
Sb, nm / RIU	792	628.5	1026	2870	2897 ΔI% / RIU
Sc, nm/μgmL^{-1}	0.73	1.33	3.31	1.22	3.6
Res, RIU	-	-	1.75 10^{-4}	3.31 10^{-4}	1.6 10^{-4}

It is possible to see that large area nanoholes arrays present much larger values of sensitivities relative to the FIB fabricated structures. In particular, structures fabricated by UV Nanoimprinting seem to achieve more than double of the surface sensitivity of the nanoholes fabricated by IL. However, the lack of homogeneity and the detection noise decreased their resolution.IL is a more reliable fabrication method and the IL structures were found to yield better surface sensitivity, demonstrating that they can be considered viable substrates in the construction of cheaper biosensing devices.

The last column of Table 9.1displaysthe results obtained with intensity modulation-type measurements. Although the setup is not yet optimized, it was demonstrated its capability by reaching comparable performance values as the other transmission detection schemes. With further instrumental improvements, there is no doubt that this setup could achieve better performances, putting us closer the gold standard, the Krestchmann-Raether SPR configuration (Section 2.1).

It seems clear that pursuing of new types of periodic plasmonic sensors will continue to grow, driven by the need of better label free sensing elements. The advantage in terms of miniaturization and multiplexing of the platforms and the setup characterized in this thesis place them in an unique position to make a significant impact in the next generation of sensor devices, including point-of-care technologies.

Bibliography

1. Brolo, A. G., Plasmonics for future biosensors. *Nature Photonics* **2012,** *6* (11), 709-713.
2. Homola, J., *Surface Plasmon Based Sensor*. Springer: 2006.
3. R. B. Richard, B. M. S., A. J. Tudos, *Handbook Of Surface PLasmon Resonance*. RSC Publishing: 2008.
4. Wijaya, E.; Lenaerts, C.; Maricot, S.; Hastanin, J.; Habraken, S.; Vilcot, J.-P.; Boukherroub, R.; Szunerits, S., Surface plasmon resonance-based biosensors: From the development of different SPR structures to novel surface functionalization strategies. *Current Opinion in Solid State & Materials Science* **2011,** *15* (5), 208-224.
5. Escobedo, C.; Brolo, A. G.; Gordon, R.; Sinton, D., Optofluidic Concentration: Plasmonic Nanostructure as Concentrator and Sensor. *Nano Letters* **2012,** *12* (3), 1592-1596.
6. Escobedo, C.; Brolo, A. G.; Gordon, R.; Sinton, D., Flow-Through vs Flow-Over: Analysis of Transport and Binding in Nanohole Array Plasmonic Biosensors. *Analytical Chemistry* **2010,** *82* (24), 10015-10020.
7. Yang, J.-C.; Ji, J.; Hogle, J. M.; Larson, D. N., Multiplexed plasmonic sensing based on small-dimension nanohole arrays and intensity interrogation. *Biosensors & bioelectronics* **2009,** *24* (8), 2334-2338.
8. Stoeva, S. I.; Lee, J.-S.; Smith, J. E.; Rosen, S. T.; Mirkin, C. A., Multiplexed Detection of Protein Cancer Markers with Biobarcoded Nanoparticle Probes. *Journal of the American Chemical Society* **2006,** *128* (26), 8378-8379.
9. Naimushin, A. N.; Soelberg, S. D.; Nguyen, D. K.; Dunlap, L.; Bartholomew, D.; Elkind, J.; Melendez, J.; Furlong, C. E., Detection of Staphylococcus aureus enterotoxin B at femtomolar levels with a miniature integrated two-channel surface plasmon resonance (SPR) sensor. *Biosensors and Bioelectronics* **2002,** *17* (6–7), 573-584.
10. Frasconi, M.; Tortolini, C.; Botrè, F.; Mazzei, F., Multifunctional Au Nanoparticle Dendrimer-Based Surface Plasmon Resonance Biosensor and Its Application for Improved Insulin Detection. *Analytical Chemistry* **2010,** *82* (17), 7335-7342.
11. Sim, H. R.; Wark, A. W.; Lee, H. J., Attomolar detection of protein biomarkers using biofunctionalized gold nanorods with surface plasmon resonance. *Analyst* **2010,** *135* (10), 2528-2532.
12. Ferreira, J.; Santos, M. J. L.; Rahman, M. M.; Brolo, A. G.; Gordon, R.; Sinton, D.; Girotto, E. M., Attomolar Protein Detection Using in-Hole Surface Plasmon Resonance. *Journal of the American Chemical Society* **2009,** *131* (2), 436-+.
13. Karabchevsky, A.; Krasnykov, O.; Auslender, M.; Hadad, B.; Goldner, A.; Abdulhalim, I., Theoretical and Experimental Investigation of Enhanced Transmission Through Periodic Metal Nanoslits for Sensing in Water Environment. *Plasmonics* **2009,** *4* (4), 281-292.
14. Genet, C.; Ebbesen, T. W., Light in tiny holes. *Nature* **2007,** *445* (7123), 39-46.
15. Garcia-Vidal, F. J.; Martin-Moreno, L.; Ebbesen, T. W.; Kuipers, L., Light passing through subwavelength apertures. *Reviews of Modern Physics* **2010,** *82* (1), 729-787.

16. Gordon, R.; Sinton, D.; Kavanagh, K. L.; Brolo, A. G., A new generation of sensors based on extraordinary optical transmission. *Accounts of Chemical Research* **2008,** *41* (8), 1049-1057.
17. Blanchard-Dionne, A. P.; Guyot, L.; Patskovsky, S.; Gordon, R.; Meunier, M., Intensity based surface plasmon resonance sensor using a nanohole rectangular array. *Opt. Express* **2011,** *19* (16), 15041-15046.
18. Stark, P. R. H.; Halleck, A. E.; Larson, D. N., Short order nanohole arrays in metals for highly sensitive probing of local indices of refraction as the basis for a highly multiplexed biosensor technology. *Methods* **2005,** *37* (1), 37-47.
19. Lesuffleur, A.; Im, H.; Lindquist, N. C.; Lim, K. S.; Oh, S.-H., Laser-illuminated nanohole arrays for multiplex plasmonic microarray sensing. *Opt. Express* **2008,** *16* (1), 219-224.
20. Escobedo, C.; Vincent, S.; Choudhury, A. I. K.; Campbell, J.; Brolo, A. G.; Sinton, D.; Gordon, R., Integrated nanohole array surface plasmon resonance sensing device using a dual-wavelength source. *Journal of Micromechanics and Microengineering 21* (11).
21. www.Biacore.com.
22. Lesuffleur, A.; Im, H.; Lindquist, N. C.; Oh, S.-H., Periodic nanohole arrays with shape-enhanced plasmon resonance as real-time biosensors. *Applied Physics Letters* **2007,** *90* (24).
23. Koerkamp, K. J. K.; Enoch, S.; Segerink, F. B.; van Hulst, N. F.; Kuipers, L., Strong Influence of Hole Shape on Extraordinary Transmission through Periodic Arrays of Subwavelength Holes. *Physical Review Letters* **2004,** *92* (18), 183901.
24. van der Molen, K. L.; Segerink, F. B.; van Hulst, N. F.; Kuipers, L., Influence of hole size on the extraordinary transmission through subwavelength hole arrays. *Applied Physics Letters* **2004,** *85* (19), 4316-4318.
25. Gordon, R. B., A. G.; McKinnon, A.; Rajora, A.; Leathem, B.; Kavanagh, K. L., Strong Polarization in the Optical Transmission through Elliptical Nanohole Arrays *Physical Review Letters* **2004,** *92* (3).
26. Correia-Ledo, D.; Gibson, K. F.; Dhawan, A.; Couture, M.; Tuan, V.-D.; Graham, D.; Masson, J.-F., Assessing the Location of Surface Plasmons Over Nanotriangle and Nanohole Arrays of Different Size and Periodicity. *Journal of Physical Chemistry C* **2012,** *116* (12), 6884-6892.
27. Peters, J. H., Status of EUVL mask development in Europe. In *Photomask and Next-Generation Lithography Mask Technology XII, Pts 1 and 2*, Komuro, M., Ed. 2005; Vol. 5853, pp 297-307.
28. Gates, B. D.; Xu, Q. B.; Stewart, M.; Ryan, D.; Willson, C. G.; Whitesides, G. M., New approaches to nanofabrication: Molding, printing, and other techniques. *Chemical Reviews* **2005,** *105* (4), 1171-1196.
29. Chen, J.; Shi, J.; Decanini, D.; Cambril, E.; Chen, Y.; Haghiri-Gosnet, A.-M., Gold nanohole arrays for biochemical sensing fabricated by soft UV nanoimprint lithography. *Microelectronic Engineering* **2009,** *86* (4-6), 632-635.
30. Menezes, J. W.; Ferreira, J.; Santos, M. J. L.; Cescato, L.; Brolo, A. G., Large-Area Fabrication of Periodic Arrays of Nanoholes in Metal Films and Their Application in Biosensing and Plasmonic-Enhanced Photovoltaics. *Advanced Functional Materials* **2010,** *20* (22), 3918-3924.
31. http://seer.cancer.gov/statfacts/html/clyl.html.

32. C. Valsecchi, A. G. B., Periodic Metallic Nanostructures as Plasmonic Chemical Sensors. *Langmuir* **2013,** *accepted*.
33. Maier, S. A., *Plasmonics: fundamentals and applications*. Springer: New York, 2007.
34. Raether, H., *Surface Plasmons on smooth and rough surfaces and on gratings*. Springer-Verlag: Berlin, 1988.
35. Barnes, W. L., Surface plasmon-polariton length scales: a route to sub-wavelength optics. *Journal of Optics a-Pure and Applied Optics* **2006,** *8* (4), S87-S93.
36. Dawson, P.; Puygranier, B. A. F.; Goudonnet, J. P., Surface plasmon polariton propagation length: A direct comparison using photon scanning tunneling microscopy and attenuated total reflection. *Physical Review B* **2001,** *63* (20), 205410.
37. Ritchie, R. H.; Arakawa, E. T.; Cowan, J. J.; Hamm, R. N., SURFACE-PLASMON RESONANCE EFFECT IN GRATING DIFFRACTION. *Physical Review Letters* **1968,** *21* (22), 1530-&.
38. Barnes, W. L.; Dereux, A.; Ebbesen, T. W., Surface plasmon subwavelength optics. *Nature* **2003,** *424* (6950), 824-830.
39. http://en.wikipedia.org/wiki/File:Dispersion_Relationship.png.
40. Kretschm.E; Raether, H., PLASMA RESONANCE EMISSION IN SOLIDS. *Zeitschrift Fur Naturforschung Part a-Astrophysik Physik Und Physikalische Chemie* **1968,** *A 23* (4), 615-&.
41. Roh, S.; Chung, T.; Lee, B., Overview of the Characteristics of Micro- and Nano-Structured Surface Plasmon Resonance Sensors. *Sensors* **2011,** *11* (2), 1565-1588.
42. Ji, J.; Yang, J.-C.; Larson, D. N., Nanohole arrays of mixed designs and microwriting for simultaneous and multiple protein binding studies. *Biosensors and Bioelectronics* **2009,** *24* (9), 2847-2852.
43. Correia-Ledo, D.; Gibson, K. F.; Dhawan, A.; Couture, M.; Tuan, V.-D.; Graham, D.; Masson, J.-F., Assessing the Location of Surface Plasmons Over Nanotriangle and Nanohole Arrays of Different Size and Periodicity. *Journal of Physical Chemistry C 116* (12), 6884-6892.
44. Charbonneau, R.; Tencer, M.; Lahoud, N.; Berini, P., Demonstration of surface sensing using long-range surface plasmon waveguides on silica. *Sensors and Actuators B: Chemical* **2008,** *134* (2), 455-461.
45. Rispens, T.; te Velthuis, H.; Hemker, P.; Speijer, H.; Hermens, W.; Aarden, L., Label-free assessment of high-affinity antibody–antigen binding constants. Comparison of bioassay, SPR, and PEIA-ellipsometry. *Journal of Immunological Methods* **2011,** *365* (1–2), 50-57.
46. Shalabney, A.; Abdulhalim, I., Electromagnetic fields distribution in multilayer thin film structures and the origin of sensitivity enhancement in surface plasmon resonance sensors. *Sensors and Actuators A: Physical* **2010,** *159* (1), 24-32.
47. Martín-Moreno, L.; García-Vidal, F. J.; Lezec, H. J.; Pellerin, K. M.; Thio, T.; Pendry, J. B.; Ebbesen, T. W., Theory of Extraordinary Optical Transmission through Subwavelength Hole Arrays. *Physical Review Letters* **2001,** *86* (6), 1114-1117.
48. De Leebeeck, A.; Kumar, L. K. S.; de Lange, V.; Sinton, D.; Gordon, R.; Brolo, A. G., On-chip surface-based detection with nanohole arrays. *Analytical Chemistry* **2007,** *79* (11), 4094-4100.

49. Campbell, C. T.; Kim, G., SPR microscopy and its applications to high-throughput analyses of biomolecular binding events and their kinetics. *Biomaterials* **2007,** *28* (15), 2380-2392.
50. Kim, S. A.; Byun, K. M.; Kim, K.; Jang, S. M.; Ma, K.; Oh, Y.; Kim, D.; Kim, S. G.; Shuler, M. L.; Kim, S. J., Surface-enhanced localized surface plasmon resonance biosensing of avian influenza DNA hybridization using subwavelength metallic nanoarrays. *Nanotechnology* **2010,** *21* (35), 355503-355503.
51. Markowicz, P. P.; Law, W. C.; Baev, A.; Prasad, P. N.; Patskovsky, S.; Kabashin, A., Phase-sensitive time-modulated surface plasmon resonance polarimetry for wide dynamic range biosensing. *Opt. Express* **2007,** *15* (4), 1745-1754.
52. Im, H.; Lee, S. H.; Wittenberg, N. J.; Johnson, T. W.; Lindquist, N. C.; Nagpal, P.; Norris, D. J.; Oh, S.-H., Template-Stripped Smooth Ag Nanohole Arrays with Silica Shells for Surface Plasmon Resonance Biosensing. *Acs Nano* **2011,** *5* (8), 6244-6253.
53. Zhao, H.; Brown, Patrick H.; Schuck, P., On the Distribution of Protein Refractive Index Increments. *Biophysical Journal* **2011,** *100* (9), 2309-2317.
54. Stenberg, E.; Persson, B.; Roos, H.; Urbaniczky, C., Quantitative determination of surface concentration of protein with surface plasmon resonance using radiolabeled proteins. *Journal of Colloid and Interface Science* **1991,** *143* (2), 513-526.
55. Livnah, O.; Bayer, E. A.; Wilchek, M.; Sussman, J. L., Three-dimensional structures of avidin and the avidin-biotin complex. *Proceedings of the National Academy of Sciences* **1993,** *90* (11), 5076-5080.
56. Love, J. C.; Estroff, L. A.; Kriebel, J. K.; Nuzzo, R. G.; Whitesides, G. M., Self-Assembled Monolayers of Thiolates on Metals as a Form of Nanotechnology. *Chemical Reviews* **2005,** *105* (4), 1103-1170.
57. Decher, G.; Lehr, B.; Lowack, K.; Lvov, Y.; Schmitt, J., New nanocomposite films for biosensors: layer-by-layer adsorbed films of polyelectrolytes, proteins or DNA. *Biosensors and Bioelectronics* **1994,** *9* (9–10), 677-684.
58. Lvov, Y.; Decher, G.; Moehwald, H., Assembly, structural characterization, and thermal behavior of layer-by-layer deposited ultrathin films of poly(vinyl sulfate) and poly(allylamine). *Langmuir* **1993,** *9* (2), 481-486.
59. Caruso, F.; Furlong, D. N.; Ariga, K.; Ichinose, I.; Kunitake, T., Characterization of Polyelectrolyte−Protein Multilayer Films by Atomic Force Microscopy, Scanning Electron Microscopy, and Fourier Transform Infrared Reflection−Absorption Spectroscopy. *Langmuir* **1998,** *14* (16), 4559-4565.
60. Stewart, M. E.; Yao, J. M.; Maria, J.; Gray, S. K.; Rogers, J. A.; Nuzzo, R. G., Multispectral Thin Film Biosensing and Quantitative Imaging Using 3D Plasmonic Crystals. *Anal Chem* **2009,** *81* (15), 5980-5989.
61. Lide, D. R., *Handbook of Chemistry Physics*
71st ed ed.; CRC: Boston, 1990.
62. Wilkins, D. K.; Grimshaw, S. B.; Receveur, V.; Dobson, C. M.; Jones, J. A.; Smith, L. J., Hydrodynamic Radii of Native and Denatured Proteins Measured by Pulse Field Gradient NMR Techniques†. *Biochemistry* **1999,** *38* (50), 16424-16431.
63. Justino, C. I. L.; Rocha-Santos, T. A.; Duarte, A. C., Review of analytical figures of merit of sensors and biosensors in clinical applications. *Trac-Trends in Analytical Chemistry 29* (10), 1172-1183.

64. Tobiška, P.; Homola, J., Advanced data processing for SPR biosensors. *Sensors and Actuators B: Chemical* **2005,** *107* (1), 162-169.
65. Lesuffleur, A.; Kumar, L. K. S.; Gordon, R., Enhanced second harmonic generation from nanoscale double-hole arrays in a gold film. *Applied Physics Letters* **2006,** *88* (26), 261104-3.
66. www.biology.arizona.edu/immunology.
67. Kyrtsonis, M. C.; Vassilakopoulos, T. P.; Kafasi, N.; Sachanas, S.; Tzenou, T.; Papadogiannis, A.; Galanis, Z.; Kalpadakis, C.; Dimou, M.; Kyriakou, E.; Angelopoulou, M. K.; Dimopoulou, M. N.; Siakantaris, M. P.; Dimitriadou, E. M.; Kokoris, S. I.; Panayiotidis, P.; Pangalis, G. A., Prognostic value of serum free light chain ratio at diagnosis in multiple myeloma. *British journal of haematology* **2007,** *137* (3), 240-3.
68. Volkert, C. A.; Minor, A. M., Focused Ion Beam Microscopy and Micromachining. *MRS Bulletin* **2007,** *32* (05), 389-399.
69. http://www.stehm.uvic.ca/research/gallery/daily/.
70. http://www1.appstate.edu/dept/physics/coffey/annie/fb2100.html.
71. Menezes, J. W.; Ferreira, J.; Santos, M. J. L.; Cescato, L.; Brolo, A. G., Large-Area Fabrication of Periodic Arrays of Nanoholes in Metal Films and Their Application in Biosensing and Plasmonic-Enhanced Photovoltaics. *Advanced Functional Materials 20* (22), 3918-3924.
72. Rodriguez, A.; Echeverria, M.; Ellman, M.; Perez, N.; Verevkin, Y. K.; Peng, C. S.; Berthou, T.; Wang, Z.; Ayerdi, I.; Savall, J.; Olaizola, S. M., Laser interference lithography for nanoscale structuring of materials: From laboratory to industry. *Microelectronic Engineering* **2009,** *86* (4-6), 937-940.
73. Hecht, E., *Optics*. Addison-Wesley: 2002.
74. http://microchem.com/PDFs_Dow/S1800.pdf.
75. http://www.ntt-at.com/products_e/Nanoimprint_custom/.
76. Nagpal, P.; Lindquist, N. C.; Oh, S.-H.; Norris, D. J., Ultrasmooth Patterned Metals for Plasmonics and Metamaterials. *Science* **2009,** *325* (5940), 594-597.
77. http://www.molecularimprints.com/products/nutera_hd7000.php.
78. Corporation., H. H. T., *Lets familiarize ourselves with the SEM*. 2009.
79. http://www.ammrf.org.au/myscope/sem/background/concepts/interactions.php.
80. http://www.nist.gov/pml/data/xraytrans/index.cfm.
81. Huntington, M. D.; Odom, T. W., A Portable, Benchtop Photolithography System Based on a Solid-State Light Source. *Small* **2011,** *7* (22), 3144-3147.
82. http://www.ece.gatech.edu/research/labs/vc/theory/photolith.html.
83. http://www.nanoterra.com/soft_lithography.asp.
84. http://www1.appstate.edu/dept/physics/coffey/annie/fb2100.html.
85. http://www.uiowa.edu/~cmrf/courses/S-4800%20Instruction%20Manual.pdf.
86. Das, M.; Hohertz, D.; Nirwan, R.; Brolo, A. G.; Kavanagh, K. L.; Gordon, R., Improved Performance of Nanohole Surface Plasmon Resonance Sensors by the Integrated Response Method. *Ieee Photonics Journal* **2011,** *3* (3), 441-449.
87. Zhou, Y.; Xu, H.; Dahlin, A. B.; Vallkil, J.; Borrebaeck, C. A. K.; Wingren, C.; Liedberg, B.; Hook, F., Quantitative interpretation of gold nanoparticle-based bioassays designed for detection of immunocomplex formation. *Biointerphases* **2007,** *2* (1), 6-15.
88. http://en.wikipedia.org/wiki/File:Yee-cube.svg.
89. http://docs.lumerical.com/en/fdtd/ref_sim_obj_boundary_conditions_tab.html.

90. Palik, E. D., *Handbook of Optical Constants of Solids*. Academic Press: 1985; p 804.
91. P.B. Johnson, R. W. C., Optical Constant of the Noble Metals. *Physical Review B* **1972,** *6* (12), 4370-4379.
92. Wijaya, E.; Lenaerts, C.; Maricot, S.; Hastanin, J.; Habraken, S.; Vilcot, J.-P.; Boukherroub, R.; Szunerits, S., Surface plasmon resonance-based biosensors: From the development of different SPR structures to novel surface functionalization strategies. *Current Opinion in Solid State and Materials Science* **2011,** *15* (5), 208-224.
93. Ma, H.; Hyun, J.; Stiller, P.; Chilkoti, A., "Non-Fouling" Oligo(ethylene glycol)-Functionalized Polymer Brushes Synthesized by Surface-Initiated Atom Transfer Radical Polymerization. *Advanced Materials* **2004,** *16* (4), 338-341.
94. http://en.wikipedia.org/wiki/Streptavidin.
95. Anderson, M. P. a. N. L., A List of Candidate Cancer Biomarkers for Targeted Proteomics. *Biomark Insights* **2006,** *1*, 1–48.
96. Iijima, M.; Kadoya, H.; Hatahira, S.; Hiramatsu, S.; Jung, G.; Martin, A.; Quinn, J.; Jung, J.; Jeong, S.-Y.; Choi, E. K.; Arakawa, T.; Hinako, F.; Kusunoki, M.; Yoshimoto, N.; Niimi, T.; Tanizawa, K.; Kuroda, S. i., Nanocapsules incorporating IgG Fc-binding domain derived from Staphylococcus aureus protein A for displaying IgGs on immunosensor chips. *Biomaterials* **2011,** *32* (6), 1455-1464.
97. Gordon, R.; Brolo, A., Increased cut-off wavelength for a subwavelength hole in a real metal. *Opt. Express* **2005,** *13* (6), 1933-1938.
98. Zhou, R.; Chen, X.; Wang, S.; Lu, W.; Zeng, Y.; Chen, H.; Li, H.; Xia, H.; Wang, L., The surface plasmon resonance of metal-film nanohole arrays. *Solid State Communications* **2008,** *145* (1–2), 23-28.
99. Ziblat, R.; Lirtsman, V.; Davidov, D.; Aroeti, B., Infrared Surface Plasmon Resonance: A Novel Tool for Real Time Sensing of Variations in Living Cells. *Biophysical journal* **2006,** *90* (7), 2592-2599.
100. Lee, C. S.; Lee, S. H.; Kim, Y. G.; Lee, J. H.; Kim, Y. K.; Kim, B. G., A method of binding kinetics of a ligand to micropatterned proteins on a microfluidic chip. *Biosensors & bioelectronics* **2007,** *22* (6), 891-8.
101. Choi, H. J.; Kim, N. H.; Chung, B. H.; Seong, G. H., Micropatterning of biomolecules on glass surfaces modified with various functional groups using photoactivatable biotin. *Analytical biochemistry* **2005,** *347* (1), 60-6.
102. Menezes, J. W.; Barea, L. A. M.; Chillcce, E. F.; Frateschi, N.; Cescato, L., Comparison of Plasmonic Arrays of Holes Recorded by Interference Lithography and Focused Ion Beam. *Photonics Journal, IEEE* **2012,** *4* (2), 544-551.
103. http://www.photometrics.com/products/ccdcams/coolsnap_hq2.php.
104. Dobbins, H. M.; Peck, E. R., Change of refractive index of water as a function of temperature. *J. Opt. Soc. Am.* **1973,** *63* (3), 318-320.
105. http://www.coherent.com/products/?659/Ultra-Low-Noise-Diode-Laser-Modules.